

**Nonlinear mechanisms of wave propagation in periodic
structures: harmonic generation, dispersion correction,
and their interplay**

**A THESIS
SUBMITTED TO THE FACULTY OF THE GRADUATE SCHOOL
OF THE UNIVERSITY OF MINNESOTA
BY**

Weijian Jiao

**IN PARTIAL FULFILLMENT OF THE REQUIREMENTS
FOR THE DEGREE OF
DOCTOR OF PHILOSOPHY**

Stefano Gonella, Advisor

December, 2020

© Weijian Jiao 2020
ALL RIGHTS RESERVED

Acknowledgements

It has been such a wonderful journey for me to pursue my doctoral degree at the University of Minnesota, whose diverse and inspiring atmosphere allows me to broaden my horizons in both academic and non-academic aspects.

Among those who have contributed to this journey, I first would like to express my deepest gratitude to my advisor, Prof. Stefano Gonella for the opportunity and guidance he has provided to me. I believe that the influence he has exerted on me would continue to play a significant role in my future career.

I would like to thank Professors Henryk Stolarski, Bojan Guzina, and Ellad Tadmor for being my committee members, and for their useful comments and discussions that lead to a better version of the dissertation.

I greatly acknowledge the financial support from the Department of Civil, Environmental, and Geo- Engineering, the College of Science and Engineering at UMN, and the National Science Foundation, which allows me to explore exciting research ideas and make steady progress towards the completion of my PhD.

The interactions with my friends, the members of the Department of Civil, Environmental, and Geo- Engineering, and the staff of the University at large also contribute a considerable part of this journey, which I will cherish for the rest of my life.

I am eternally grateful to my mother Baoqun Jiao and my wife Lijuan Yu for their unconditional love and support. If it were not for them, this journey would become less meaningful and memorable.

Abstract

Periodic structures have been extensively investigated due to their unique dynamical properties, which have enabled a broad range of practical applications, especially in the context of wave control. Considering nonlinearity in periodic structures not only leads to a more complete description, but also opens new doors for the design of functional and tunable metamaterials. In this thesis work, we are interested in the dynamical behavior of periodic structures in the weakly nonlinear regime. In the case of quadratic nonlinearity, a well-known effect on wave propagation is second harmonic generation (SHG), which gives rise to a secondary harmonic in addition to the fundamental harmonic that is nearly identical to the linear response. This effect provides an opportunity to nonlinearly activate a second harmonic that exhibits complementary modal characteristics to those of the fundamental harmonic, thereby enriching the modal characteristics involved in the total response. Then, this modal enrichment functionality is explored in 1D periodic structures featuring internal resonators via numerical and experimental analysis, in which we use SHG as a mechanism to achieve energy trapping and localization in the resonators. Moreover, we extend our focus to experimentally demonstrate all the key components induced by SHG in 2D lattices of repulsive magnets supported by pillars. As for cubic nonlinearity, the effect on wave propagation is an amplitude-dependent correction of the dispersion relation, which can manifest either as a frequency shift or as a wavenumber shift depending on how the excitation is prescribed. Compared to the vast study on frequency shift, the scenario of wavenumber shift has only been marginally explored. To fill this gap, we first present a multiple scales framework to analytically capture the wavenumber shift on the dispersion relation of monatomic chains, showing that wavenumber shift is associated with harmonic boundary excitation. We then extend the framework to periodic structures with internal resonators to achieve tunability of locally resonant bandgaps. Last, we investigate the effects of the interplay between quadratic and cubic nonlinearities in periodic waveguides. Through two conceptual applications, we demonstrate that these effects can be leveraged to unveil an array of wave control strategies for the design of tunable metamaterials with self-switching functionalities.

Contents

Acknowledgements	i
Abstract	ii
List of Figures	vi
1 Introduction	1
1.1 Linear periodic structures	2
1.2 Nonlinear periodic structures	7
1.2.1 Solitons and discrete breathers	8
1.2.2 Nonlinear harmonic generation	8
1.2.3 Amplitude-dependent dispersion corrections	11
1.3 Motivation and outline	13
1.3.1 Inter-modal energy tunneling in nonlinear waveguides	13
1.3.2 SHG in two-dimensional lattices	14
1.3.3 Wavenumber shifts in cubic nonlinear chains	15
1.3.4 Interplay of quadratic and cubic nonlinearities	16
2 Mechanics of inter-modal energy tunneling in nonlinear waveguides	18
2.1 Waves in nonlinear homogeneous waveguides	18
2.1.1 Derivation of the coupled governing equations	18
2.1.2 Analytical solution	21
2.1.3 Comparison with 3D elasticity models and discussion	26
2.1.4 Numerical simulations	28
2.2 Nonlinear periodic waveguides with internal resonators	33

2.3	Conclusion	38
3	Inter-modal and subwavelength energy trapping in nonlinear metamaterial waveguides	40
3.1	Preliminary analysis of linear response	40
3.2	Experimental evidence of inter-modal tunneling	44
3.3	Conclusions	51
4	Nonlinear harmonic generation in two-dimensional lattices	52
4.1	Introductory example: 2D magnetic particle oscillator	53
4.1.1	Analytical model	53
4.1.2	Time-domain simulations	55
4.2	Wave propagation in 2D Repulsive Lattices	57
4.2.1	Analytical model	57
4.2.2	Full-scale simulations	60
4.3	Experiments on magnetic prototypes	62
4.3.1	Experimental characterization of linear behavior	62
4.3.2	Experimental characterization of nonlinear behavior	66
4.4	Conclusions	70
5	Wavenumber-space band clipping in nonlinear periodic structures	72
5.1	Dispersion relation of nonlinear monatomic chains	72
5.1.1	Multiple scales analysis	73
5.1.2	Full-scale simulation	79
5.2	Bandgap tunability in nonlinear locally-resonant periodic structures . .	81
5.2.1	Multiple scales analysis	81
5.2.2	Full-scale simulation	86
5.3	Conclusions	87
6	Doubly-nonlinear waveguides with self-switching functionality selection capabilities	88
6.1	Multiple scales analysis	88
6.1.1	Governing equations and linear dispersion relation	88

6.1.2	Nonlinear correction of the dispersion relation	92
6.1.3	Second harmonic generation and its correction shift	93
6.2	Full-scale simulations	100
6.3	Application for self-switching capabilities	102
6.3.1	Application 1: Optical mode switch	102
6.3.2	Application 2: Adaptive PMC switch	105
6.4	Conclusion	109
7	Conclusion and future outlook	111
7.1	Conclusion	111
7.2	Future outlook	113
	Bibliography	114
	Appendix A. Derivation of the complete stiffness matrix	125
	Appendix B. Preliminary stability analysis of the magnetic particle oscillator	127
	Appendix C. Experimental characterization of the force-displacement relation between two repulsive magnets	128
	Appendix D. Derivation of the non-zero forcing term f_u^2 at $O(\epsilon_2)$	130

List of Figures

1.1	Examples of periodic media	2
1.2	Bragg bandgap and locally resonant bandgap	3
1.3	A resonant metawedge	4
1.4	Spatial directivity in square lattices	5
1.5	Examples of tunable metamaterials	6
1.6	Examples of acoustic rectifier	10
1.7	Amplitude-dependent dispersion corrections	13
2.1	Schematic of a rod-beam structure	19
2.2	Relative magnitude of different nonlinear strain components	28
2.3	Schematic of a homogeneous waveguide	29
2.4	Lateral displacement response for increasing strength of nonlinearity	30
2.5	Axial displacement response for intermediate strength of nonlinearity	31
2.6	Spectral representation of lateral and axial responses	32
2.7	Amplitude of forced second harmonic vs. strength of nonlinearity	33
2.8	Unit cell of a metamaterial waveguide and band diagram	34
2.9	Snapshots of wave evolution	35
2.10	Spectral response of a metamaterial waveguide	36
2.11	Ratio of energy trapped in resonators to total energy in waveguide	37
3.1	Waveguide specimen and experimental setup	41
3.2	Band diagram of a waveguide featuring internal resonators	43
3.3	Experimentally reconstructed linear dispersion relation	44
3.4	Experimentally acquired nonlinear temporal response	45
3.5	Experimentally acquired nonlinear spectral response	46
3.6	Schematic illustration of quadrant shift due to aliasing	47

3.7	Detailed local wavefields	49
4.1	Schematic of a magnetic particle oscillator.	53
4.2	FRF of the magnetic particle resonator for four configurations	56
4.3	Schematic of triangular lattice and first Brillouin Zone	57
4.4	Dispersion relation of a repulsive lattice	59
4.5	Finite lattice used in full-scale simulation	60
4.6	Spectral response obtained from numerical simulation	61
4.7	Lattice prototype, equivalent spring-mass model, and band diagram	63
4.8	Experimental characterization of linear dispersion relation	65
4.9	Experimental evidence of nonlinearly generated second harmonics	66
4.10	Snapshots of experimentally acquired wavefields	67
4.11	k -plane amplitude spectra and filtered wavefields	69
5.1	Conventional multiple scales analysis of a nonlinear monatomic chain	74
5.2	Dispersion relation of a monatomic chain with hardening cubic nonlinearity	76
5.3	Dispersion relation of a monatomic chain with softening cubic nonlinearity	78
5.4	Spectral response of a monatomic chain with hardening cubic nonlinearity	79
5.5	Spectral response of a monatomic chain with softening cubic nonlinearity	81
5.6	Temporal and spatial responses of a nonlinear monatomic chain	82
5.7	Schematic of two nonlinear mass-in-mass chains	83
5.8	Dispersion relations of two nonlinear mass-in-mass chains	85
5.9	Temporal and spatial response of two nonlinear mass-in-mass chains	86
6.1	Schematic of a doubly-nonlinear spring-mass chain	89
6.2	Linear dispersion relation of a double-nonlinear chain	91
6.3	Dispersion correction under harmonic boundary excitation	94
6.4	Theoretical predictions of dispersion shifts	98
6.5	Numerical estimation of dispersion shifts in fundamental harmonic	101
6.6	Numerical estimation of dispersion shifts in second harmonics	102
6.7	Schematic of a self-adaptive optical mode switch	103
6.8	Numerical illustration of self-adaptive optical mode switch	104
6.9	Schematic of tunable PMC	105
6.10	Schematic of self-adaptive PMC switches	106
6.11	Numerical illustration of a self-adaptive PMC switch	107

C.1	Experimental setup for a static characterization of magnets	129
C.2	Force-displacement curve fitted using experimental data	129

Chapter 1

Introduction

In this dissertation, the physical systems of interest are structures and materials featuring repetitive patterns. Such systems are widely present in nature at different scales, ranging from crystal lattices (microscopic) to honey bee cells (macroscopic). In addition, artificial periodic structures and metamaterials can be designed to exhibit unique properties that cannot be found in conventional materials, thereby extending the territory of structural engineering and materials science. The objective of the dissertation is twofold. While the linear characteristics of periodic structures have been extensively studied thanks to the well-established analytical and numerical tools, their nonlinear characteristics (especially from the perspective of their dynamical behavior) are more complex and are still relatively explored. Therefore, the first objective is to investigate the nonlinear dynamical behavior of periodic structures, with an emphasis on wave propagation phenomena, and understand their underlying mechanisms via theoretical investigations supported by proof-of-concept numerical simulations and/or experiments. The second, more applied, objective is to leverage this nonlinear behavior for the design of metamaterials with versatile functionalities and wave manipulation capabilities, such as tunability and adaptivity. In this introductory Chapter, we first provide a brief review of the literature on the dynamical (phononic) properties of linear periodic structures, which serves as a stepping stone for nonlinear analysis. Then, we document benchmark studies on nonlinear periodic structures and their applications in metamaterials engineering. Finally, we present the motivation of each specific research task and the outline of the dissertation.

1.1 Linear periodic structures

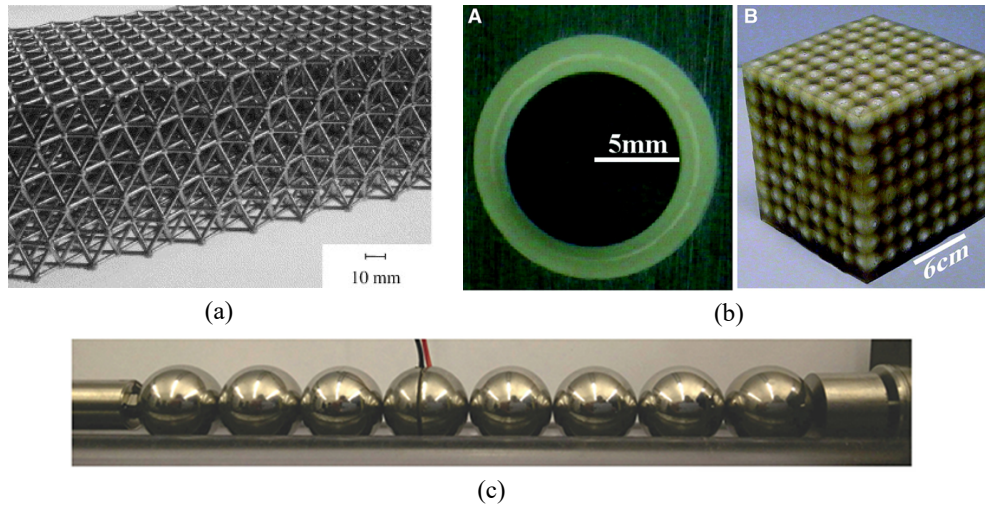


Figure 1.1: Examples of periodic media. (a) A octet-truss lattice material made from a casting aluminum alloy [1]. (b) A locally resonant metamaterial (A: unit cell consisting of a heavy core coated by soft material and a hard matrix material. B: the whole metamaterial) [2]. (c) A granular chain of stainless steel balls [3].

Phononic crystals, periodic structures, and acousto-elastic metamaterials at large are media featuring repetitive patterns consisting of fundamental elements (known as unit cells), which can be formed by periodic variation of the geometric or material properties or intrinsically induced by the discreteness of the structures. Examples include: lattice materials (Fig. 1.1(a)), periodic composites (Fig. 1.1(b)), and granular phononic crystals (Fig. 1.1(c)). The inherent periodicity gives rise to a number of unique dispersive properties. Perhaps, the most well-known dynamical property of periodic media is the ability to attenuate wave propagation within certain frequency intervals, referred to as phononic bandgaps [4, 5]. These bandgaps are due to Bragg scattering mechanisms induced by the periodic pattern of the structure when the unit cell size is commensurate to the wavelength, hence they are labeled “Bragg bandgaps”. By incorporating microstructures in the unit cells, it is possible to obtain locally resonant bandgaps with subwavelength characteristics and additional modal complexity [2, 6]. In this case, the systems are referred to as locally-resonant sonic crystals, or at times as acoustic metamaterials, although the term metamaterials has been used with more general significance

in other contexts. Two illustrative examples representative of the two types of systems introduced above, a diatomic chain and a so-called mass-in-mass chain, are shown in Fig. 1.2, along with their band diagrams (dispersion relations). The band diagrams elucidate the relation between frequency and wavenumber obeyed by harmonic waves that propagate through these media. We can appreciate that all the phonon bands (dispersion curves) are periodic in the wavenumber domain. Thus, the dispersive properties of the systems are fully described by limiting the investigation to the interval $[-\pi, \pi]$, referred to as the first *Brillouin Zone*. Moreover, by invoking the time reverse symmetry of the response in the *Brillouin zone*, the analysis can be further reduced to the *irreducible Brillouin Zone*, which is simply $[0, \pi]$ in the given examples. These concepts can be easily extended to 2D and 3D cases, in which symmetries in high-dimensional space need to be considered.

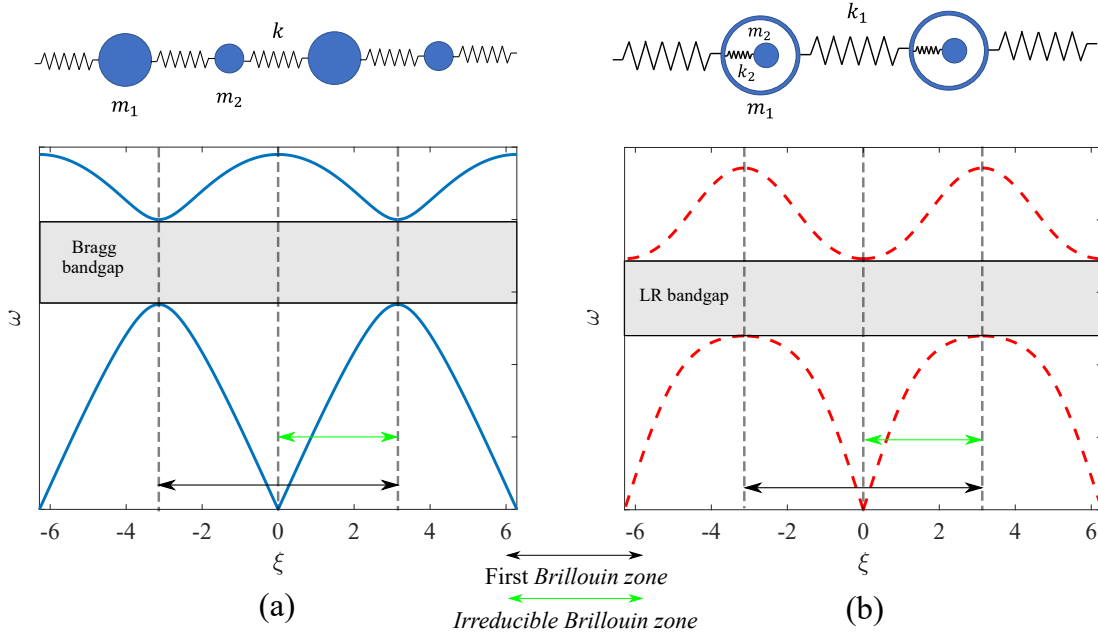


Figure 1.2: Bragg bandgap and locally resonant (LR) bandgap. (a) Diatomic chain and its band diagram featuring a Bragg bandgap. (b) Mass-in-mass chain and its band diagram featuring a LR bandgap.

One advantage of locally resonant bandgaps, compared to Bragg bandgaps, is their availability in lower-frequency ranges, which makes them appealing for practical applications of mechanical and structural engineering interest, such as sound and vibration

isolation [7, 8]. Following this paradigm, Celli and Gonella [9] used LEGO[®] bricks to realize locally resonant mechanisms in stubbed plates and use this platform as an avenue to obtain reconfigurable metamaterial prototypes through which they explored a variety of wave manipulation effects, including low-frequency wave guiding and seismic isolation. Another interesting application out of this concept is the resonant metawedge shown in Fig. 1.3, in which it is hypothesized that forests of trees can naturally interact with seismic waves and provide protection from earthquake events [10, 11]. Moreover, a medium with locally-resonant mechanisms can be engineered to display negative effective mass density [12], which has also been further exploited, in conjunction with other negative effective moduli, to achieve negative refraction [13] and elastic cloaking effect [14].

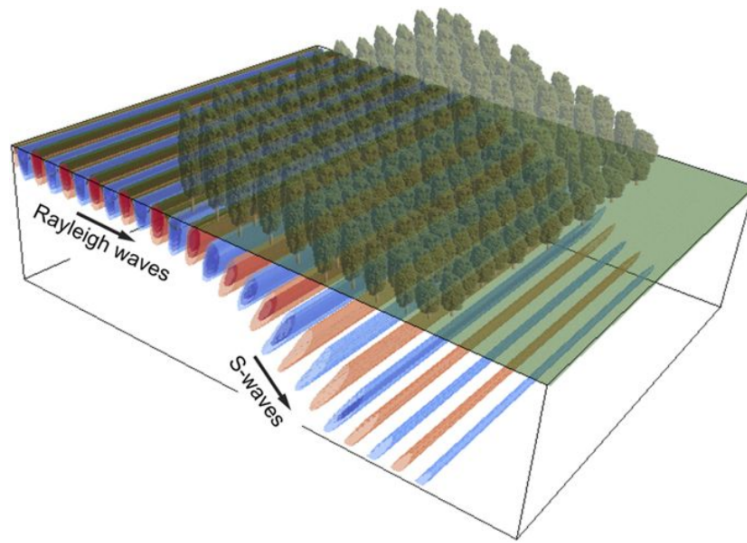


Figure 1.3: A resonant metawedge conceptually realized in a forest of trees with decreasing height [10].

An interesting feature germane to 2D (or possibly 3D) periodic structures is their frequency-dependent directivity, or directivity [16, 17, 18, 19, 20], which can be predicted by plotting the so-called group velocity contours (i.e., envelopes of the group velocity vectors plotted for variable angles of propagation in a polar plane) at different frequencies. For example, if we consider a square lattice plate excited out-of-plane by a point excitation, the preferential directions of propagation at low frequencies are along

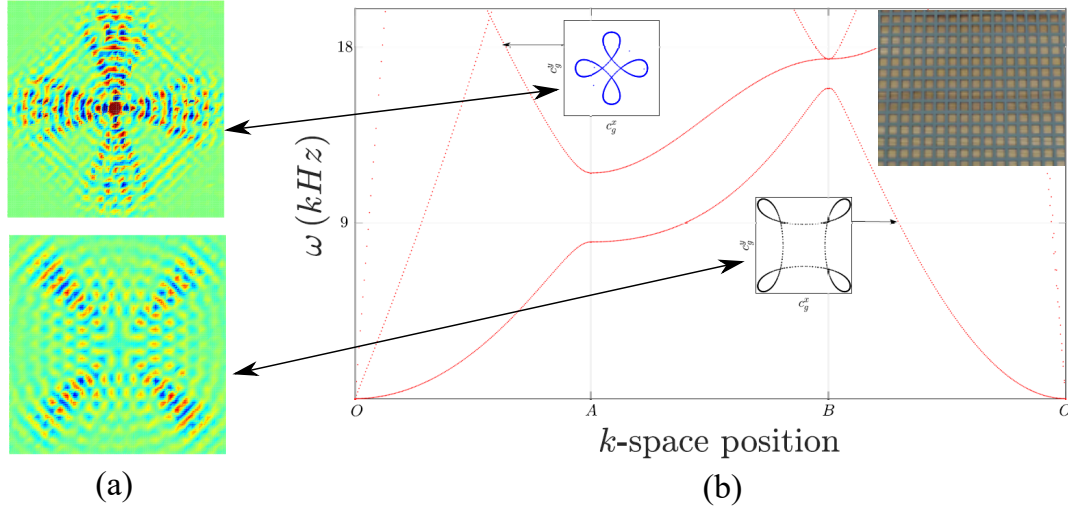


Figure 1.4: (a) Experimental out-of-plane wavefields in a square lattice at two selected frequencies, exhibiting complementary spatial directivity [15]. (b) The first two out-of-plane dispersion curves of the square lattice. The group velocity contours associated with the two frequencies (exhibiting complementary caustics patterns) are shown in the insets.

the diagonals of the lattice while, at high frequencies, the energy is routed preferentially along the horizontal and vertical directions, as shown in Fig. 1.4(a). We can see that the spatial patterns exhibited by the experimentally acquired wavefields are consistent with the group velocity contours depicted in the insets of Fig. 1.4(b).

Recently, an increasing amount of efforts have been devoted towards designing metamaterials with tuning capabilities. Achieving this goals often requires working with multi-physical systems. One strategy is to incorporate electro-mechanical phases in the systems. Along these lines, Casadei et al. [23] obtained an elastic waveguide with tunable dispersion properties by embedding piezoelectric resonators. The same piezoelectric framework involving electro-mechanical coupling has been employed to achieve rainbow trapping in 1D waveguides [24] and proposed to induce tunable directivity in 2D lattices [21]. In the latter case, the idea is to relax the symmetry of the unit cells by controlling the properties of piezoelectric patches connected to the auxiliary resonating microstructures of the cells, thereby affecting the globe directivity, as shown in Fig. 1.5(a). This type of coupling can also be employed to realize other wave control

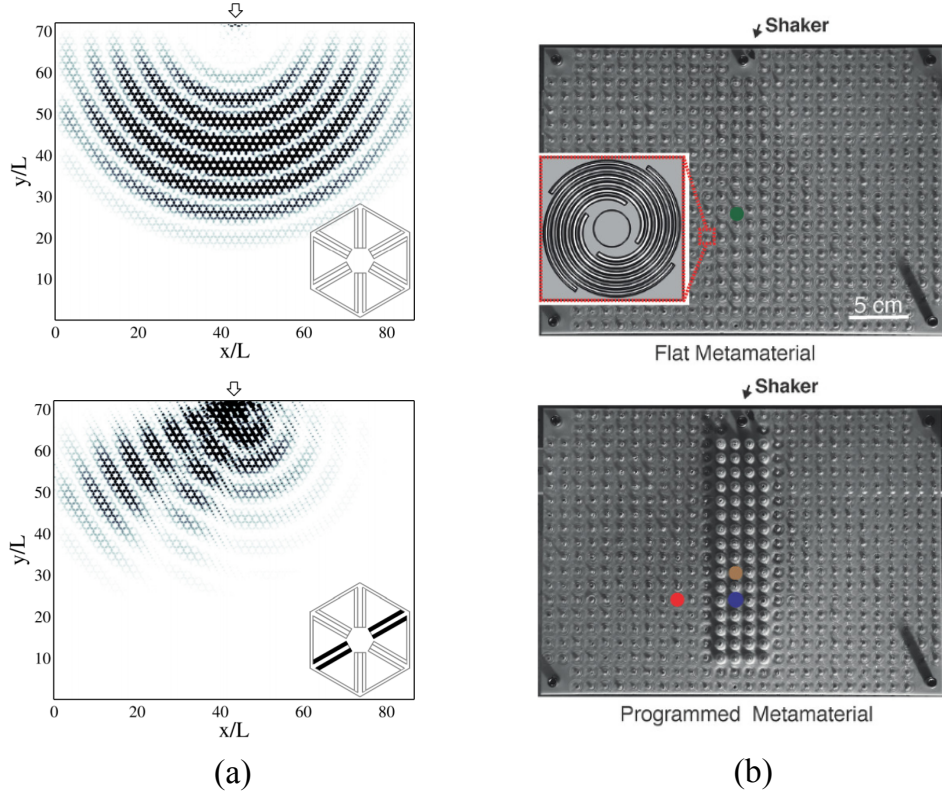


Figure 1.5: (a) Tunable directivity in a 2D metamaterial based on electro-mechanical effects. Top figure: all patches are open-circuited. Bottom figure: only selected patches (black ones) are shunted [21]. (b) Elastic wave control via magneto-mechanical effects. Top figure: 2D flat configuration (no external magnetic field). Bottom figure: 3D configuration when an external magnetic field is applied in a selected area [22].

capabilities [25], including active noise cancellation, cloaking, and wave steering. Another popular way to achieve tunability of the dynamical response is based on exploiting magneto-mechanical effects [26, 27, 22, 28]. One interesting realization of this concept, shown in Fig. 1.5(b), was obtained by adding magnets in the unit cells through spiral springs. When an external magnetic field is introduced, the original unit cell can be deformed into different shapes which would in turn affect the dynamical properties of the structure. On top of that, the nonlinearity of the different sources available in mechanical systems has been explored as an alternative avenue for the design of metamaterials with tuning capabilities, which will be discussed in the section below.

1.2 Nonlinear periodic structures

The different sources of nonlinearity available in mechanical systems have been explored as an alternative avenue for the design of metamaterials with tuning and wave manipulation capabilities. In certain systems, the magnitude of the available nonlinear effects is not only dictated by the geometric and material properties of the system but also controlled by externally controllable parameters. For instance, in granular crystals, the constitutive behavior (i.e., the nonlinear Hertz law) can be controlled by the external precompression, so it is possible to vary the level of precompression to tune the dynamical response [29]. Similar ideas have been exploited in the context of multistable materials and structures, where instability can be utilized to trigger reconfigurations in the lattice structure of compliant metamaterials, thus modifying their dispersion relations and controlling their phononic characteristics [30, 31, 32, 33, 34]. However, it is important to note that, in these examples, nonlinearity is involved in the externally applied *static* tuning mechanisms, while the dynamical response is still considered in the linear regime in the form of small-amplitude waves and vibrations. When it comes to the nonlinear regime, accounting for nonlinearity provides a more complete description of the dynamical behavior of periodic structures that extends to operational conditions characterized by finite (or even large) amplitudes of excitation. Moreover, the amplitude-dependent dynamical characteristics of these nonlinear systems have enabled a variety of unique functionalities, which have opened new doors for active wave and vibration control without the need for external stimuli.

The first study on nonlinear dynamics of periodic structures is reported in [35], which investigates vibrations in a one-dimensional discrete system of oscillators interacting through anharmonic potentials, referred to as the Fermi-Pasta-Ulam-Tsingou (FPUT) lattice system. Later, anharmonic chains and lattices become an important platform for nonlinear analysis because of their mathematical and numerical tractability. In the remainder of this section, we will demonstrate several interesting nonlinear phenomena with an emphasis on waves and vibrations and their implications in the context of periodic structures and metamaterials.

1.2.1 Solitons and discrete breathers

A soliton or solitary wave is a nonlinear wave that can preserve its shape and speed even in a dispersive medium and after interactions with other solitons. This phenomenon was first described in 1834 by Russell who observed a solitary wave in the Union Canal in Scotland. Later, the Korteweg-de Vries (KdV) equation was proposed as a mathematical model of waves on shallow water surfaces [36]. A milestone work by Zabusky and Kruskal [37] demonstrated that the KdV equation permits soliton solutions, and further showed that the KdV equation was the continuum limit of the FPUT system. Solitons have also been extensively studied in granular crystals composed of beads interacting via Hertzian contacts [38]. Moreover, the degree of nonlinearity in granular chains can be simply controlled by precompressions, thereby offering opportunities to achieve tunable properties of solitary wave [39]. Based on this tuning effect, a nonlinear acoustic lens, capable of focusing acoustic signals, is realized using ordered arrays of granular chains [40]. Other notable applications of solitary wave include energy trapping [41], topologically protected mechanical conductor [42], and pulse-driven robot [43]. Recently, it has been shown that the propagation of elastic solitons can also be supported in soft architected materials [44, 45] and composite laminates [46].

Another interesting nonlinear phenomenon in discrete systems is known as *intrinsic localized modes* (i.e., *discrete breathers*) in which energy concentrates in a localized and oscillatory fashion. Their existence has first been confirmed by theoretical investigations of anharmonic lattices [47, 48], demonstrating that it is a result of the interplay between nonlinearity and discreteness. In the past two decades, experimental studies have been conducted on various physical systems [49, 50]. Among them, granular crystals provide an ideal platform for the experimental observation of discrete breathers at the macroscopic scale [51, 52].

1.2.2 Nonlinear harmonic generation

In weakly nonlinear systems, a well-known wave phenomenon associated with quadratic nonlinearity is second harmonic generation (SHG), also called frequency doubling. In the context of elastic waves, this phenomenon was first studied in classical continua and structures (an excellent review can be found in [53]) and only recently has been extended

to unconventional solids such as composite materials and metamaterials. In general, there are two different scenarios of SHG, to classify which we introduce two terminologies. The first scenario, termed *intra-modal* SHG, is observed when the fundamental harmonic and the second harmonic have identical (or comparable) modal characteristics. For example, a longitudinal second harmonic can be generated by a fundamental longitudinal wave propagating in a nonlinear rod [54].¹ The other scenario is *inter-modal* SHG (or *hopping*), where the fundamental harmonic and the second harmonic have orthogonal (or complementary) modal characteristics. Here “hopping” pictorially captures the fact that, if we monitor the phenomenon of nonlinear second harmonic generation on a band diagram, the wave solution jumps from the $\omega - k$ point of the fundamental wave to another spectral point on a different branch. An example of this is a transversal second harmonic generated by a fundamental longitudinal wave in a 3D infinite solid [55, 56]. While all the wave modes in the above examples are non-dispersive, inter-modal hopping can also be found in dispersive structures. De Lima and Hamilton [57] studied the propagation of finite-amplitude waves in isotropic elastic plates, showing that a primary shear horizontally-polarized (SH) mode can excite a resonant Rayleigh-Lamb mode at the second harmonic. For specific structural configurations and excitation conditions, phase matching condition (PMC) can be established when the fundamental harmonic and the second harmonic have the same phase velocity, resulting in cumulative second harmonic propagation and overall stronger nonlinear signatures, as experimentally confirmed and reported in [58, 59, 60, 61].

In the context of periodic structures and metamaterials, periodicity gives rise to additional modal and dispersive complexity, compared to conventional materials, which affects the way in which the nonlinear response manifests and offers new possibilities for both intra- and inter-modal hopping. For example, Sánchez-Morcillo et al. [65] used perturbation techniques to find an explicit solution for the nonlinearly-generated second harmonics in monatomic granular chains, which can be classified as a case of intra-modal hopping, and investigated the interplay of SHG and dispersion. Later, Mehrem et al. [66] conducted a series of experiments to confirm the existence of SHG in a nonlinear chain consisting of repulsive magnets. A few works have also explored

¹ This is one of the few examples where an exact solution is available, while in most cases there only exist approximate solutions.

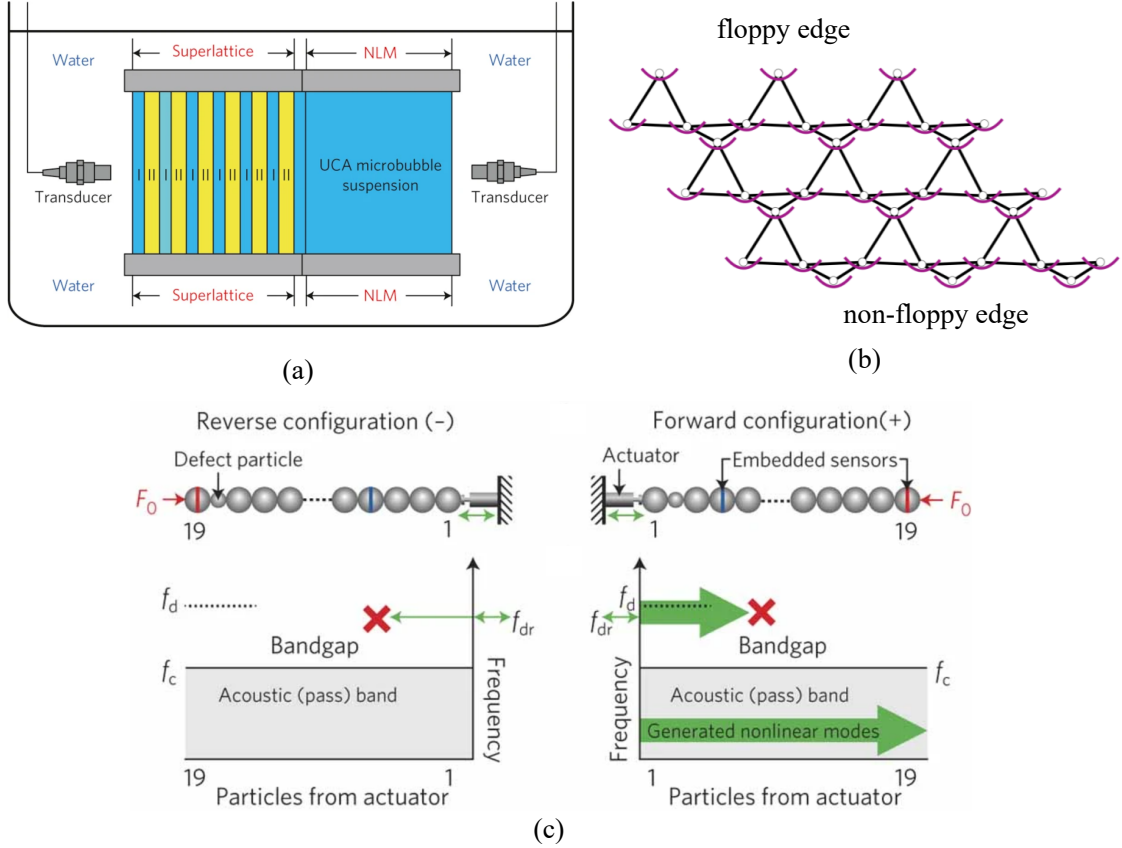


Figure 1.6: Examples of acoustic rectifier. (a) A superlattice coupled with a nonlinear medium (NLM) [62]. (b) A nonlinear lattice featuring a topological floppy edge [63]. (c) A 1D granular crystal featuring a mass defect [64].

SHG in high-dimensional and multi-degree of freedom periodic structures, including diatomic chains [67, 68], 2D phononic crystals [69, 70], and lattice materials [71, 72], in which the availability of both intra- and inter-modal hopping results in nonlinear enrichment of the dynamical response (i.e., modal mixing) and additional opportunities for the establishment of PMC that effectively boosts the energy tunneling between the fundamental wave and the second harmonic [67, 70, 73]. An interesting application of SHG is the realization of acoustic rectifiers (or diodes). One design of such acoustic rectifiers is proposed by Liang et al. [62], who coupled a superlattice with a nonlinear medium as depicted in Fig. 1.6(a). In the structure, wave propagation is prohibited if the excitation is prescribed at the end of the superlattice with a frequency falling inside

the bandgap. However, if the same excitation is prescribed at the other end (i.e., the open end of the nonlinear medium), the nonlinear harmonic induced via SHG is allowed to propagate and reach the opposite end of the device. The asymmetric wave behavior of the structure enables a rectified energy flux of acoustic waves, hence the name acoustic rectifier. Another design involves the use of nonlinear topological Maxwell lattices that exhibit topologically protected floppy edge modes [63]. If the excitation is imposed at the floppy edge, SHG is promoted due to the large boundary deformations established by the activated floppy mode. In contrast, SHG is much weaker if the excitation is imposed at the non-floppy edge featuring high rigidity. Therefore, acoustic rectification effect and nonreciprocal behavior can be established.

In addition to SHG, quadratic nonlinearity can also be exploited to enable the generation of other super- and sub-harmonics [74, 75]. Considering two waves with difference frequencies f_1 and f_2 propagating in a medium featuring quadratic nonlinearity, the self-interaction of the two waves results in the distribution of energy to frequencies that are linear combinations of the two frequencies (i.e., $mf_1 \pm nf_2$ in which m and n are integers). This effect has also been exploited to realize acoustic rectifiers in granular crystals. One example is offered by Boechler et al. [64], who consider a 1D granular crystal consisting of steel spheres and a mass defect (Fig. 1.6(c)). In the reverse configuration (the actuator is placed far away the defect), an incident wave cannot propagate through the crystal for a driving frequency inside the bandgap. However, in the forward configuration where the actuator is placed near the defect, the defect causes the generation of nonlinear modes that are allowed to propagate to the other end. Recently, Zega et al. [76] have experimentally demonstrated the emergence of subharmonic attenuation zones in a locally resonant metamaterial, which is induced by autoparametric resonance that gives rise to the generation of sub-harmonics.

1.2.3 Amplitude-dependent dispersion corrections

In the case of cubic nonlinearity, several studies have addressed the effects on the dynamical properties of oscillators, e.g., the emergence of chaotic behavior [54, 77]. In the context of wave propagation, the main signature of cubic nonlinearity is the amplitude-dependent correction of the dispersion relation, which can manifest either as a frequency shift or as a wavenumber shift depending on whether the problem is treated

as an initial value problem or a boundary value problem. Various analytical models have been proposed to capture the dispersion correction in monatomic chains, whose low modal and dispersive complexity make them amenable to tractable mathematical models. Chakraborty and Mallik [78] presented a perturbation scheme to determine the amplitude-dependent properties of the frequency cutoffs of nonlinear monatomic chains. Narisetti et al. [79] derived an explicit expression to predict frequency shifts using the *Lindstedt-Poincaré* perturbation technique, which allows for a derivation of an explicit mathematical expression of the dispersion relation correction. A more general analytical treatment based on multiple scales analysis yields consistent results for the frequency shifts if harmonic excitations are prescribed in space (i.e., initial value problem), which is documented in textbooks on perturbation methods [80]. While most theoretical models rely on perturbation methods, Lazarov and Jensen [81] employed the method of harmonic balance to study the shift of bandgaps in chains with attached nonlinear resonators. These shifting effects have also been explored in two-dimensional and multi-degree of freedom periodic structures [82, 83, 84, 85], in which the spatial characteristics of wave propagation become amplitude-dependent. Moreover, experimental evidence of dispersion shifts achievable in granular systems has been reported in [68, 86].

The amplitude-dependent dispersion correction has opened new doors for the design of tunable periodic structures and metamaterials. Fig. 1.7 depicts the dispersion curve of a monatomic spring-mass chain with hardening (or softening) cubic nonlinearity (using the formula given in [79]), in which we observe that the dispersion curve shifts upwards (or downwards) with increasing amplitude. As a consequence, the nonlinear structure is endowed with tunable functionalities which are especially pronounced for excitations near the cutoff frequency, whereby it is possible to determine whether an excited wave can propagate or not via a simple control of the excitation amplitude.

In addition to the dispersion shifts, other interesting effects of cubic nonlinearity (not strictly limited to the weakly nonlinear regime) include chaotic bands [87] and third harmonic generation (THG) [88]. Recently, strong cubic nonlinearity experimentally realized connecting masses with thin steel wires has been employed to break acoustic reciprocity in a lattice composed of coupled oscillators with internal scale hierarchy, thereby achieving asymmetric energy transfer [89].

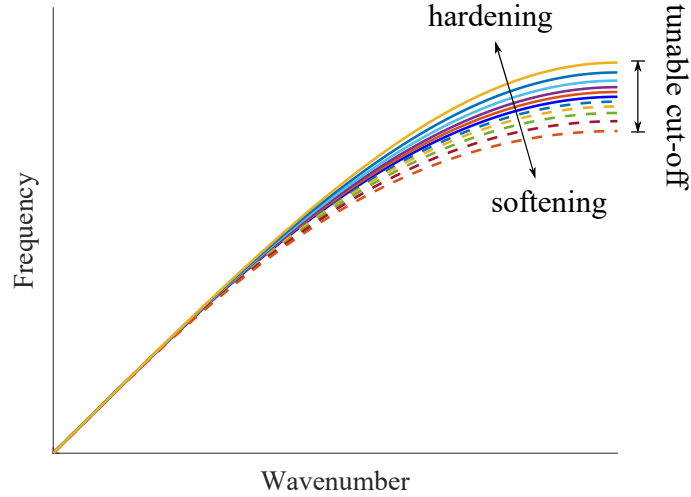


Figure 1.7: Dispersion curve of monatomic spring-mass chain with hardening or softening cubic nonlinearity, showing tunable characteristics of the cutoff frequency.

1.3 Motivation and outline

Among the above-discussed nonlinear phenomena, we are especially interested in SHG, dispersion corrections, and their potential interactions. The general motivation of the dissertation is to characterize these nonlinear effects in the context of periodic structures and metamaterials, and explore their implications for wave manipulation and tunability. A description for each specific research task is given below.

1.3.1 Inter-modal energy tunneling in nonlinear waveguides

By definition, inter-modal hopping mechanisms are more conducive to modal complementarity. If maximizing the degree of complementarity is the primary design objective, it seems reasonable to work with structural systems that, in virtue of their intrinsic geometric characteristics, naturally feature highly complementary wave modes. To this end, we propose a new class of inter-modal hopping mechanism via SHG that involves the coupling between axial and lateral degrees of freedom in nonlinear beam-like waveguides. First, we derive an explicit expression for the full nonlinear response that is valid

in the weakly nonlinear regime. Then, the analytical solution is verified via finite element simulations, revealing that a non-oscillatory component and two second-harmonic contributions coexist in the response. A special case, when phase matching conditions are established, is presented to illustrate an effective way of magnifying this nonlinear response. We then extend the analysis to periodic waveguides with internal resonators, in which the simultaneous availability of locally-resonant bandgaps and nonlinear mode hopping mechanisms result in the possibility to activate the resonators even at relatively low frequencies. In this context, inter-modal tunneling provides an unprecedented mechanism to transfer conspicuous packets of energy to the resonating microstructure.

We then proceed to experimentally demonstrate the phenomenon of nonlinearity-activated inter-modal energy tunneling in a elastic metamaterial waveguide with internal resonators and we show how this effect can be exploited to achieve conspicuous energy localization and trapping. 3D laser vibrometry at different scales of spatial refinement is employed to capture global and local in-plane features of the wavfield. The measured response naturally yields an experimental reconstruction of the band diagram of the waveguide and reveals unequivocally the spectral signature of the high-frequency modes that are activated by tunneling. Finally, a detailed scan of selected unit cells highlights a strong and persistent axial activation of the resonators which displays subwavelength deformation.

1.3.2 SHG in two-dimensional lattices

While SHG has been widely studied in one-dimensional nonlinear metamaterials and waveguides, the investigation of its effects on the spatial characteristics of nonlinear wavefields in 2D metamaterials has been more sporadic [71, 72] and still lacks a definitive experimental observation of nonlinear response at amplitude levels that are suitable for practical applications. Recently, it has been shown that lattices can be formed at the macroscopic scale using arrays of repulsive magnets [90, 66, 91, 92]. In light of it, a lattice prototype is experimentally realized involving finite-size magnets supported by thin pillars, which can be interpreted as a practical realization of a triangular lattice of repulsively-interacting particles with on-site potentials. A unique feature of the system is that in the initial equilibrium configuration each magnet is subjected to a set of self-balancing static forces exchanged with its neighbors. Before jumping into the nonlinear

regime, we first theoretically predict the linear dispersion relation, revealing the important role played by the initial static forces on the dispersive behavior of the system. We then experimentally confirm the predictions by reconstructing the dispersion relation using data obtained via 3D laser vibrometry.

Using the linear characterization as guidelines, we perform a suite of experiments to investigate the nonlinear behavior of the specimen. Specifically, we first verify the existence of SHG in the spectrum of the response. To this end, we take advantage of the strength of the nonlinear effects granted by the particle nature of the system, compared to the case of structural lattices, even without the establishment of phase matching conditions. Moreover, we experimentally confirm that the second harmonic encompasses two different contributions. Finally, we show that the second harmonic features distinctive and complementary modal and spatial characteristics when we compare the response with that of the fundamental harmonic.

1.3.3 Wavenumber shifts in cubic nonlinear chains

The dispersion correction induced by cubic nonlinearity can manifest either as a frequency shift or as a wavenumber shift. The different manifestations reflect the flexibility of the choice of the control variable, which is linked to the type of excitation. For example, if the excitation is prescribed as an initial condition (spatial profile), one can consider the wavenumber as a fixed externally-controlled parameter, which enforces the cubic nonlinear effect to manifest as a frequency shift. In contrast, working with a boundary excitation assumes that the input frequency can be treated the fixed parameter, and therefore the effect has to manifest as a wavenumber shift.

While the bulk of the literature on this effect is focused on characterizing frequency shifts, because of the availability of well-established mathematical tools for this task, this framework is not compatible with realistic scenarios (e.g., experiments) in which the excitation is prescribed as a harmonic oscillation at the boundaries. This condition is commonly encountered in practical applications of engineering interests in which the excitation is exerted using a point source actuation system (such as a shaker or a piezoelectric transducer). To address this limitation, we first develop a multiple scales scheme to properly capture the dispersion correction of weakly nonlinear chains under boundary excitations (i.e., wavenumber shifts). Then, we demonstrate via numerical

simulations that cubic nonlinearity in combination with harmonic boundary excitations, gives rise to unusual dispersive regimes that are fundamentally different from those associated with the frequency shifts. Finally, the framework is extended to locally-resonant periodic structures, in which the additional degree of freedom induced by the internal resonator provides new opportunities to achieve bandgap tunability under practical excitation constraints.

1.3.4 Interplay of quadratic and cubic nonlinearities

In most relevant contexts, the effects of quadratic and cubic nonlinearities have been studied separately. A few works have dealt with these two types of nonlinearity jointly to study wave propagation in classical anharmonic lattices [93, 94, 95] and in granular systems obeying Hertz contact law [68, 96], and to explore amplitude gaps for solitary waves in elastic metamaterials [97, 98]. However, little attention has been paid to the implications of the quadratic-cubic (Q-C) interplay for wave control and tunability. The objective of this task is precisely to fill this gap. To this end, we consider a medium - here a spring-mass chain on nonlinear elastic foundation - that features simultaneously both sources of nonlinearity (at different orders) embedded in the chain and in the support elastic elements. The coexistence of Q-C effects opens unprecedented opportunities for amplitude-controlled wave tuning. We are interested in how the cubic nonlinearity can be used to effectively modify the way in which the quadratic nonlinear effects manifest in the response. Specifically, we investigate whether the dispersion correction caused by cubic nonlinearity can be used as an internal switch (or mode selector) capable of switching on/off certain high-frequency features of the response that are generated by the quadratic mechanisms, or at least controlling their strength. This additional tuning capability is fully intrinsic to the system, as the selection of the functionality is solely due to the nonlinear effects, and therefore controlled by the amplitude of excitation, without resorting to any active external tuning.

To provide guidelines, a multiple scales analysis is applied to obtain the full nonlinear response of the chain. Due to the Q-C interaction, SHG is observed with some unique modal characteristics, including magnified dispersion shift and tunable PMC. Two examples of tunable systems with self-adaptive switches are given to illustrate the wealth of wave manipulation capabilities that directly leverage the Q-C nonlinear interaction.

The outline of the rest of the dissertation is listed as follows

- Chapter 2 presents theoretical and numerical study on mechanisms of inter-modal energy tunneling in nonlinear waveguides, which is adapted from “**W. Jiao and S. Gonella. Mechanics of inter-modal tunneling in nonlinear waveguides. J. Mech. Phys. Solids, 111:117, 2018.**” [99]
- Chapter 3 provides experimental evidence of inter-modal energy tunneling in a locally resonant metamaterial, which is adapted from “**W. Jiao and S. Gonella. Intermodal and subwavelength energy trapping in nonlinear metamaterial waveguides. Phys. Rev. Appl., 10:024006, Aug 2018.**” [100]
- In Chapter 4, the propagation of two-dimensional nonlinear waves is experimentally investigated in a lattice consisting of repulsive magnets supported by thin pillars, part of which is adapted from “**W. Jiao and S. Gonella. Dynamics of interacting particle systems: Modeling implications of the repulsive interactions and experiments on magnetic prototypes. Phys. Rev. B, 102:054304, Aug 2020.**” [101].
- In Chapter 5, a theoretical framework based multiple scales analysis is developed to properly capture wavenumber shifts in nonlinear periodic structures under harmonic boundary excitations, which is validated via full-scale simulations.
- Chapter 6 demonstrates the interplay of quadratic and cubic nonlinearities and its implications for self-switching functionalities in weakly nonlinear spring-mass chains, which is adapted from “**W. Jiao and S. Gonella. Doubly nonlinear waveguides with self-switching functionality selection capabilities. Phys. Rev. E, 99:042206, Apr 2019.**” [102]
- Chapter 7 gives a final conclusion and discussion of the analyses presented in the dissertation.

Chapter 2

Mechanics of inter-modal energy tunneling in nonlinear waveguides

In this Chapter, we explore the availability of inter-modal hopping through geometric coupling between flexural and axial degrees of freedom in 1D waveguides . To this end, an analytical model is proposed to capture flexural-to-axial inter-modal hopping in homogeneous waveguides using basic arguments of perturbation analysis, which is validated via a suite of nonlinear finite element simulations. We then use the model as a guideline to investigate the counterpart of this phenomenon in periodic waveguides featuring internal resonators. Moreover, we employ this hopping mechanism to transfer conspicuous packets of energy to the resonators, thereby achieving energy trapping and harvesting functionalities.

2.1 Waves in nonlinear homogeneous waveguides

2.1.1 Derivation of the coupled governing equations

In this section, we provide a theoretical description of the coupled axial-flexural dynamics of homogeneous slender waveguides through the lens of a simple structural mechanics description that combines a nonlinear rod model and a linear Euler-Bernoulli beam model. In this framework, the critical coupling mechanism is captured by the relation

between lateral and axial degrees of freedom that is intrinsically involved in the kinematics of bending. In the later sections, the conclusions drawn using these models will be compared against finite-element simulations to provide qualitative interpretations of the computational results. Finite element (FE) simulations will be conducted by modeling waveguides as two-dimensional elastic solids, motivated by the fact that this allows us to more seamlessly frame the problem within the general framework of nonlinear computational elasticity. The reason for resorting to structural mechanics models in this theoretical section is twofold. On one hand, this choice allows for tractable one-dimensional models, for which it is possible to derive, under special conditions, simple yet illustrative analytical solutions; while these simplified solutions do not correspond exactly to the dynamic conditions modeled in the simulated environment, they can explain a large range of behaviors observed in simulations with satisfactory accuracy. Secondly, a description through a rod-beam model, in which axial and flexural mechanisms are treated separately, seems naturally well-suited to describe the dichotomic inter-modal nature of the hopping mechanisms that we intend to investigate.

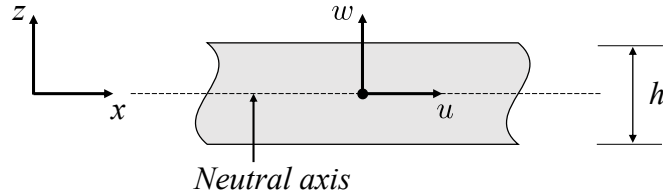


Figure 2.1: Schematic of a rod-beam structure. Every point along the neutral axis has two degrees of freedom (axial and lateral displacements) denoted as u and w , respectively.

The construction of our model begins with the selection of an appropriate strain descriptor. To capture the effects of nonlinearity, we invoke the Green-Lagrange strain tensor

$$\boldsymbol{\varepsilon} = \frac{1}{2}[\nabla\mathbf{u} + (\nabla\mathbf{u})^T] + \frac{1}{2}(\nabla\mathbf{u})^T\nabla\mathbf{u} \quad (2.1)$$

where \mathbf{u} is a vector of displacements (i.e., $\mathbf{u} = [u \ w]^T$). Nevertheless, we still assume that the strain is relatively small, which essentially corresponds to enforcing the assumptions of weak nonlinearity. We consider a two-dimensional body in the $x - z$ plane as shown in Fig. 2.1, whose kinematics are described by the two displacement degrees of freedom

u and w . In addition, we assume that the body is sufficiently slender along the x direction to be modeled as a rod-beam structure (with thickness h), which is capable of experiencing both axial and flexural deformations.

At this point we introduce the critical assumption that the effects of geometric nonlinearity are predominantly observed in the axial response even if the excitation is prescribed to optimally trigger flexural deformation. This implies that, while we must adopt a fully nonlinear description for the axial deformation, a linear bending model is sufficient to describe the flexural deformation. This assumption, which is indispensable to achieve a tractable model, is supported by the results (reported in a later section) of our simulations of slender beams excited in bending, in which the medium is treated as a two-dimensional elastic body and therefore no discrimination between axial and flexural motion is made *a priori*: in these simulations the signature of geometric nonlinearity (amplitude dependence of the response) is indeed predominantly observed in the axial response. Under this assumption, the only relevant component of the strain ε_{xx} can be written as:

$$\varepsilon_{xx} = \frac{\partial u}{\partial x} + \frac{1}{2} \left(\frac{\partial u}{\partial x} \right)^2 + \frac{1}{2} \left(\frac{\partial w}{\partial x} \right)^2 \quad (2.2)$$

In order to separately account for the contributions to the strain from the axial and lateral degrees of freedom, the axial displacement is decomposed as $u = u_A + u_F$. u_A denotes the axial displacement of all points belonging to the cross section of coordinate x due to axial elongation. From Euler-Bernoulli beam theory, we assume that the lateral displacement of the beam can be described by the lateral displacement of its neutral axis $w = w(x)$ and u_F , which represents the profile of axial displacement established across the thickness due to bending, can be written as:

$$u_F = -z \frac{\partial w}{\partial x} \quad (2.3)$$

Substituting Eq.2.3 into Eq.2.2 yields

$$\begin{aligned} \varepsilon_{xx} &= \frac{\partial u_A + u_F}{\partial x} + \frac{1}{2} \left(\frac{\partial u_A + u_F}{\partial x} \right)^2 + \frac{1}{2} \left(\frac{\partial w}{\partial x} \right)^2 \\ &= \frac{\partial u_A}{\partial x} - z \frac{\partial^2 w}{\partial x^2} + \frac{1}{2} \left(\frac{\partial u_A}{\partial x} - z \frac{\partial^2 w}{\partial x^2} \right)^2 + \frac{1}{2} \left(\frac{\partial w}{\partial x} \right)^2 \\ &= \frac{\partial u_A}{\partial x} - z \frac{\partial^2 w}{\partial x^2} + \frac{1}{2} \left(\frac{\partial u_A}{\partial x} \right)^2 + z \frac{\partial u_A}{\partial x} \frac{\partial^2 w}{\partial x^2} + \frac{1}{2} \left(z \frac{\partial^2 w}{\partial x^2} \right)^2 + \frac{1}{2} \left(\frac{\partial w}{\partial x} \right)^2 \end{aligned} \quad (2.4)$$

Assuming that the material is linear elastic, the stress along the x direction is given as:

$$\sigma_{xx} = E \varepsilon_{xx} \quad (2.5)$$

where E is the Young's modulus. Integrating σ_{xx} (with Eq.2.4 plugged in) over the cross-section and equilibrating internal, external and inertial forces acting along x , we obtain the following governing equation for axial motion:

$$\rho A \frac{\partial^2 u}{\partial t^2} = EA \frac{\partial}{\partial x} \left[\frac{\partial u}{\partial x} + \frac{1}{2} \left(\frac{\partial u}{\partial x} \right)^2 + \frac{1}{2} \left(\frac{\partial w}{\partial x} \right)^2 + \frac{1}{24} h^2 \left(\frac{\partial^2 w}{\partial x^2} \right)^2 \right] + p(x, t) \quad (2.6)$$

where $u = u(x, t)$, A is the area of the cross section, and $p(x, t)$ is an external axial force per unit length. Note that the antisymmetric second and fourth terms in Eq.2.4 have vanished after integrating over the cross-section and we have relabeled u_A as u for convenience.

As discussed above, the flexural part of the problem is described by a linear model. Consequently, the equation for the transverse motion reduces to the canonical 4th-order partial differential equation of Euler-Bernoulli theory:

$$\rho A \frac{\partial^2 w}{\partial t^2} + EI \frac{\partial^4 w}{\partial x^4} = q(x, t) \quad (2.7)$$

where $w = w(x, t)$, I is the second moment of area of the beam's cross-section and $q(x, t)$ is an external lateral force per unit length.

2.1.2 Analytical solution

We now set forth to find an analytical solution for the coupled equations 2.6 and 2.7 under special excitation conditions. Since Eq. 2.7 is linear and only involves d.o.f. w , we begin by seeking a harmonic solution of the form:

$$w = \mathcal{A} \sin(k_F x - \omega t) \quad (2.8)$$

where \mathcal{A} is the amplitude of the wave, ω is the frequency and $k_F = 2\pi/\lambda_F$ is the wavenumber for the flexural wave propagation mode. It is worth noting that the validity of Euler-Bernoulli beam model imposes a constrain on the wavelength λ_F for a given thickness h , which is linked to the fundamental assumption that the behavior of the

beam can be exhaustively described by the deformation of its neutral axis. In general, a decent prediction can be obtained from Euler-Bernoulli beam model if $\lambda_F/h \geq 10$ is satisfied.

At this point, it is useful to introduce the nondimensional quantity $\mathcal{A}k_F$, which basically represents an amplitude of the wave relative to its wavenumber and *de facto* introduces the wavelength of the excitation as an important length scale of the problem. It seems reasonable to take this quantity as a well-suited metric to quantify the effects of nonlinearity, which are controlled by the (nondimensional) strain established in the medium. Essentially $\mathcal{A}k_F$ suggests that stronger nonlinear effects are achieved by either increasing \mathcal{A} for a fixed wavenumber, or by reducing the wavelength for a given prescribed amplitude - both cases resulting in an increase in strain. In light of these considerations, we can impose weak nonlinearity by setting $\mathcal{A}k_F = \epsilon$; as we will discuss later, this will be useful to establish a common smallness reference to estimate the relative order of the terms in the nonlinear response. Before proceeding further, we point out that Eq. 2.8 implies a *sustained*, perfectly mono-chromatic harmonic excitation. This condition is adopted here for convenience, as it is amenable to analytical treatment. In contrast, our numerical simulations will involve narrow-band tone bursts, which represent more realistic excitations of engineering interest. Despite the intrinsic differences between the two scenarios, we will show that this theoretical model has the ability to explain qualitatively the most important characteristics of the nonlinear response even for the numerical results obtained for more complex waveguides.

The dispersion relation for the flexural mode can be easily obtained by substituting Eq. 2.8 into Eq. 2.7 (with $q(x, t) = 0$) and by solving for $k_F(\omega)$, yielding

$$k_F = \left(\frac{\rho A}{EI} \right)^{\frac{1}{4}} \omega^{\frac{1}{2}} \quad (2.9)$$

which captures the well-known dispersive behavior of flexural waves. Note that this model is only valid at relatively low frequencies and for a purely flexural (antisymmetric) mode, as a result of the constrain on the wavelength. For higher frequencies and/or non antisymmetric deformation, this dispersive model would have to be replaced by the Rayleigh-Lamb model, where we recall that the lowest antisymmetric Lamb mode A_0 is indeed well approximated by Eq. 2.9 but tends asymptotically to a linear behavior at high frequencies.

Plugging Eq. 2.8 into the expression for w in Eq. 2.6 (with $p(x, t) = 0$) leaves us with a nonlinear heterogeneous spatio-temporal partial differential equation in the variable u :

$$\rho A \frac{\partial^2 u}{\partial t^2} = EA \frac{\partial}{\partial x} \left[\frac{\partial u}{\partial x} + \frac{1}{2} \left(\frac{\partial u}{\partial x} \right)^2 \right] + F_1 + F_2 \quad (2.10)$$

where the two forcing terms are

$$F_1 = -\frac{1}{2} EA \mathcal{A}^2 k_F^3 \sin(2k_F x - 2\omega t) = -\frac{1}{2} \epsilon^2 EA k_F \sin(2k_F x - 2\omega t) \quad (2.11)$$

$$F_2 = \frac{1}{24} EA h^2 \mathcal{A}^2 k_F^5 \sin(2k_F x - 2\omega t) = \frac{\pi^2}{6} \epsilon^2 EA (h/\lambda_F)^2 k_F \sin(2k_F x - 2\omega t) \quad (2.12)$$

The last steps of the above equations are obtained invoking the two relations $\mathcal{A}k_F = \epsilon$ and $k_F = 2\pi/\lambda_F$. Under the constrain $\lambda_F/h \geq 10$, it can be easily shown that F_2 is at a much higher order when compared to F_1 , and therefore is ignored in the following analysis. In the interest of generality, we seek an expansion of u as:

$$u(x, t) = u^\alpha(x, t) + u^\beta(x, t) + \dots \quad (2.13)$$

where u^α represents the primary wave solution and u^β and above are small perturbations due to nonlinearity. Note that the only constraint here is that $u^\alpha \gg u^\beta$; the respective orders of u^α and u^β are not explicitly stated *a priori* and will be indirectly inferred from the solution of the equation. Substituting the truncated two-term expansion for u in Eq. 2.10 (with F_2 neglected), we obtain:

$$\frac{\rho}{E} \left(\frac{\partial^2 u^\alpha}{\partial t^2} + \frac{\partial^2 u^\beta}{\partial t^2} \right) = \frac{\partial^2 u^\alpha}{\partial x^2} + \frac{\partial^2 u^\beta}{\partial x^2} + \left(\frac{\partial u^\alpha}{\partial x} + \frac{\partial u^\beta}{\partial x} \right) \left(\frac{\partial^2 u^\alpha}{\partial x^2} + \frac{\partial^2 u^\beta}{\partial x^2} \right) + F_1 \quad (2.14)$$

We separately balance terms of commensurate order to obtain the following cascading PDEs

$$O(\epsilon^\alpha) : \rho \frac{\partial^2 u^\alpha}{\partial t^2} - E \frac{\partial^2 u^\alpha}{\partial x^2} = F_1 \quad (2.15)$$

$$O(\epsilon^\beta) : \rho \frac{\partial^2 u^\beta}{\partial t^2} - E \frac{\partial^2 u^\beta}{\partial x^2} = E \frac{\partial u^\alpha}{\partial x} \frac{\partial^2 u^\alpha}{\partial x^2} \quad (2.16)$$

In Eq. 2.15, u^α is to be interpreted as the leading-order solution due to the applied forcing function F_1 . In Eq. 2.16 all the terms containing mixed products of derivatives in u^α and u^β are recognized as higher-order terms and neglected, and u^β assumes the

significance of a perturbation solution driven by the forcing term $E \frac{\partial u^\alpha}{\partial x} \frac{\partial^2 u^\alpha}{\partial x^2}$ (which indirectly dictates the order of u^β).

The primary wave solution u^α is found from Eq. 2.15 following standard solution techniques for PDEs and consists of a (particular) forced solution and a homogeneous solution:

$$u_h^\alpha(x, t) = B_1 \sin(2k_F x - 2\omega t) + B_2 \sin(k_A(2\omega)x - 2\omega t) \quad (2.17)$$

where the subscript h has been added to denote that this solution is harmonic, to distinguish it from a non-harmonic contribution which will be discussed later on. The forced solution in Eq. 2.17 is obtained by assuming a harmonic form with the same frequency and wavenumber of the forcing term, for which it can be easily found that $B_1 = \frac{EA^2 k_F^3}{8(\omega^2 \rho - Ek_F^2)}$. The second term represents the homogeneous solution, which conforms to the linear dispersion relation of the medium (here the dispersion relation for axial waves in a rod $k_A(\omega) = \sqrt{\rho/E\omega}$) evaluated at the driving frequency 2ω , and where B_2 is to be determined from the boundary conditions. Incorporating the expression for k_F from Eq.2.9, the expression for B_1 can be rewritten as

$$B_1 = \frac{\mathcal{A}^2 k_F}{8(Ik_F^2/A - 1)} \quad (2.18)$$

In addition to the harmonic solution in Eq. 2.17, the axial problem also admits a non-harmonic solution. To provide a rationale for this statement, we recall the expression for the nonlinear axial force resultant F_{NL}^w , which is nonlinearly induced by the lateral displacement w . Using the expression for w , the leading order term of F_{NL}^w (i.e., the one yields F_1 in Eq. 2.10) can be expressed as

$$F_{NL}^w = \frac{1}{2}EA \left(\frac{\partial w}{\partial x} \right)^2 = \frac{1}{4}EA\mathcal{A}^2 k_F^2 [1 + \cos(2k_F x - 2\omega t)] \quad (2.19)$$

and we recognize a time-harmonic as well as a constant term. Note that the constant term vanishes when F_{NL}^w is plugged into Eq. 2.6 (due to the differentiation with respect to x), leading to the nonlinear wave equation (Eq. 2.10) already used above to obtain the harmonic solution. We now focus on the effect of the constant term which gives rise to a stationary solution. In the absence of external forces in the axial direction, the total internal force resultant should be equal to zero, yielding the static equilibrium

equation

$$EA \left[\frac{\partial u_{nh}}{\partial x} + \frac{1}{2} \left(\frac{\partial u_{nh}}{\partial x} \right)^2 + \frac{1}{4} \mathcal{A}^2 k_F^2 \right] = 0 \quad (2.20)$$

where only the constant term of F_{NL}^w has been retained and u_{nh} denotes a stationary, non-harmonic axial contribution to u . Invoking smallness considerations to neglect the higher order term in Eq. 2.20, we obtain the following first order differential equation:

$$EA \left(\frac{\partial u_{nh}}{\partial x} + \frac{1}{4} \mathcal{A}^2 k_F^2 \right) = 0 \quad (2.21)$$

to be solved for u_{nh} . A general solution of the above equation can be found as a bilinear spatio-temporal form $u_{nh}(x, t) = Gx + C_1 t + C_2$. The constant G can be easily found by substituting the solution in Eq. 2.21, yielding $G = -\frac{1}{4} \mathcal{A}^2 k_F^2$, while C_1 and C_2 are to be determined, along with B_2 , from the boundary conditions. Aggregating the non-harmonic term to the primary wave harmonic solution ($u^\alpha = u_{nh} + u_h^\alpha$), we obtain a complete solution for the primary axial response:

$$u^\alpha(x, t) = -\frac{1}{4} \mathcal{A}^2 k_F^2 x + C_1 t + C_2 + B_1 \sin(2k_F x - 2\omega t) + B_2 \sin(k_A(2\omega)x - 2\omega t) \quad (2.22)$$

Imposing the absence of second harmonic and non-harmonic terms at the boundary ($x = 0$) yields $C_1 = C_2 = 0$ and $B_2 = -B_1$, leading to the final expression:

$$u^\alpha(x, t) = -\frac{1}{4} \mathcal{A}^2 k_F^2 x + \frac{\mathcal{A}^2 k_F}{8(Ik_F^2/A - 1)} [\sin(2k_F x - 2\omega t) - \sin(k_A(2\omega)x - 2\omega t)] \quad (2.23)$$

The expression above allows for a few insightful observations. The first term represents a non-harmonic secular term that grows in amplitude as the wave propagates through the medium. It is important to recall that this model is based on the assumption of sustained harmonic excitation. We will see that, when the excitation is a compactly supported function (e.g., a tone burst), a non-harmonic component is visible (and possibly conspicuous) but it only grows within the support of the burst, after which it is preserved as a constant long-wavelength modulation in the tail of the signal. It is possible to recast Eq. 2.23 as:

$$u^\alpha(x, t) = -\frac{1}{4} \mathcal{A}^2 k_F^2 x + \frac{\mathcal{A}^2 k_F}{4(Ik_F^2/A - 1)} \sin \left(\frac{2k_F - k_A(2\omega)}{2} x \right) \cos \left(\frac{2k_F + k_A(2\omega)}{2} x - 2\omega t \right) \quad (2.24)$$

where the new form highlights that the wave can be described as a harmonic wave modulated in amplitude by another harmonic envelope function.

2.1.3 Comparison with 3D elasticity models and discussion

It is useful at this point to draw some parallels between the results obtained above and those available in the literature for generic plane waves in three-dimensional elasticity. Considering plane waves propagating in nonlinear isotropic solids, it has been shown that the analytical solution of the nonlinearly-generated second harmonics can be explicitly derived using perturbation techniques. For example, if the primary wave is a purely longitudinal wave propagating along x axis (i.e. $u \neq 0, v = w = 0$) due to an excitation $u(x = 0, t) = u_0 \sin \omega t, v(x = 0, t) = w(x = 0, t) = 0$, a longitudinal second harmonic is generated, whose expression was given by [56]:

$$u(x, t) = u_0 \sin \left(\frac{\omega x}{c_l} - \omega t \right) - \frac{\gamma}{8\rho} \left(\frac{\omega u_0}{c_l^2} \right)^2 x \cos \left(2 \frac{\omega x}{c_l} - 2\omega t \right) + \dots \quad (2.25)$$

where $\gamma = 3\rho c_l^2 + c_{111}$, and $c_l = \sqrt{\frac{\lambda+2\mu}{\rho}}$ is the speed of the linear longitudinal wave (with λ and μ being the Lamé moduli, and c_{111} and c_{166} appearing below are the third-order elastic constants). Similarly, if the primary wave is a purely transversal wave (i.e. $v \neq 0, u = w = 0$) due to a source excitation $v(x = 0, t) = v_0 \sin \omega t, u(x = 0, t) = w(x = 0, t) = 0$, no transverse second harmonic is observed, while a longitudinal second harmonic is generated as given by [55]:

$$u(x, t) = \frac{\tau \omega v_0^2}{4\rho c_t (c_t^2 - c_l^2)} \sin \left[\left(\frac{1}{c_t} - \frac{1}{c_l} \right) \omega x \right] \cos \left[\left(\frac{1}{c_t} + \frac{1}{c_l} \right) \omega x - 2\omega t \right] + \dots \quad (2.26)$$

where $\tau = \rho c_t^2 + c_{166}$, and $c_t = \sqrt{\frac{\mu}{\rho}}$ is the speed of the linear transverse wave. If we compare Eq. 2.24 and Eq. 2.26, we note that the two expressions are formally very similar, ultimately pointing at the unitary underlying mechanics of nonlinear problems. However, the two expressions feature a few important conceptual differences, which can be attributed to the specifics of the respective models. First, since Eq. 2.26 holds for an infinite 3D domain, it does not contain any geometric parameter; in contrast, the cross-sectional parameters of the beam play an important role in Eq. 2.23. Moreover, all the modes appearing in Eq. 2.26 are non-dispersive, while the solution in Eq. 2.23 is intrinsically dispersive in light of the characteristics of the $k_F(\omega)$ branch. From the examples mentioned above we can distinguish between two available classes of mode hopping mechanisms. The first, involving hopping within the longitudinal mode (from

lower to higher frequencies), can be defined as *intra-modal* hopping; the second, occurring from a transversal mode to the longitudinal mode, is referred to as *inter-modal* hopping. The flexural-to-axial case depicted in this Chapter for waveguides is another example of inter-modal hopping.

Equation 2.23 also allows establishing relative orders of magnitude for the terms in the solution. Since smallness is controlled by the nonlinear strain, it is logical to estimate orders in terms of strain. The axial strain associated with the primary wave is obtained through differentiation of Eq. 2.23 as:

$$\varepsilon_{xx}^\alpha(x, t) = -\frac{1}{4}\epsilon^2 + \frac{\epsilon^2}{4(Ik_F^2/A - 1)} \cos(2k_F x - 2\omega t) - \frac{k_A(2\omega)\epsilon^2}{8k_F(Ik_F^2/A - 1)} \cos(k_A(2\omega)x - 2\omega t) \quad (2.27)$$

where we have used $\mathcal{A}k_F = \epsilon$. As expected, all the terms in Eq. 2.27 are of order ϵ^2 . To estimate their relative contributions to the total nonlinear response, in Fig. 2.2 we plot the magnitude of their coefficients as a function of the wavenumber of the imposed excitation. It is convenient to express the wavelength as a multiple of the beam thickness h , i.e., $\lambda_F = nh$, which implies $k_F = 2\pi/nh$.

We observe that the order of both harmonic components varies with n . As we increase n , the contribution of the forced solution reaches an asymptotic value, while that of the homogeneous solution decreases, eventually decaying into a higher order contribution. The plot also features a vertical asymptote for $n \approx 2$. This corresponds to a value of k_F that leads to the establishment of phase matching conditions, for which the response grows secularly. Phase matching conditions are realized when, upon hopping, $k(2\omega) = 2k(\omega)$, which requires the existence of a branch for which doubling the wavenumber implies doubling the frequency. This requirement is naturally fulfilled in non-dispersive media characterized by linear dispersion branches. In our rod-beam model, this mechanism is available if the excitation lies on the axial non-dispersive branch; since, in our problem, the excitation is provided in the form of a flexural mode, this condition is met if we select an excitation frequency at the intersection between the axial branch $\omega = \sqrt{E/\rho}k$ and the flexural branch $\omega = \sqrt{EI/\rho Ak^2}$. Interestingly, this mathematical condition corresponds to setting the coefficient $8(Ik_F^2/A - 1)$ (at the denominator of B_1) equal to 0, which indeed makes B_1 go to infinity.

In closing, and in preparation for the simulation results in the next chapter, it is

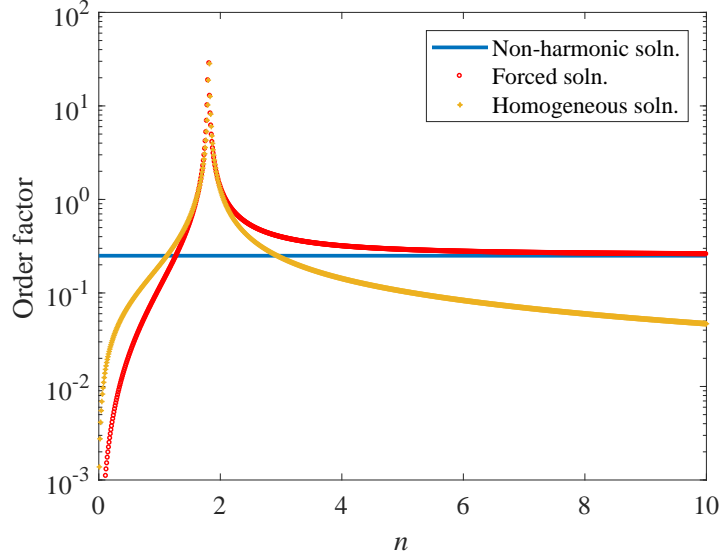


Figure 2.2: Relative magnitude of the three contributions in Eq. 2.27 (non-harmonic, homogeneous harmonic and forced harmonic) as a function of the nondimensional wavenumber parameter $n = 2\pi/k_F h$. We can see how the harmonic contributions peak for values of the wavenumber corresponding to the onset of phase matching conditions.

worth pointing out another difference between these theoretical predictions and the results of our simulations. We already pointed out that the dispersion relation of a Euler-Bernoulli beam is not valid for high frequencies and short wavelengths, where a Rayleigh-Lamb model is more appropriate. Since, at high frequencies, the lowest modes of the Rayleigh-Lamb spectrum are non-dispersive, and therefore there is no intersection between the modes, we conclude that phase matching conditions cannot be achieved for realistic beam structures (modeled as 2D solids). In the later chapters, we will show demonstrate how phase matching conditions can be instead activated in the nonlinear response of periodic waveguides through an appropriate design of the unit cell.

2.1.4 Numerical simulations

We perform now a suite of numerical simulations in geometrically nonlinear waveguides. Our domain, illustrated in Fig. 2.3(a), consists of a slender waveguide with length

$L = 5$ m and thickness $h = 0.01$ m. The domain is discretized with rectangular four-node isoparametric elements with aspect ratio of approximately 1. In our simulations, the shortest wavelength λ_{\min} is carefully chosen such that $\lambda_{\min}/h \approx 10$ and Euler-Bernoulli assumptions hold for the model. The ratio L_{el}/λ_{\min} (where L_{el} is the element size) is also carefully chosen to be small enough to guarantee avoidance of spurious numerical dispersion in the results. The body is modeled as a Saint-Venant Kirchoff (linear elastic) solid under plane-stress conditions, with the following test parameters: Young's modulus $E = 1$ MPa, Poisson's ration $\nu = 0.47$, density $\rho = 1100$ Kg/m³.

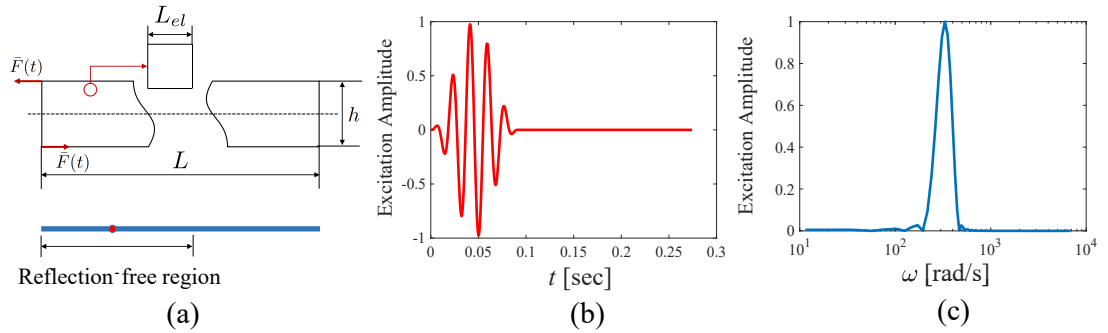


Figure 2.3: (a) Schematic of a homogeneous waveguide; the red dot located at $x = 1.2$ m marks the position of a virtual sensing point. (b-c) Temporal and spectral representation of a tone burst excitation.

The beam is subjected to a moment excitation applied at the left end through a pair of antiparallel forces, as shown in Fig. 2.3(a), in order to mimic pure bending conditions. The excitation is prescribed as a tone burst (shown in Figs. 2.3(b)-(c) along with its narrow frequency spectrum) obtained by modulating a five-cycle sine signal with carrier frequency ω using a Hann window, i.e., $\bar{F}(t) = \bar{F}_0 H(t) \sin(\omega t)$. ω is swept and specific values are given in the discussion of the plots. The peak force amplitude \bar{F}_0 is ramped to progressively increase the strength of the nonlinear effects.

The nonlinear equations of motion resulting from the FE model are integrated using an energy- and angular momentum-preserving time integration scheme [103]. The spatio-temporal response $(u(x, z, t), w(x, z, t))$ recorded at the nodes is presented below in two fashions. To capture the frequency content and highlight harmonic generation, time histories are extracted at a location on the neutral axis marked by the red dot in Fig. 2.3(a). Alternatively, spatial snapshots of the waves are sampled along the neutral

axis to capture the wavelength content and illustrate the multi-modal and dispersive characteristics of the medium.

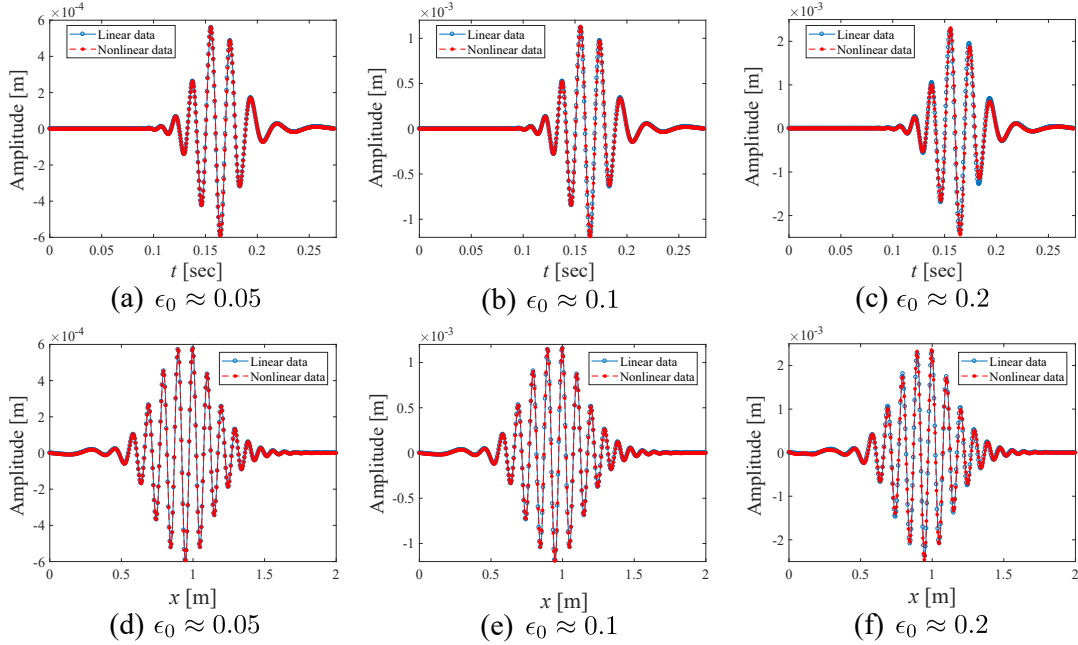


Figure 2.4: Lateral displacement response for increasing strength of nonlinearity (a-c) Temporal wave profiles, (d-f) Spatial wave profiles. The simulations suggest that the signature of nonlinearity on the flexural response is negligible in the considered excitation amplitude regime.

The response obtained under three different degrees of input nonlinearity (here quantified by the values of $\epsilon_0 = \mathcal{A}_0 k_F$, where \mathcal{A}_0 is the lateral displacement on the neutral axis induced at the edge of beam) is shown in Fig. 2.4. The results for nonlinear analysis (red dashed line with asterisk markers) are superimposed to those obtained for a corresponding linear model (blue line with circular markers) to show the increasing signature of nonlinearity when \mathcal{A}_0 grows. We can comfortably conclude that the signature of nonlinearity on the transversal response is negligible for low-to-mid amplitudes of excitation and fairly mild even for larger ϵ_0 , which provides a validation for the assumption made in the analytical model.

We now focus our attention on the axial motion for the intermediate case $\epsilon_0 \approx 0.1$. In Figs 2.5(a) and (d), the axial response (red line with asterisk markers) is plotted as

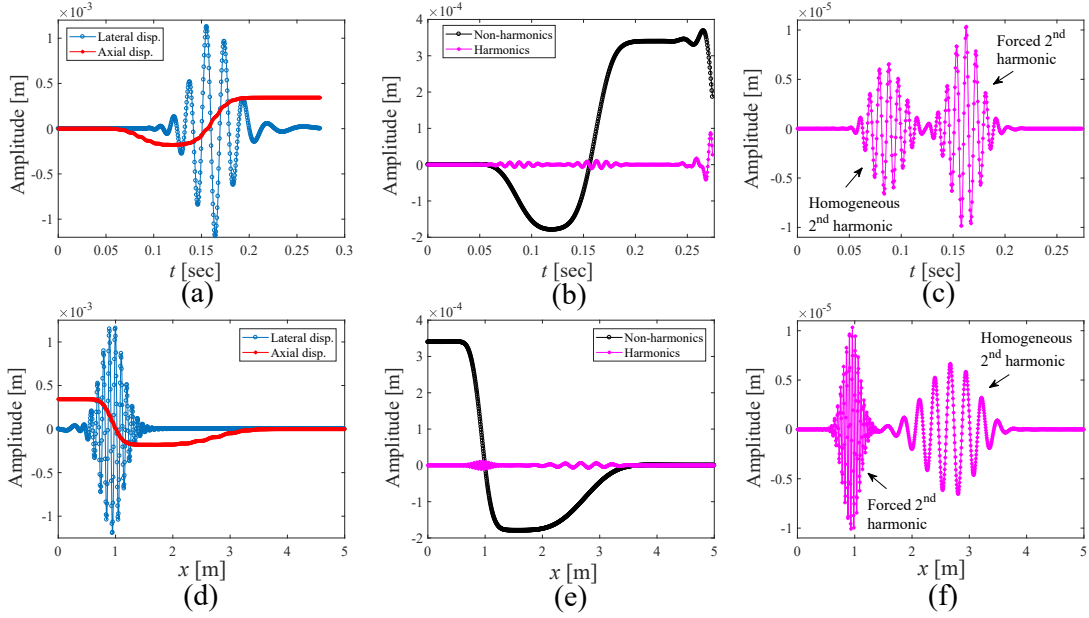


Figure 2.5: Axial displacement response for the intermediate case $\epsilon_0 \approx 0.1$ (a-c) Temporal wave profiles (d-e) Spatial wave profiles. From left to right: total response, filtered axial components, and zoomed detail of the 2^{nd} harmonic contributions.

a time history and as a spatial snapshot, respectively. The transversal response (blue line with circular markers) is also shown for reference. We immediately notice that the axial response carries a significantly stronger signature of nonlinearity. The most conspicuous effect is the coexistence of a harmonic and a non-harmonic component. This is highlighted in Figs. 2.5(b) and (e), in which a low- and high-pass filters are used to separate the two components (note that filtering introduces a spurious oscillatory behavior at the end of the temporal signal, therefore the last part of the signal must be ignored in the analysis). The generation of a non-harmonic modulation is in agreement with our analytical treatment; here, however, since we are exciting with a burst with compact support, as opposed to a sustained harmonic excitation, this effect has a morphologically different manifestation which results in a sigmoidal envelope modulation, consistently with the results obtained by [104] for similar excitations. Details of the harmonic components are shown in the zoomed plots of Figs. 2.5(c) and (f). Interestingly, in Fig. 2.5(c) we recognize two distinct packets traveling at different velocities with the same frequency 2ω . Fig. 2.5(f) reveals that the two packets are characterized

by largely different wavenumbers, which hints at interpreting the two packets as the transient counterparts of the two second-harmonic terms in Eq. 2.23.

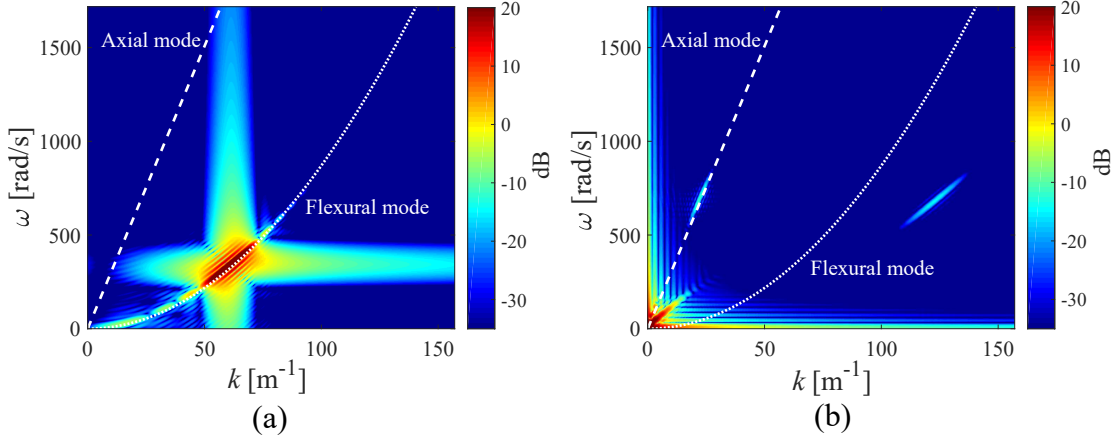


Figure 2.6: Spectral representation of numerical response (sampled along the neutral axis) (a) 2D-DFT of the lateral displacement: the spectral signature of the imposed flexural excitation lies on the flexural branch and no appreciable harmonics are observed for this degree of freedom (b) 2D-DFT of the axial displacement: it is possible to recognize the spectral signature of a strong long-wavelength modulation, of the homogeneous solution at $2\omega, k_A(2\omega)$, which conforms to the axial branch of the band diagram, and of the forced solution at $2\omega, 2k_F(\omega)$, which does not lie on any branch.

An alternative description of the nonlinear response is obtained by transforming the transversal and axial response (along the neutral axis) to the Fourier domain ($w(x, t) \rightarrow W(k, \omega)$, $u(x, t) \rightarrow U(k, \omega)$) via two-dimensional Discrete Fourier Transform (2D-DFT). Color maps of the spectral amplitude as a function of frequency and wavenumber for both degrees of freedom (W and U) are given in Figs. 2.6(a) and (b), respectively. The dispersion curves for the flexural ($k_F(\omega)$) and axial ($k_A(\omega)$) modes are superimposed for reference. In Fig. 2.6(a) we recognize a single feature at the prescribed frequency ω (and corresponding wavenumber $k_F(\omega)$), representing the fundamental flexural solution, which lies precisely on the parabolic dispersion branch for the flexural mode. The absence of other noticeable features confirms that the effects of nonlinearity on the flexural motion are negligible. Moreover, the agreement with the flexural branch tells us that our excitation is low enough in frequency that the transversal motion of the beam is still well captured by a flexural model (as opposed to the Rayleigh-Lamb

one). In Fig. 2.6(b) we recognize the three components of the nonlinear response (and their relative amplitudes): the long wavelength component, the homogeneous solution at the second harmonic lying on the axial branch ($2\omega, k_A(2\omega)$), and the forced solution at $2\omega, 2k_F(\omega)$, not lying on any branch.

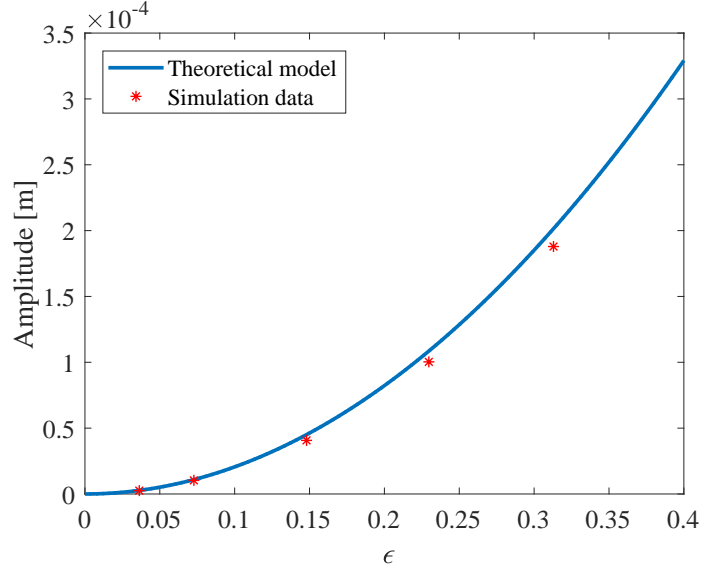


Figure 2.7: Amplitude of forced 2^{nd} harmonic vs. nonlinearity parameter ϵ . Comparison between analytical model and simulations. Theoretical model and results from simulations display remarkable agreement over a broad range of intensities of nonlinear effects (ϵ parameter).

To assess the consistency between analytical model and simulations, we repeat the analysis for five values of the magnitude of excitation and we plot the amplitude of the forced 2^{nd} harmonic against the nonlinearity parameter ϵ . The results, shown in Fig. 2.7 suggest a very good agreement between model and simulations, although, as expected, a certain discrepancy is observed for larger values of ϵ .

2.2 Nonlinear periodic waveguides with internal resonators

In this section, we shift our attention to one-dimensional periodic waveguides with internal resonators. In doing so, we are inspired by an attempt to maximize the energy tunneling and modal complementarity that can be achieved via inter-modal hopping.

The idea is based on the following conceptual pillars. Let us consider a waveguide with internal resonators which features a locally resonant bandgap: the unit cell mode shape for the acoustic mode calculated at the onset of the bandgap is expected to involve dramatic motion and/or deformation of the resonator. If we manage to design the unit cell such that a nonlinearly generated second harmonic would hop from the flexural mode to the onset of the bandgap, we will be able to achieve significant activation of the resonators, thus enriching the fundamental response with a type of mechanism that is completely unattainable, at those frequencies, in the linear regime and therefore functionally orthogonal to the imposed excitation. Furthermore, if the band diagram can be engineered such that phase matching conditions are established between the fundamental and the second harmonic, the strength of the observed energy tunneling will increase and we will be able to deploy conspicuous packets of energy to the resonators.

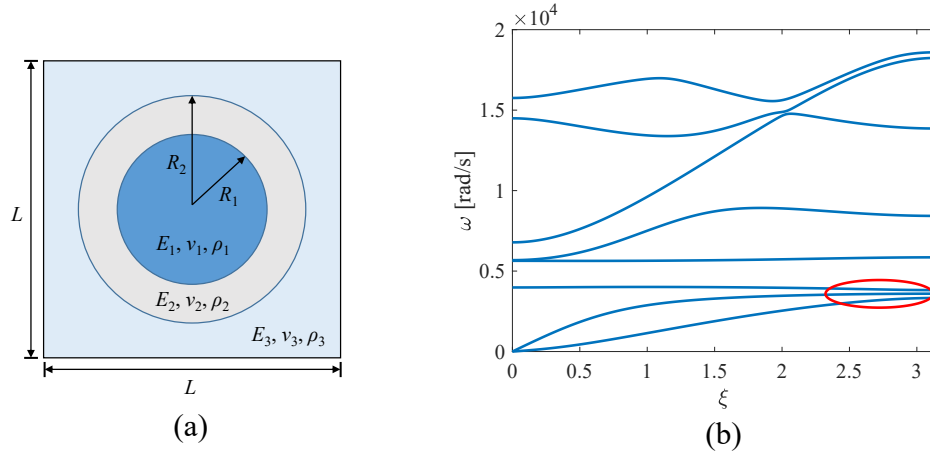


Figure 2.8: (a) Schematic of the unit cell with internal resonator (b) Band diagram of the corresponding linear structure featuring a locally-resonant subwavelength bandgap. The region marked by the red ellipse denotes the portion of the spectral plane corresponding to the onset of the bandgap, to which we need to hop in order to transfer energy to the resonators.

The unit cell under consideration consists of three material phases with the following test parameters: a heavy core ($E_1 = 14$ GPa, $\nu_1 = 0.42$, $\rho_1 = 11340$ Kg/m³), a soft rubber-like material annular layer ($E_2 = 1$ MPa, $\nu_2 = 0.47$, $\rho_2 = 1100$ Kg/m³), and a matrix material ($E_3 = 71$ MPa, $\nu_3 = 0.33$, $\rho_3 = 2700$ Kg/m³), and the geometric parameters are: $L = 0.02$ m, $R_1 = 0.005$ m, $R_2 = 0.0075$ m, as shown in Fig. 2.8(a).

The band diagram obtained from linear unit cell analysis is plotted in Fig. 2.8(b), where a locally-resonant bandgap is indeed observed above the acoustic modes. Then, we proceed to simulate a phononic waveguide consisting of 80 unit cells tessellated in the x direction. The excitation frequency is carefully chosen (in this case, we choose 2 kHz) to excite the flexural mode and trigger inter-modal hopping in a way that enables phase matching conditions to occur at the onset of the bandgap, which implies that the second harmonic will fall in the local resonance region shown in Fig. 2.8(b).

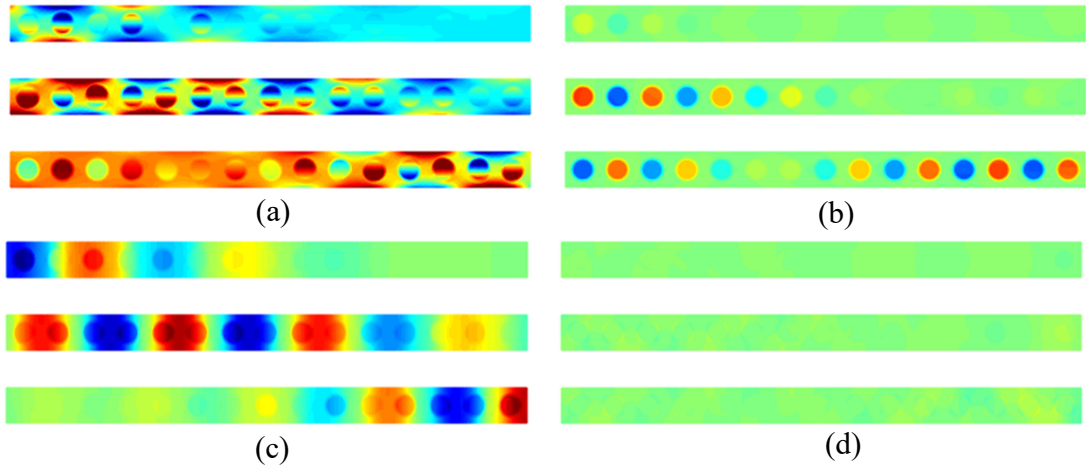


Figure 2.9: Snapshots of the wave evolution over a portion of the waveguide: color map proportional to the axial (a-b) and lateral (c-d) displacements (on the same color-bar scale): (a,c) Total wavefield (b,d) Filtered 2^{nd} harmonic. It is evident that the nonlinearly activated axial mode excites the resonators, which are marginally engaged by the flexural wave. The resonators undergo large axial motion that continues even after the tail of the excitation packet, thus effectively locally trapping the energy.

Color maps of the wavefield (for axial and flexural displacements) at three different time instances in a segment of the waveguide spanning from the 25^{th} to the 40^{th} unit cell are given in Fig. 2.9. A visual inspection of the axial displacement map (Fig. 2.9(a)) reveals a strong axial activation of the resonators that persists after the flexural packet has traveled through the considered section. The axial displacement map encompasses two distinct contributions. The first is associated with the fundamental *flexural* wave and is due to the inherent coupling between axial and flexural degrees of freedom typical of bending. This contribution has a linear antisymmetric profile through the thickness and displays the wavelength of the imposed excitation. Superimposed to that is a purely

axial field (with constant displacement across the thickness) which we recognize as the *axial wave* excited by hopping. This contribution has an oscillatory component and a long wavelength modulation, in agreement with theory. In Fig. 2.9(b) we filter out the fundamental harmonic and the non-harmonic components to isolate and better visualize the second harmonic. The color map suggests that the host structure is almost at rest while the resonators undergo large localized *axial* motion, which indicates that the resonators have indeed been activated according to the modal characteristics expected at the onset of the bandgap. Moreover, the wavelength of this contribution is smaller, as we have hopped to the π limit of the Brillouin zone. The large *axial* motion localized at the resonators is evidence of the modal enrichment that can be achieved by operating in the nonlinear regime. Finally, the amplitude of the oscillatory part of the nonlinearly generated axial wave is larger than in the previous example (without resonators) - here comparable to the fundamental solution. It is evident that here the local resonant mechanisms and the availability of phase matching conditions contribute to magnify the energy tunneling occurring between the modes.

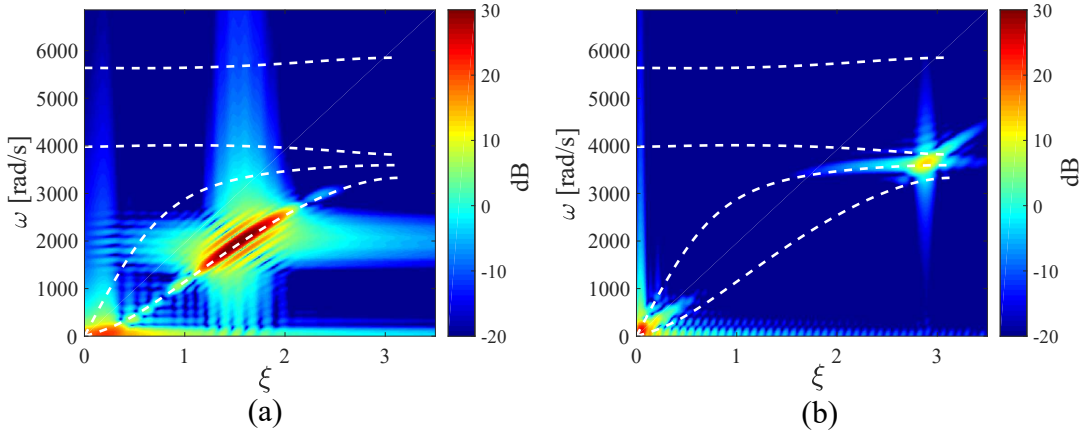


Figure 2.10: Spectral response of periodic waveguide with resonators (a) 2D-DFT of the lateral displacement (b) 2D-DFT of the axial displacement. The spectral representation confirms that the selected frequency of excitation has resulted into mode hopping to the onset of the bandgap.

The total and filtered lateral displacements are shown in Fig. 2.9(c) and (d), respectively, to provide further evidence that nearly all the energy associated with the

2^{nd} harmonic contributes to the axial motion of the resonators. The spectral representation of the full nonlinear response is plotted in Fig. 2.10. A graphical illustration of phase matching conditions is given in Fig. 2.10(b), where we observe an overlap between the forced 2^{nd} harmonic and the homogeneous 2^{nd} harmonic (which implies that the phase velocities of the two harmonic components are identical). This overlap causes a significant magnification of the total nonlinearly-generated 2^{nd} harmonic, which is a quintessential manifestation of phase matching conditions, as we discussed in section 2.1.3.

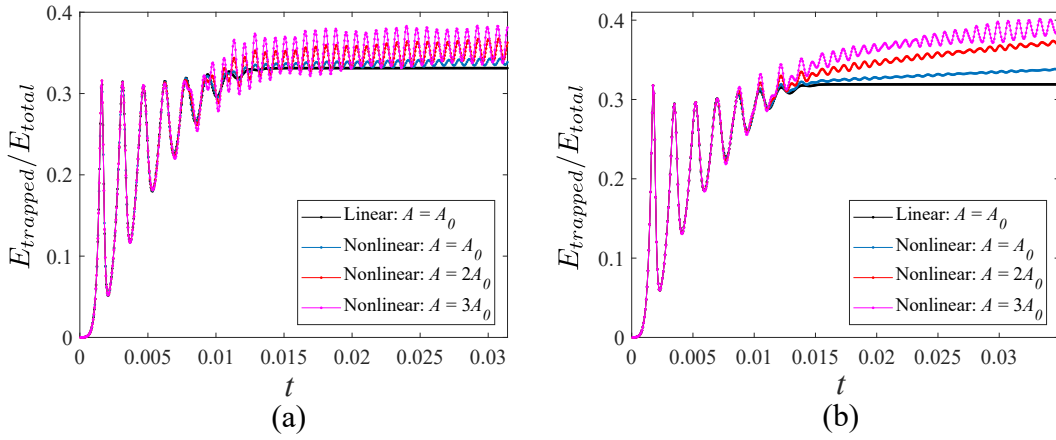


Figure 2.11: Energy trapped in the resonators $E_{trapped}$ vs. total energy E_{total} in the waveguide for two excitation frequencies. In both cases we observe a fast oscillation associated with the excitation of the resonators at the onset of the bandgap. Notably, the portion of the energy trapped in the resonators increases with the amplitude of excitation, indicating that the energy tunneling mechanisms are magnified by nonlinearity.

The most powerful statement about the role played by the resonators in promoting nonlinear energy tunneling comes from the analysis of how the energy transferred by hopping is partitioned among the different unit cell constituents. Let us recall that, in this instance of inter-modal hopping, a new and uncorrelated (in terms of MAC number) deformation mechanism is activated by geometric nonlinearity, which must be associated with some energy transfer from the primary wave. In Fig. 2.11(a), we plot the ratio between the energy trapped inside the resonators and the total energy in the waveguide for three different amplitudes of excitation and for the corresponding linear case, as reference. We first look at the linear case (black line with dot markers). The

ratio fluctuates during the excitation window before reaching a horizontal asymptote. The initial fluctuation is due to the redistribution of the energy that occurs within the structure as the primary wave is progressively injected into the system and affects an increasing number of cells; this effect decreases as more unit cells are engaged and subsides when the support of the packet is established over a finite number of cells. For the three nonlinear cases, the energy ratio keeps experiencing fluctuations even after the end of the excitation window. Interestingly, this fluctuation carries the higher-frequency signature of the second harmonic, which implies that the nonlinearly-generated 2^{nd} harmonic contributes directly to the energy trapped in the resonators. More importantly, we find that more and more conspicuous packets of energy are transferred to the resonators as we increase the amplitude of excitation, confirming that the increase in energy activation inside the resonators is not trivially due to a larger amount of total energy pumped into the system as the amplitude of excitation is increased, but rather depends on the nonlinear tunneling mechanisms that become more and more prevalent as the amplitude of excitation is ramped. We repeat the analysis for a slightly different excitation frequency (1.8 kHz) and the corresponding energy ratio is plotted in Fig. 2.11(b), revealing a similar scenario where the energy trapping in the resonators is even more pronounced due to a more precise establishment of phase matching conditions.

2.3 Conclusion

In this Chapter, we have investigated flexural-to-axial mode hopping in nonlinear waveguides analytically, by means of a simple rod-beam model, and numerically via finite element simulations. For the modeling part, we have been able to derive an explicit expression for the full nonlinear solution valid in a regime of weak nonlinearity and for special purely harmonic excitations. The solution provides useful insight into the propagation of coupled flexural-axial waves, highlighting unique features of the problem such as: the interplay between nonlinearity and dispersion, the role played by coupling in determining the available mode hopping scenarios, the opportunities for modal mixing with high modal complementarity, and the establishment of phase matching conditions. Through finite elements simulations, we have extended the investigation to nonlinear

periodic waveguides. We have explored different designs that lead to functionally complementary inter-modal hopping and we have explored the associated opportunities for functionality boosting. We have taken advantage of the fact that one component of the second harmonic solution conforms to the dispersion relation of the corresponding linear structure to engineer complex features of the nonlinear solution through a simple unit cell analysis. Based on this concept, we have parametrically swept the unit cell parameters (mass and geometry of the resonators) to identify configurations that enable phase matching conditions, thus achieving the transfer of conspicuous packets of energy to the resonating microstructure as we progressively increase the amplitude of excitation. This efficient and nonlinearly enhanced mechanism of energy tunneling to selected internal microstructural elements can become the building block of strategies for the design of tunable metamaterials with superior energy trapping and harvesting capabilities.

Chapter 3

Inter-modal and subwavelength energy trapping in nonlinear metamaterial waveguides

In this Chapter, we provide a definitive experimental demonstration of the tunneling effects achievable via inter-modal hopping in elastic metastructures. Guided by a finite-element based unit cell analysis, we design and test a locally resonant metamaterial waveguide, in which the availability of PMC enables an experimental observation of inter-modal hopping endowed with subwavelength energy trapping capabilities.

3.1 Preliminary analysis of linear response

After comparing advantages and disadvantages of different fabrication techniques and materials, we decided to manufacture a waveguide specimen via water-jet cutting from a sheet of acrylonitrile butadiene styrene (ABS) with the following material parameters: Young's modulus $E = 2.1374$ GPa, Poisson's ratio $\nu = 0.35$, density $\rho = 1040$ kg/m³. Preliminary experiments carried out on homogeneous strips of the same material suggested that the material has relatively low damping whose manifestation is limited to amplitude attenuation during propagation without any appreciable spectral distortion.

For this reason, the viscoelastic effects can be safely ignored in the model used in support of our experiments. The waveguide has dimensions $102\text{ cm} \times 2\text{ cm} \times 0.3556\text{ cm}$ and consists of 56 $1.75\text{ cm} \times 2\text{ cm}$ unit cells with internal resonators, as shown in Fig. 3.1. In order to lower the frequency spectrum of the resonators, we increase their mass by cutting a cylinder core (with radius 0.25 cm) out of the square domain at the center of each unit cell, and inserting a steel disk.

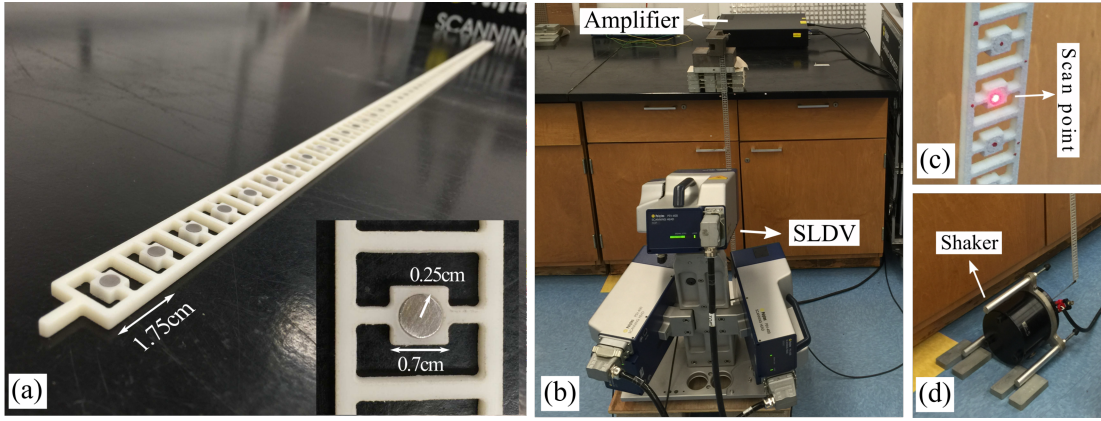


Figure 3.1: (a) Waveguide specimen with detail of a unit cell with steel-core resonator. (b) Experiment setup. (c) Detail of the scanned surface. (d) Shaker position for flexural excitation.

Before we proceed to assess the waveguide’s nonlinear response, it is useful to determine its linear dispersive characteristics. For a weakly nonlinear system, the homogeneous component of the nonlinear response has been shown to conform to the dispersion relation of the corresponding linear system [71]. As a result, we can use the linear band diagram to predict certain features of the nonlinear response and to design basic manipulation strategies involving harmonic generation. Specifically, from the inspection of the dispersion branches, we can predict the availability of tunneling mechanisms between the modes, i.e., the existence of $\omega - k(\omega)$ points on a dispersion branch (where ω is the frequency of the excitation and k is the wavenumber) such that the corresponding $2\omega - k(2\omega)$ points fall on a different branch, or on a higher-frequency zone of the same branch. We distinguish between intra-modal (axial-to-axial or flexural-to-flexural) and inter-modal (flexural-to-axial) tunneling mechanisms. Our focus here is on inter-modal tunneling. We can also identify opportunities for the establishment of phase-matching

conditions between fundamental and second harmonic, i.e., when $k(2\omega) = 2k(\omega)$.

We construct a finite element (FE) model of the unit cell using two-dimensional four-node isoparametric elements under plane-stress conditions and we perform a 1D Bloch analysis. In Fig. 3.2, we plot the band diagram along with the mode shapes at three representative spectral points (one on the flexural branch, two on the axial one). As expected, the two axial mode shapes feature purely axial (axis-symmetric) deformation profiles. Of the two, the one located on the folding part of the branch involves dramatic motion of the resonator. Let us now go through the following three conceptual steps. 1) Let us assume to prescribe a pure-bending excitation at a frequency lying within the range of the flexural mode. We expect the waveguide to experience a deformation that is purely flexural. 2) Let us choose the excitation frequency such that the nonlinearly-generated second harmonic can hop from the flexural mode to the folding part of the axial mode (close to the frequency cut-off of the mode). Some of the flexural energy externally pumped in the system will be necessarily transferred to cell deformation mechanisms that involve large degrees of axial motion of the resonators relative to the cells. 3) Finally, let us select the frequency-wavenumber excitation pair such that phase-matching conditions are established between the fundamental and the second harmonic. As a result, the magnitude of the observed energy tunneling (and associated trapping events) will be enhanced. This is the sequence of logically concatenated events that we intend to establish, observe and measure in our experiment.

Details of the experimental setup are shown in Fig. 3.1. A 3D Scanning Laser Doppler Vibrometer (SLDV, Polytec PSV-400-3D) is used to measure the in-plane response. The waveguide is hung vertically and clamped at the top end, as shown in Fig. 3.1(b). The excitation is imparted at the bottom end of the waveguide through an electrodynamic shaker (Bruel & Kjaer Type 4809) powered by a Bruel & Kjaer Type 2718 amplifier. When we intend to excite flexural waves at the fundamental harmonic, the shaker stinger is kept perpendicular to the waveguide and acts on an axial protrusion (visible in Fig. 3.1(a) to engage directly the neutral axis and mimic pure-bending conditions. To excite axial modes, the shaker is rotated to load the tip protrusion axially. It is worth pointing out that, despite a very careful setup, a certain amount of coupling between flexural and axial modes, as well as between in-plane and out-of-plane modes, is inevitable in practice due to unavoidable eccentricities in the stinger and warping of

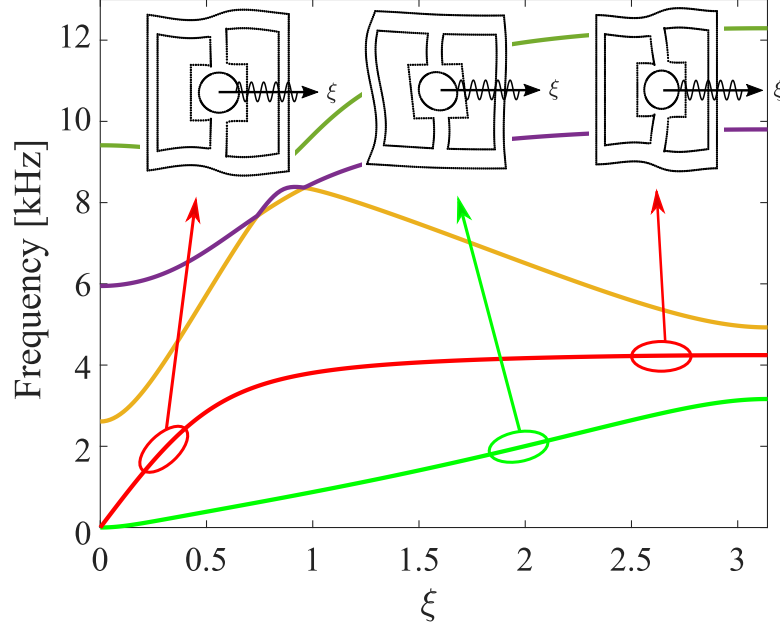


Figure 3.2: Band diagram of the waveguide with mode shapes shown for three representative spectral points. ξ is the non-dimensional wavenumber ($\xi = ka$, where k is the wavenumber and a is the length of the unit cell).

the soft waveguide.

As a next task, we reconstruct the band diagram from the experimental data. We excite the waveguide with a linear chirp with frequency range from 100 Hz to 8 kHz. The in-plane velocity time histories are measured along a straight line of scan points located directly on the resonators (Fig. 3.1(c)). These values are aggregated into a matrix of spatio-temporal data and fed to a 2D Discrete Fourier Transform (2D-DFT) to obtain spectral amplitude maps. In Fig. 3.3(a) and (b), we plot the spectral amplitude of the lateral and axial components of the response obtained through excitations prescribed laterally and axially, respectively. To better resolve the steering region of the axial mode, the chirp is locally replaced by a tone-burst with carrier frequency falling inside the desired interval (Fig. 3.3(c)). The dispersion relations obtained from the FE model are superimposed as dashed lines for comparison. Visual inspection suggests a very good agreement between experiments and model (we note a discrepancy of the cut-off frequency prediction for the axial mode, most likely due to an insufficiency of the finest FE mesh that we could afford in our desktop model).

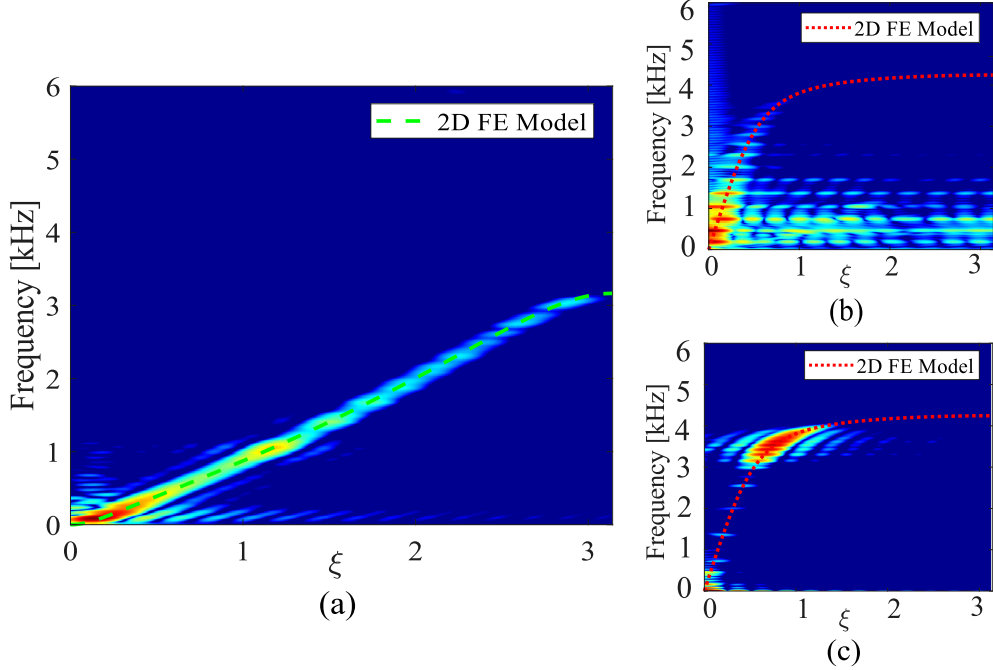


Figure 3.3: Experimentally reconstructed spectral response and comparison to FE data. (a) Lateral velocity field. (b) Non-dispersive region and (c) steering region of the axial mode.

3.2 Experimental evidence of inter-modal tunneling

We can now rely on the band diagram of Fig. 3.2 to find the excitation conditions necessary to trigger inter-modal flexural-to-axial tunneling while enabling phase-matching conditions. To this end, we excite the waveguide laterally with a tone-burst with carrier frequency 2 kHz, whose spectrum is plotted in Fig. 3.5(a). The amplitude of excitation is increased to ensure that sufficient geometrically nonlinear deformations are induced. The 3D response measured at a single scan point placed on the resonator of one unit cell (sufficiently far from the lateral excitation source) is shown in Fig. 3.4a. The wave packets corresponding to the lateral response are clearly recognized, suggesting that the ABS material can support wave propagation without dramatic wave distortion or attenuation. Components of the response in the axial and out-of-plane degree of freedom are also present in the response due to coupling effects. We apply a low- and band-pass filter to separate the fundamental harmonics and the second harmonics, which are

plotted in Fig. 3.4b and Fig. 3.4c, respectively. We observe a strong activation of axial waves at the second harmonic, whose amplitude is much higher than the signals for the other two degrees of freedom. Another noticeable feature of the axial second harmonic is the persistence of the oscillations, which implies that the energy is trapped in the resonator. The above observations are highly consistent with the results obtained from spectral analysis and the reconstructed deflection shapes discussed below.

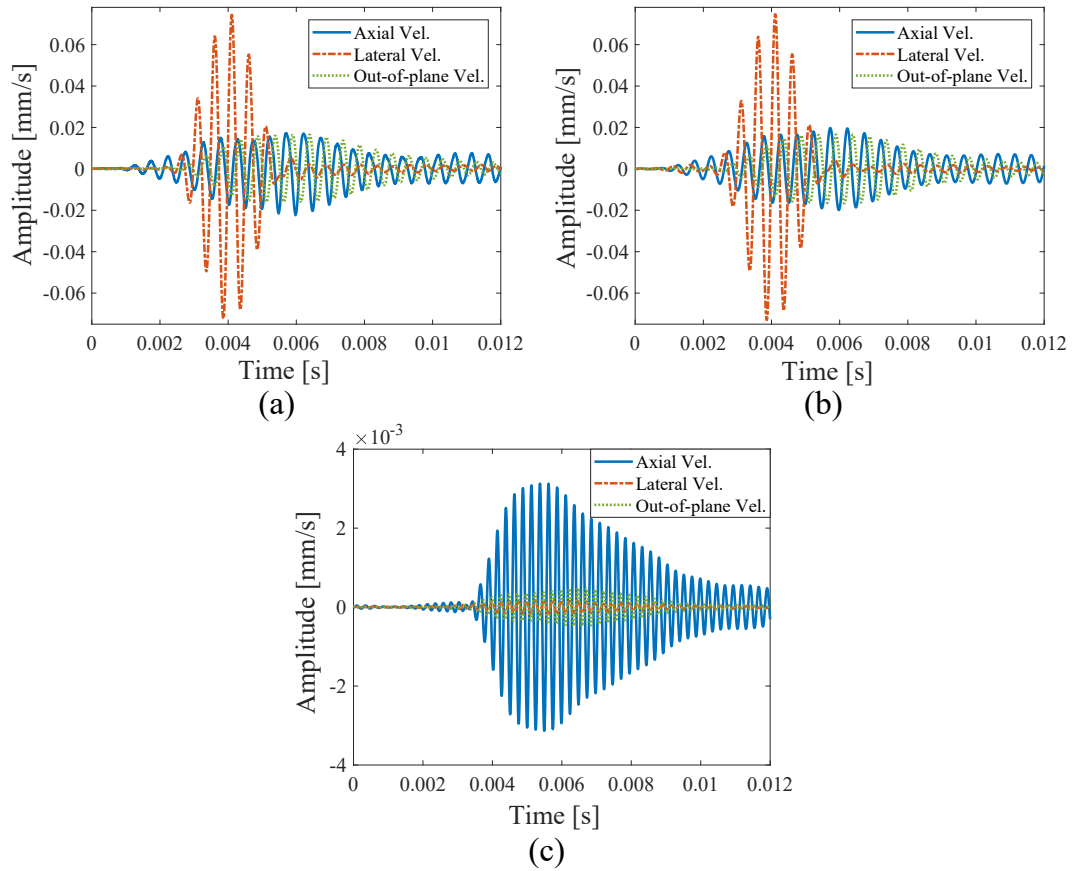


Figure 3.4: Experimental data collected at a single scan point: (a) Original velocity response. (b) Fundamental harmonics extracted by applying a low-pass filter. (c) Second harmonics extracted by applying a band-pass filter.

In Fig. 3.5(b), we plot the frequency spectrum of the total response measured at a representative point located at the mid point of the waveguide. In addition to the dominant contributions at the prescribed excitation frequency, we recognize a strong

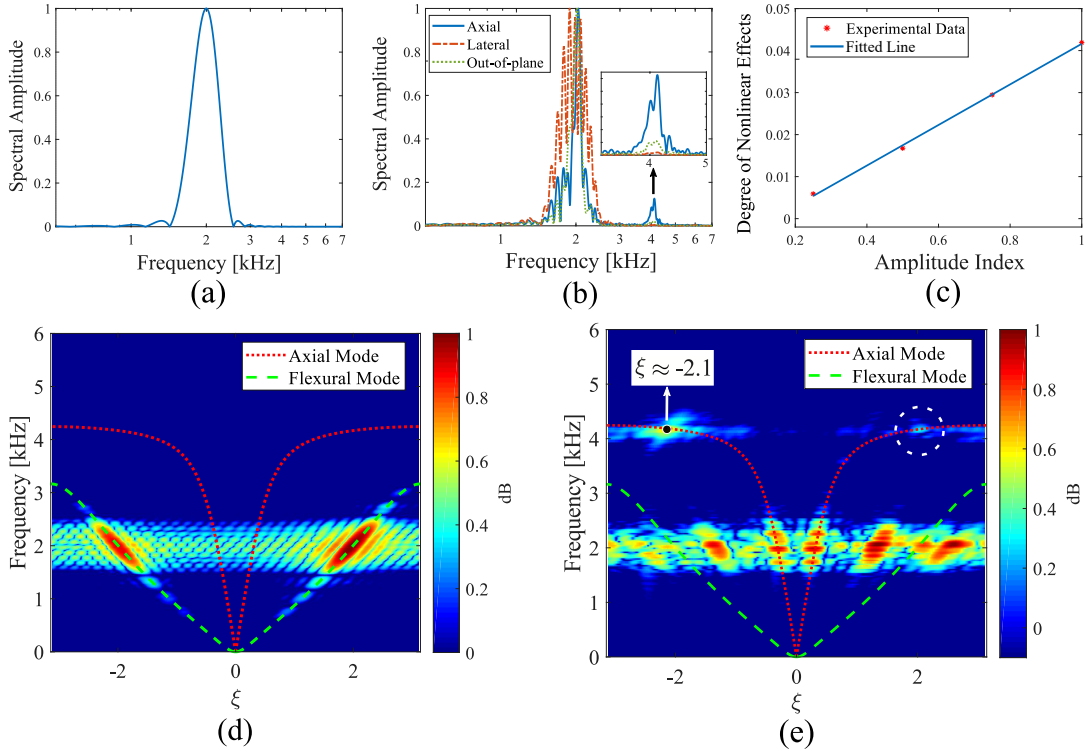


Figure 3.5: (a) Frequency spectrum of a tone-burst excitation. (b) Spectral representation of the response collected at a single scan point. (c) Ratio between amplitude of axial second harmonic and amplitude of fundamental flexural harmonic for four different amplitudes (scaled by the maximum value) of excitation. (d) and (e) Spectral representation (via 2D-DFT) of the lateral and axial response, respectively, sampled along the waveguide axis.

signature of second harmonic for the axial degree of freedom, while the second harmonic component for the lateral degree of freedom is negligible, in accordance with our previous theoretical findings [99]. In essence, the harmonic generation manifests as a highly mode-selective process in which the axial degrees of freedom dominate the second harmonic despite being a secondary mechanism (only due to coupling) in the fundamental harmonic.

In Fig. 3.5(c) we plot the ratio between the amplitude of the axial second harmonic A_{2A} and that of the flexural fundamental harmonic A_{1F} as a function of the amplitude of the fundamental harmonic A_{1F} , for four amplitudes of excitation. The non-constant of this ratio confirms the amplitude-dependent characteristics of the nonlinear response.

More specifically, the precise linear trend of the ratio tells us that the intensity of the second harmonic ultimately depends on the square of the amplitude of excitation, consistently with analytical solutions previously obtained for nonlinear waveguides [99]. Through this metric, we can also quantify the strength of the nonlinear effects observed in the response. As a result of the relatively soft modulus of the material and, more importantly, of the activation of phase-matching conditions, the magnitude of the nonlinear features approaches 4% of the amplitude of the fundamental wave, a full order of magnitude stronger than what reported in our previous study [72]. We also note that components of the second harmonic are also observed in the out-of-plane response (green dotted line in Fig. 3.5(b)).

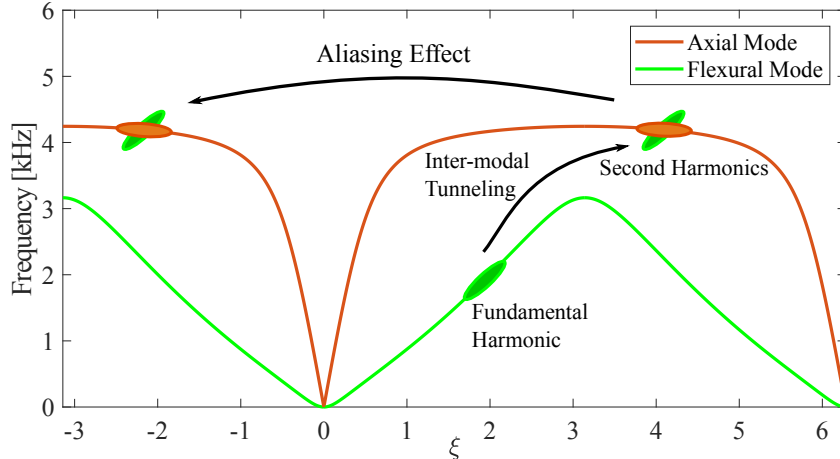


Figure 3.6: Schematic illustration of quadrant shift due to aliasing during inter-modal tunneling.

Next, we again resort to Fourier analysis to map the dispersive characteristics of the nonlinear response and identify the signature of the second harmonics. The normalized spectral amplitude (in dB units) of the lateral and axial responses is plotted in Fig. 3.5(d) and (e), respectively. The dispersion curves for the axial and flexural modes are superimposed for reference. In Fig. 3.5(d), the main contribution lies precisely on the flexural branch at the prescribed frequency, while no noticeable flexural features are detected at the second harmonic. In our experiment, the acquisition time is long enough to allow for the fundamental flexural wave to be reflected at the clamp. This is done to allow the spatial characteristics of the wave to be fully established (Note

that we are still in a purely propagating regime, and no standing wave conditions are established). The spatial feature at ω recorded in the left quadrant (negative ξ -space) represents the reflected flexural wave. Due to the damping mechanisms that are present in the structure, the reflected wave is significantly weaker, which can be noticed from the color intensity despite the visual magnification induced by the dB scale. In Fig. 3.5(e), around the excitation frequency, we observe the signature of several modes including: 1) an axial mode induced by the eccentricity in the excitation force; 2) the axial components of the flexural mode, due to bending coupling; 3) two other features associated with out-of-plane modes. At the second harmonic, we observe one dominant signature located in the negative ξ -space and consisting of two partially overlapping components, one conforming to the folding slope of the axial branch, the other having roughly the same slope of the fundamental flexural branch. These features can be recognized as the homogeneous and forced components of the second harmonic, respectively, which overlap here due to phase-matching conditions. The left quadrant location of these features can be explained invoking notions of aliasing, as graphically illustrated in Fig. 3.6. Since the wavenumber of the nonlinearly-generated second harmonic ξ_N (here twice the wavenumber of the fundamental wave, centered at 4.1, because of phase-matching conditions) falls outside the irreducible Brillouin zone, it cannot be accurately resolved by the 2D-DFT with our coarse spatial sampling frequency (here $\xi_S = 6.2$, dictated by the one-point per cell limit of our scan). From basic signal processing, the effective wavenumber of the reconstructed second harmonic ξ_R is expected to be

$$\xi_R = \xi_N - \xi_S \approx -2.1 \quad (3.1)$$

which matches the spectral location of the data. Careful inspection of the right quadrant (positive ξ -space) reveals a second feature at 2ω (highlighted by the dashed white circle in Fig. 3.5(e), albeit significantly smaller in amplitude. We recognize this as the left-going second harmonic due to the reflected component of the fundamental flexural wave. The negligible amplitude here can be attributed to the fact that this is a second-order effect generated by a reflected wave which, as stated above, is already significantly weaker than its incident counterpart due to damping. The right quadrant location of the reflected second harmonic can be explained invoking the same aliasing argument discussed above.

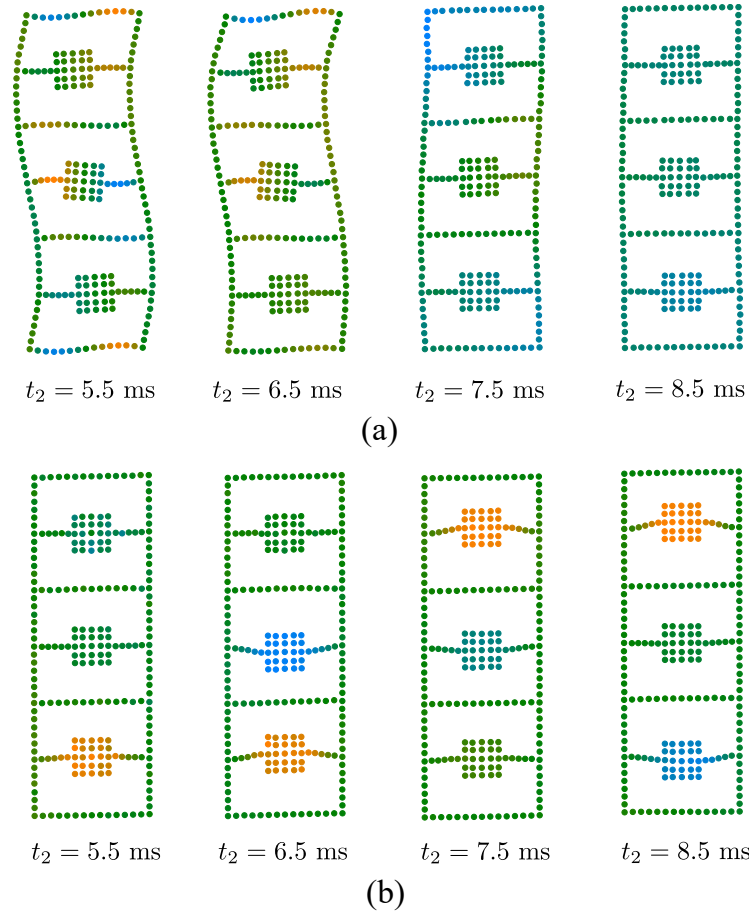


Figure 3.7: Experimentally reconstructed internal unit-cell response: snapshots of local wavefield details (spanning 3 cells) at four successive time instants. (a) Fundamental flexural wavefield. (b) Filtered wavefield at the second harmonic revealing nonlinear activation of axial resonant mechanisms and energy trapping.

It is important at this point to provide some guarantees that the signatures of nonlinearity observed in the response are predominantly due to the nonlinear mechanics of the problem rather than to other possible sources of nonlinearity, e.g., in the excitation/amplification system, or in the contact between the stinger and the structure. The spectral plot of Fig. 3.5(e) provides a rationale to support this notion. Consider that, from the perspective of the structure, a nonlinearity in the excitation would essentially be seen as a multi-frequency external input signal, which would therefore trivially activate all the branches of the band diagram that exist at any of the excited frequencies. Accordingly, an externally generated 2ω excitation component would predominantly produce an activation of the 2ω -portion of the axial branch that appears in the right quadrant of the band diagram. This is clearly not the case here where, instead, the positive- ξ axial branch remains essentially de-energized (except the very weak reflected second harmonic discussed above) and the wavenumber of the harmonic is dictated by the peculiar shape of the branches in the band diagram according to the requirements of phase matching conditions. The fact that the harmonic generation is subjected to these modal constraints suggests that the process is indeed controlled by the intrinsic mechanics of the problem. We conclude that, while undoubtedly there is a small nonlinear signature in the external excitation (which is indeed easily detected through an a-priori characterization of the shaker), the bulk of the nonlinear response is to be ascribed to the nonlinearity of the medium.

The multi-resolution capabilities of the 3D SLDV allow us to acquire detailed local snapshots of the wavefield. To this end, a dense grid of scan points spanning over 3 unit cells is used to reconstruct the deflection shapes shown in Fig. 3.7. The displacement of each point is magnified for visualization purposes and each point is color-coded proportionally to its axial displacement to highlight the activation of the resonators through inter-modal tunneling. In Fig. 3.7(a), we plot the fundamental wavefield at four time instants and we recognize the anti-symmetric lateral deflection profile typical of a flexural wave. In Fig. 3.7(b), we use a band-pass filter to distill the contributions at the second harmonic. Displacements and color contrast confirm the activation of strong short-wavelength axial mechanisms in the resonators. Compared to Fig. 3.7(a), we find that the activation of the resonators persists after the flexural packets have traveled through the scanned region, implying that some energy has been transferred

to the resonators and locally trapped. If we excited the waveguide axially at the nominal frequency ω , the wavelength would be much larger than the unit cell and therefore bypass the microstructure. To establish comparable effects, it would be necessary to excite at significantly higher frequencies lying on the folding portion of the axial branch. In this respect we can argue that, relatively to purely axial linear phononics, the trapping mechanisms of Fig. 3.7(b) display new subwavelength attributes that are directly enabled by inter-modal tunneling.

3.3 Conclusions

In conclusion, we have experimentally studied the propagation of nonlinear waves in a metamaterial waveguide with internal resonators. We have demonstrated the existence of strong inter-modal tunneling between flexural and axial mode, thus providing the strongest piece of evidence to date of modal mixing in nonlinear metamaterials. We have acquired detailed scans of the internal unit cell deformation features to visually confirm the modal conversion occurring during tunneling and the strong and persistent energy trapping established in the resonators. We have demonstrated that, by working in nonlinear conditions, strong axial trapping can be achieved even with purely flexural loads and, more importantly, even with low-frequency excitations whose long wavelengths prevent localization in the linear regime.

Chapter 4

Nonlinear harmonic generation in two-dimensional lattices

In Chapter 3, we have experimentally confirmed the existence of SHG in a 1D periodic waveguide featuring internal resonators. We now extend our focus to provide experimental validation of SHG and modal mixing phenomena in higher-dimensional periodic structures. While the general theoretical framework of this extension was laid down in [71], the problem still lacks definitive experimental observations. One of the main challenges arising in experiments carried out in 2D structural domains excited by point forces is that the strength of nonlinearity is not enough to trigger appreciable nonlinear signatures that survive the geometric attenuation inevitably experienced by propagating circular crests. This limitation has made the nonlinear effects observable in lattices of metallic or plastic material extremely elusive to detect and extract from the noise. In addition, PMC, which was key to the detection of strong SHG signatures in 1D structures, becomes unavailable in 2D structures subjected to point source excitations, because plane wave response cannot be established. To overcome this challenge, we design and realize a prototype lattice consisting of magnetic particles, which has the following advantages for the experimental observation of nonlinear wave propagation. On one hand, its compliance is conducive to relatively large displacements, compared to hard solid specimens, resulting in the activation of satisfactory levels of nonlinearity in the response. On the other hand, its discrete nature results in low modal complexity,

compared to a structural lattice, thus facilitating an unambiguous identification of all the nonlinear components. Before we perform the nonlinear analysis, it is useful to fully characterize the linear dispersion relation of the lattice. One special feature of magnetic systems is that each particle is in equilibrium at rest under the action of self-balancing static forces exchanged with its neighbors. To understand the underlying mechanism that links certain dynamical properties to these static forces, we need to take a step back to look at the simple illustrative example of a magnetic particle oscillator.

4.1 Introductory example: 2D magnetic particle oscillator

4.1.1 Analytical model

Consider the system of magnetized particles shown in Fig. 4.1. Assume that the four particles are identical with mass M and subjected to mutually repulsive forces. To establish the initial equilibrium conditions, a constant vertical force \mathbf{f} is applied on the free particle 4 (red dot) to balance the repulsive forces exerted on 4 by the fixed particles 1, 2, and 3 (black dots). The force between pairs of adjacent particles can be written in the form

$$\mathbf{F} = -\nabla\phi(r) = f(r)\mathbf{n} \quad (4.1)$$

where \mathbf{n} is the unit vector in the direction connecting the particles, and $f(r)$, in general, is taken to obey an inverse power law, i.e., $f(r) = br^{-a}$.

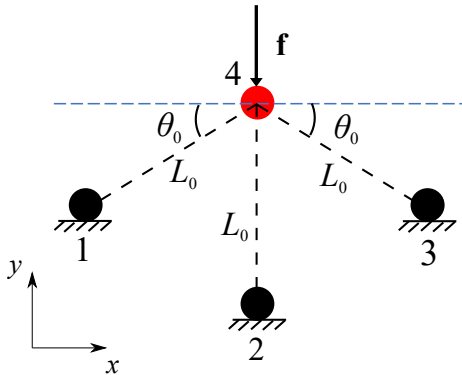


Figure 4.1: Schematic of a magnetic particle oscillator.

The governing equation for particle 1 is

$$\mathbf{M}\ddot{\mathbf{u}} - \sum_{i=1}^3 \mathbf{F}_i = \mathbf{f} \quad (4.2)$$

where $\mathbf{M} = \begin{bmatrix} M & 0 \\ 0 & M \end{bmatrix}$, $\mathbf{u} = \begin{Bmatrix} u \\ v \end{Bmatrix}$, $\mathbf{F}_i = f(r_i)\mathbf{n}_i$, $\mathbf{f} = -\sum_{i=1}^3 f(L_0)\mathbf{n}_i(\mathbf{u} = \mathbf{0})$, and

$$\begin{aligned} r_i &= \|L_0\mathbf{e}_i + \mathbf{u}\| \\ \mathbf{n}_i &= \frac{L_0\mathbf{e}_i + \mathbf{u}}{\|L_0\mathbf{e}_i + \mathbf{u}\|} \end{aligned} \quad (4.3)$$

where \mathbf{e}_i ($i = 1, 2, 3$) can be expressed as $\mathbf{e}_1 = \begin{Bmatrix} \cos \theta_0 \\ \sin \theta_0 \end{Bmatrix}$, $\mathbf{e}_2 = \begin{Bmatrix} 0 \\ 1 \end{Bmatrix}$, and $\mathbf{e}_3 = \begin{Bmatrix} -\cos \theta_0 \\ \sin \theta_0 \end{Bmatrix}$.

In the small perturbation limit, the linear stiffness matrix of the system can be obtained as

$$\begin{aligned} \mathbf{D} &= -\nabla_{\mathbf{u}} \sum_{i=1}^3 \mathbf{F}_i \Big|_{\mathbf{u}=\mathbf{0}} = \mathbf{D}_0 + \mathbf{D}^* \\ &= -\sum_{i=1}^3 f_r(L_0)\mathbf{e}_i \otimes \mathbf{e}_i - \sum_{i=1}^3 \frac{f(L_0)}{L_0} (\mathbf{I} - \mathbf{e}_i \otimes \mathbf{e}_i) \end{aligned} \quad (4.4)$$

where \mathbf{I} is the identity matrix and \otimes denotes the dyadic product. Detailed derivation of Eq. 4.4 is given in Appendix A. Interestingly, the treatment yields two distinct contributions to the stiffness matrix. In addition to the conventional term \mathbf{D}_0 , typical of generic particle systems with masses connected by linear springs, we obtain a secondary component, here denoted as \mathbf{D}^* , which depends on the initial self-balancing static forces between particles, i.e., $f(L_0)$.

The natural frequency ω_0 of the system is the only admissible root of the characteristic equation obtained by solving the eigenvalue problem

$$\left(-\omega^2\mathbf{M} + \mathbf{D}_0 + \mathbf{D}^*\right) \mathbf{u} = \mathbf{0} \quad (4.5)$$

To quantify the separate contributions of the two stiffness terms, we consider the reference natural frequency $\bar{\omega}_0$ obtained from the conventional model

$$\left(-\omega^2 \mathbf{M} + \mathbf{D}_0\right) \mathbf{u} = \mathbf{0} \quad (4.6)$$

In this example, each particle pair is treated as an ideal magnetic dipole with repulsive force expressed as [66, 105]

$$\mathbf{F} = \frac{3\mu_0 m^2}{4\pi r^4} \mathbf{n} \quad (4.7)$$

where μ_0 is the permeability of the medium and m is the magnetic moment. Combining Eq. 4.4 and Eq. 4.7, yields

$$\mathbf{D} = \sum_{i=1}^3 \frac{4\gamma}{L_0^5} \mathbf{e}_i \otimes \mathbf{e}_i - \sum_{i=1}^3 \frac{\gamma}{L_0^5} (\mathbf{I} - \mathbf{e}_i \otimes \mathbf{e}_i) \quad (4.8)$$

where $\gamma = \frac{3\mu_0 m^2}{4\pi}$. For an arbitrary choice of parameters ($M = 1$, $L_0 = 1$, $\gamma = 10^4$ with standard SI units used throughout the Chapter except where specified), the natural frequencies can be calculated from Eq. 4.5 and Eq. 4.6, and the values will be compared with simulation results provided in the following section.

4.1.2 Time-domain simulations

We perform time-domain numerical simulations assuming a harmonic excitation applied vertically on particle 1 (note that, in the simulation, the horizontal motion of the particle is constrained to ensure stability, as explained in Appendix B). The governing equation (Eq. 4.2) is integrated in time using the Verlet algorithm [106], and the magnitude of the harmonic response is recorded after steady-state conditions are reached. To effectively establish steady-state conditions, we add viscous damping to the system and we consider sufficiently long excitation times to fully dissipate the signature of the transient response. We also keep the amplitude of excitation sufficiently low to neglect the effects of nonlinearity (naturally embedded in the constitutive model of Eq. 4.7), which are not relevant for this treatment.

In Fig. 4.2, we plot the numerically-obtained frequency response function (FRF) of the complete system (red curve with o markers) for four different orientations of the slant links: $\theta_0 \in [0 \ \pi/6 \ \pi/4 \ \pi/2]$. We also superimpose the natural frequency

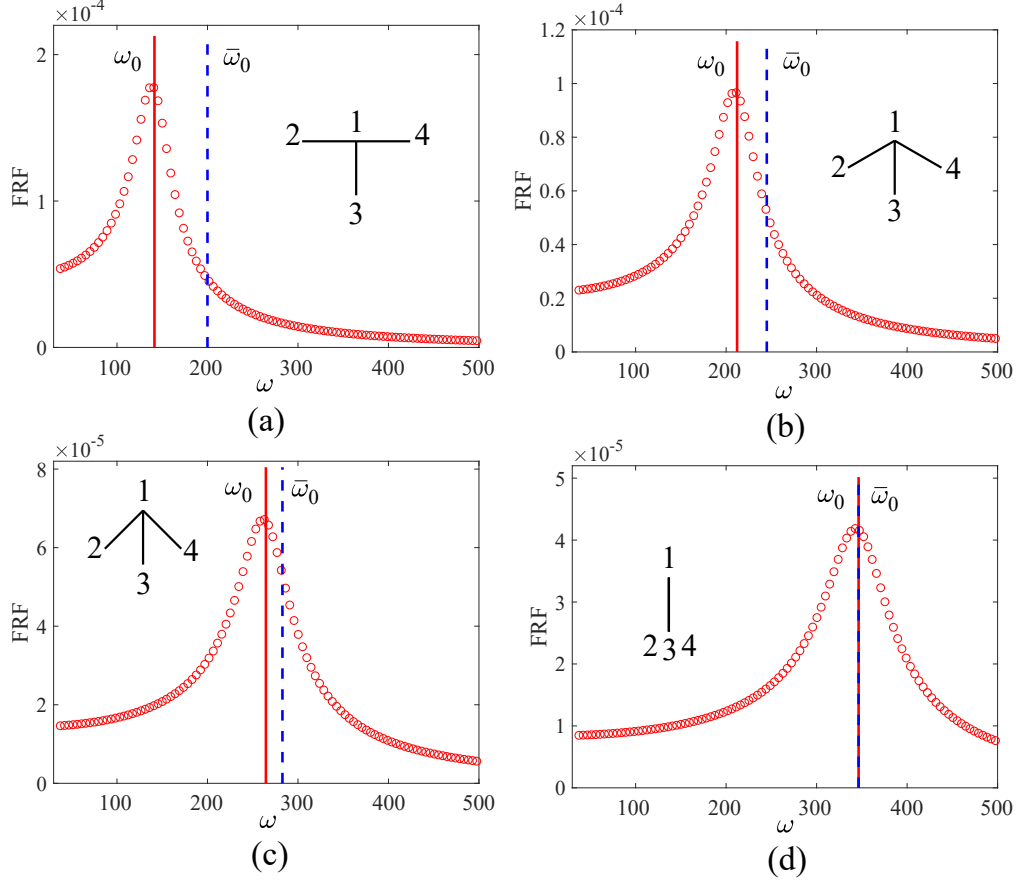


Figure 4.2: Frequency response function (FRF) of the complete systems for four configurations, sketched in the insets: (a) $\theta_0 = 0$, (b) $\theta_0 = \pi/6$, (c) $\theta_0 = \pi/4$, and (d) $\theta_0 = \pi/2$. The natural frequencies computed from the analytical models are also reported as vertical lines.

bar ω_0 (red line) and the reference frequency bar $\bar{\omega}_0$ (blue dashed line) predicted from Eq. 4.5 and Eq. 4.6, respectively. We observe that the computed natural frequencies match the peaks of the FRF curves. Since the numerical simulations are not subjected to any restrictive assumptions, as they involve updating the most general form of the interaction law at each integration step, this result confirms the validity of the complete model in Eq. 4.4. Moreover, we observe that the difference between ω_0 and $\bar{\omega}_0$ decreases as θ_0 increases. In the limit case of $\theta_0 = \pi/2$, the corresponding system is reduced to a 1D configuration and the two frequencies become identical. This result supports

our general remark anticipated earlier that the additional dynamical effect captured by \mathbf{D}^* (here manifests as the frequency difference $\Delta\omega_0 = \omega_0 - \bar{\omega}_0$) is germane to 2D configurations. This marks a fundamental difference with the terms depending on \mathbf{D}_0 , which do not vanish for 1D configurations. Another interesting feature is that, since the magnetic force is repulsive in our framework, the frequency difference $\Delta\omega_0$ is necessarily negative (softening effect). Finally, we note that, for certain parameter choices, a special condition may occur when $|\Re(\Delta\omega_0)|$ is no longer less than $\bar{\omega}_0$ or when the horizontal motion is not constrained, resulting in dynamical instabilities (a preliminary stability analysis of the magnetic system based on Eq. 4.8 is reported in Appendix B).

4.2 Wave propagation in 2D Repulsive Lattices

In this section, we shift our attention to wave propagation problems. Specifically, we theoretically and numerically investigate the propagation of waves in repulsive lattices of magnetized particles, demonstrating the effect of \mathbf{D}^* on the dispersion relation.

4.2.1 Analytical model

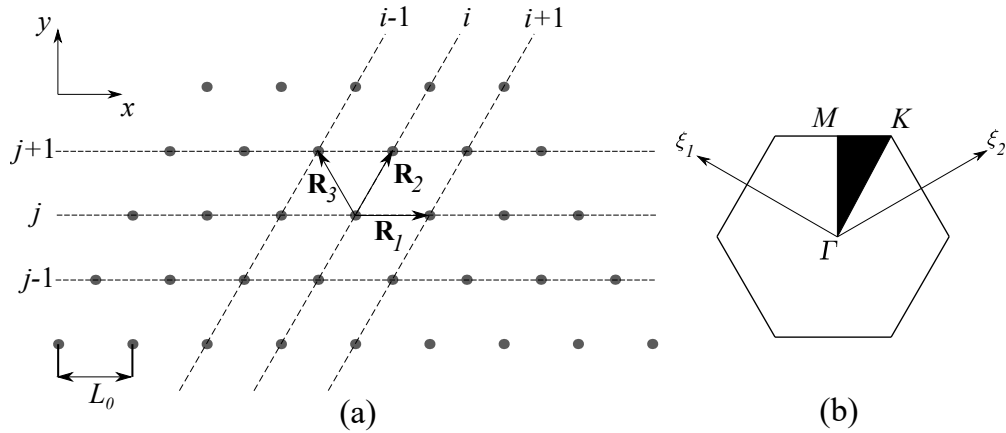


Figure 4.3: (a) 2D triangular lattice with basis vectors \mathbf{R}_2 and \mathbf{R}_3 . (b) First Brillouin zone with irreducible zone highlighted in black (ξ_1 and ξ_2 are the components of the non-dimensional wavevector in reciprocal space).

Consider a triangular lattice consisting of repulsive particles shown in Fig. 4.3. For

simplicity, each particle in the lattice is assumed to interact only with its nearest neighbors. The governing equation for a particle at location $\mathbf{R}_{i,j}$ can be written as

$$\mathbf{M}\ddot{\mathbf{u}}_{i,j}(\mathbf{R}_{i,j}, t) + \sum_{l=-3}^3 \mathbf{F}_l(\mathbf{u}) = \mathbf{0} \quad (4.9)$$

According to Eq. 4.1, the repulsive force \mathbf{F}_l between two adjacent particles takes the general form

$$\mathbf{F}_l(\mathbf{u}) = \begin{cases} f(\|\Delta\mathbf{u}_{\pm 1,0} \pm \mathbf{R}_1\|) \frac{\Delta\mathbf{u}_{\pm 1,0} \pm \mathbf{R}_1}{\|\Delta\mathbf{u}_{\pm 1,0} \pm \mathbf{R}_1\|} \\ \text{where } \Delta\mathbf{u}_{\pm 1,0} = \mathbf{u}_{i\pm 1,j} - \mathbf{u}_{i,j}, & \text{if } l = \pm 1 \\ f(\|\Delta\mathbf{u}_{0,\pm 1} \pm \mathbf{R}_2\|) \frac{\Delta\mathbf{u}_{0,\pm 1} \pm \mathbf{R}_2}{\|\Delta\mathbf{u}_{0,\pm 1} \pm \mathbf{R}_2\|} \\ \text{where } \Delta\mathbf{u}_{0,\pm 1} = \mathbf{u}_{i,j\pm 1} - \mathbf{u}_{i,j}, & \text{if } l = \pm 2 \\ f(\|\Delta\mathbf{u}_{\mp 1,\pm 1} \pm \mathbf{R}_3\|) \frac{\Delta\mathbf{u}_{\mp 1,\pm 1} \pm \mathbf{R}_3}{\|\Delta\mathbf{u}_{\mp 1,\pm 1} \pm \mathbf{R}_3\|} \\ \text{where } \Delta\mathbf{u}_{\mp 1,\pm 1} = \mathbf{u}_{i\mp 1,j\pm 1} - \mathbf{u}_{i,j}, & \text{if } l = \pm 3 \end{cases} \quad (4.10)$$

where $\mathbf{R}_1 = L_0\mathbf{e}_1 = L_0 \begin{Bmatrix} 1 \\ 0 \end{Bmatrix}$, $\mathbf{R}_2 = L_0\mathbf{e}_2 = L_0 \begin{Bmatrix} 1/2 \\ \sqrt{3}/2 \end{Bmatrix}$, and $\mathbf{R}_3 = L_0\mathbf{e}_3 = L_0 \begin{Bmatrix} -1/2 \\ \sqrt{3}/2 \end{Bmatrix}$.

Assuming that the displacement $\Delta\mathbf{u}$ is infinitesimally small, Eq. 4.9 can be linearized as

$$\mathbf{M}\ddot{\mathbf{u}}_{i,j} + \sum_{l=1}^3 \left\{ [f_r(L_0)\mathbf{e}_l \otimes \mathbf{e}_l] \Delta\mathbf{u}_l \right\} + \sum_{l=1}^3 \left\{ \left[\frac{f(L_0)}{L_0} (\mathbf{I} - \mathbf{e}_l \otimes \mathbf{e}_l) \right] \Delta\mathbf{u}_l \right\} = \mathbf{0} \quad (4.11)$$

$$\text{where } \Delta\mathbf{u}_l = \begin{cases} \mathbf{u}_{i+1,j} + \mathbf{u}_{i-1,j} - \mathbf{u}_{i,j}, & \text{if } l = 1 \\ \mathbf{u}_{i,j+1} + \mathbf{u}_{i,j-1} - \mathbf{u}_{i,j}, & \text{if } l = 2. \\ \mathbf{u}_{i-1,j+1} + \mathbf{u}_{i+1,j-1} - \mathbf{u}_{i,j}, & \text{if } l = 3 \end{cases}$$

A plane wave solution of Eq. 4.11, with wave vector \mathbf{k} and frequency ω , is given as

$$\mathbf{u}_{i,j} = A\phi e^{i(\mathbf{k}\cdot\mathbf{R}_{i,j} + \omega t)} \quad (4.12)$$

where A is a constant, and $\phi = \begin{Bmatrix} \phi_u \\ \phi_v \end{Bmatrix}$ is a modal vector. According to Floquet-Bloch theorem, the relations between displacements at neighboring sites can be expressed as

$$\mathbf{u}_{i\pm 1,j\pm 1} = \mathbf{u}_{i,j} e^{i(\pm\mathbf{k}\cdot\mathbf{R}_1 \pm \mathbf{k}\cdot\mathbf{R}_2)} \quad (4.13)$$

Substituting Eq. 4.12 and Eq. 4.13 into Eq. 4.11, yields the wavevector-dependent eigenvalue problem

$$\left[-\omega^2 \mathbf{M} + \mathbf{D}(\mathbf{k}) \right] \phi = \mathbf{0} \quad (4.14)$$

where

$$\begin{aligned} \mathbf{D}(\mathbf{k}) = & 2 \sum_{l=1}^3 \left\{ f_r(L_0) \mathbf{e}_l \otimes \mathbf{e}_l [\cos(\mathbf{k} \cdot \mathbf{R}_l) - 1] \right\} \\ & + 2 \sum_{l=1}^3 \left\{ \frac{f(L_0)}{L_0} (\mathbf{I} - \mathbf{e}_l \otimes \mathbf{e}_l) [\cos(\mathbf{k} \cdot \mathbf{R}_l) - 1] \right\} \end{aligned} \quad (4.15)$$

is a wavevector-dependent stiffness matrix. Again, we observe the appearance of two terms in the stiffness matrix. Canonically, the linear dispersion relation of the magnetic system is obtained by solving the eigenvalue problem for wavevectors along the contour of the irreducible Brillouin zone. Based on the conventional stiffness matrix, we can also define a reference system, whose dispersion relation is obtained from the following eigenvalue problem

$$\left[-\omega^2 \mathbf{M} + \mathbf{D}_0(\mathbf{k}) \right] \phi = \mathbf{0} \quad (4.16)$$

where $\mathbf{D}_0(\mathbf{k})$ is the first term of $\mathbf{D}(\mathbf{k})$ in Eq. 4.15.

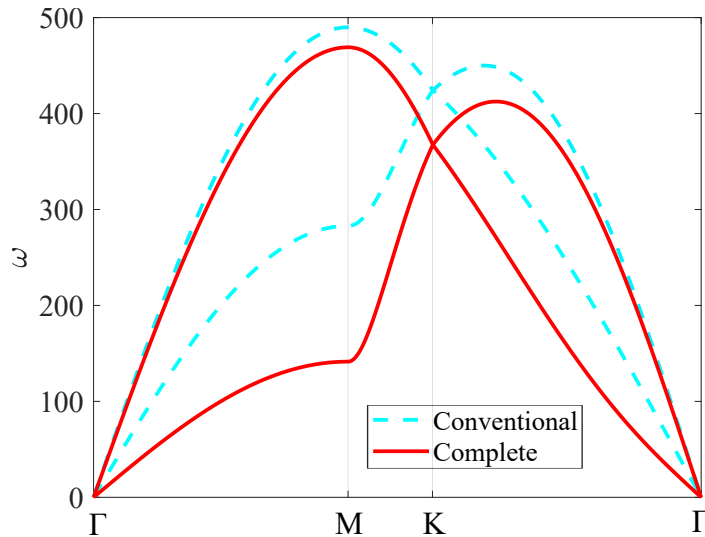


Figure 4.4: Dispersion relations of the repulsive lattice obtained from a complete and conventional (reference) models.

In Fig. 4.4, we plot the band diagram (red curves) of the 2D triangular repulsive lattice with magnetic interaction law (according to Eq. 4.7), and we superimpose the reference one (light blue dashed curves) obtained solving Eq. 4.16. Clearly, $\mathbf{D}^*(\mathbf{k})$ (i.e., the second term in Eq. 4.15) has significant influence on the dispersion relation of the repulsive lattice, especially for the first band.

4.2.2 Full-scale simulations

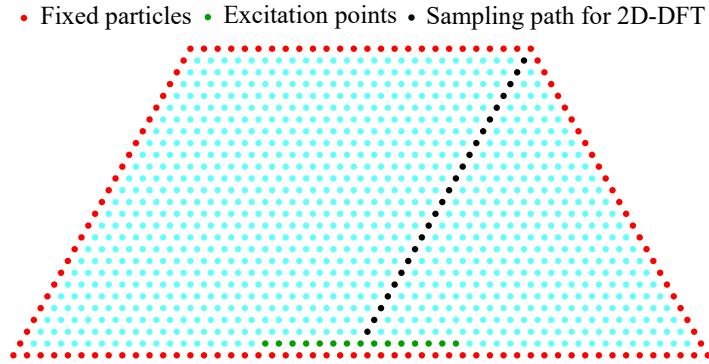


Figure 4.5: Finite lattice used in full-scale simulation

To validate our analytical model, we perform a suite of full-scale simulations to obtain the wave response of a finite lattice (shown in Fig. 4.5) and we compare it against that of a corresponding reference system. The particles located on the boundary (red dots) are fixed in order to establish initial equilibrium conditions. The objective is to numerically reconstruct the band diagram and compare it against that of a corresponding reference system. We consider wavevectors \mathbf{k} sampled along the Γ -M direction, which correspond to wave propagation in the vertical direction. Nearly plane-wave conditions are established by considering an array of excitation points collocated at the particles denoted as green dots in Fig. 4.5. The force excitation is prescribed as a five-cycle tone burst with carrier frequency Ω_0 chosen to fall within the frequency range of the first (shear-dominant) and of the second (longitudinal) modes, respectively. A small-amplitude force is applied in the horizontal (vertical) direction to optimally excite the shear (longitudinal) mode in the linear regime.

The spatio-temporal displacement response is sampled at nodes located along lattice vector \mathbf{R}_2 (black dots in Fig. 4.5) and transformed via 2D Discrete Fourier Transform

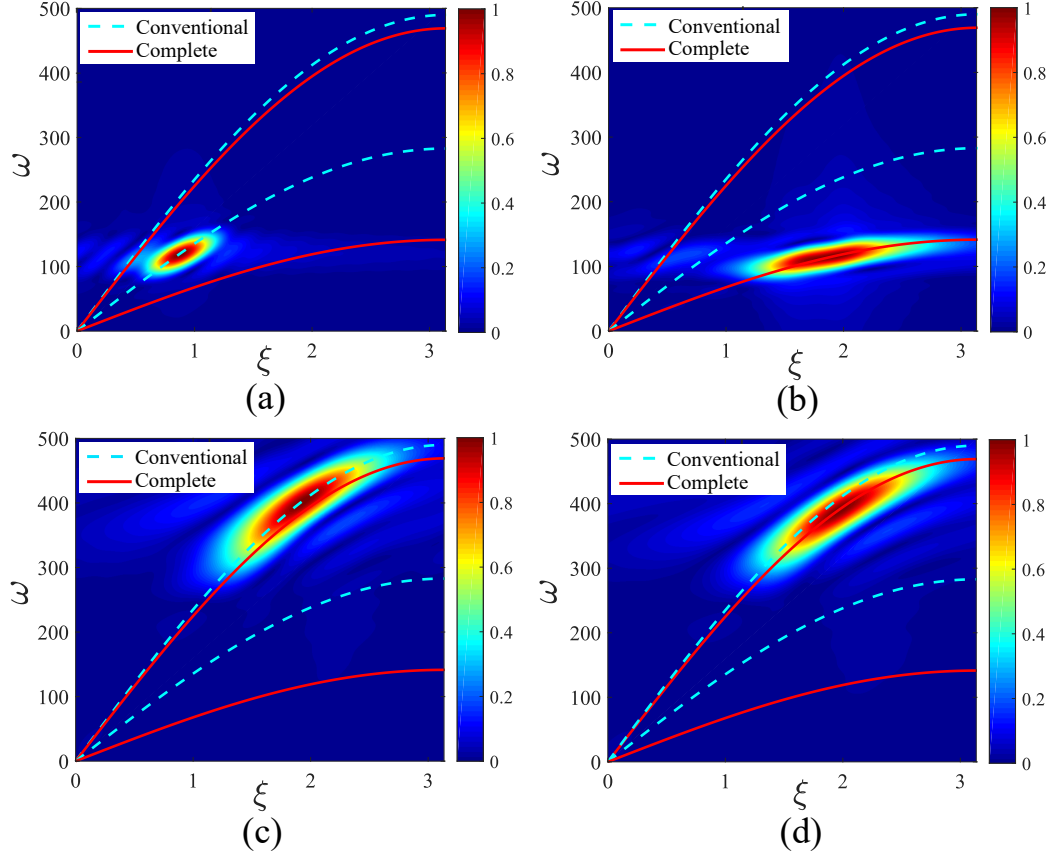


Figure 4.6: Spectral response from numerical simulations compared against band diagrams from Bloch analysis. (a) and (b) Response to excitation at $\Omega_0 = 120$ rad/s. (c) and (d) Response to excitation at $\Omega_0 = 400$ rad/s. (a) and (c) Response of the conventional (reference) system; (b) and (d) Response of the complete system.

(2D-DFT). We perform and compare two simulations. In the first, which we refer to as “complete simulation”, we update at each time step the most general form of the internal force (both its magnitude and direction) based on Eq. 4.10. The second is a conventional small-amplitude linear simulation, in which only the magnitude is updated at each step.

For an excitation at $\Omega_0 = 120$ rad/s (in the shear mode range), the normalized spectral amplitude maps obtained from the complete and conventional simulations are

plotted in Fig. 4.6(a-b), respectively. For excitation at $\Omega_0 = 400$ rad/s (in the longitudinal mode range), the results are plotted in Fig. 4.6(c-d). From a visual inspection, we observe that the results from the complete simulation match the dispersion relation predicted using the complete analytical model (i.e., Eq. 4.14), while the conventional simulation results in large dispersion deviations for the shear mode and minor ones for the longitudinal mode. However, it shows a good agreement with the conventional spring-mass model, which implies that the overlooking of \mathbf{D}^* is “forgiving” if conventional treatments are implemented in both numerical and analytical models. These results numerically confirm the inclusion (or lack thereof) of \mathbf{D}^* bears non-negligible modal-selective effects on the prediction of the dispersive behavior of repulsive lattices.

4.3 Experiments on magnetic prototypes

Through the above-developed theoretical framework, we can better understand and predict the dynamical behavior of interacting particle systems. Guided by an analytical model proposed based on this framework, we perform a series of experiments to investigate both the linear and nonlinear behavior of the prototype lattice.

4.3.1 Experimental characterization of linear behavior

The specimen used for our tests, shown in Fig. 4.7(a), consists of an array of pillars arranged to form a triangular lattice occupying a half-hexagonal domain. Each pillar in the interior lattice consists of a magnetic ring (Grade N42, with 1/4 inch outer diameter, 1/16 inch inter diameter and 1/8 inch thickness) inserted at the tip of a slender Aluminum beam (1/16 inch in diameter) whose other end is plugged into an Acrylic base through a drilled hole. For the exterior pillars, the magnets are simply glued to the tips of thick beams (1/4 inch in diameter) also plugged into the base and featuring large bending stiffness to effectively establish fixed boundary conditions along the contour of the hexagonal domain. The magnets are arranged as to experience side-by-side repulsive interactions in their own plane, and each magnet is initially in equilibrium under the action of the self-balancing static forces exerted by its neighbors. The configuration guarantees that, for the amplitudes of interest for this study, the motion of the magnets remains confined within the plane of the lattice.

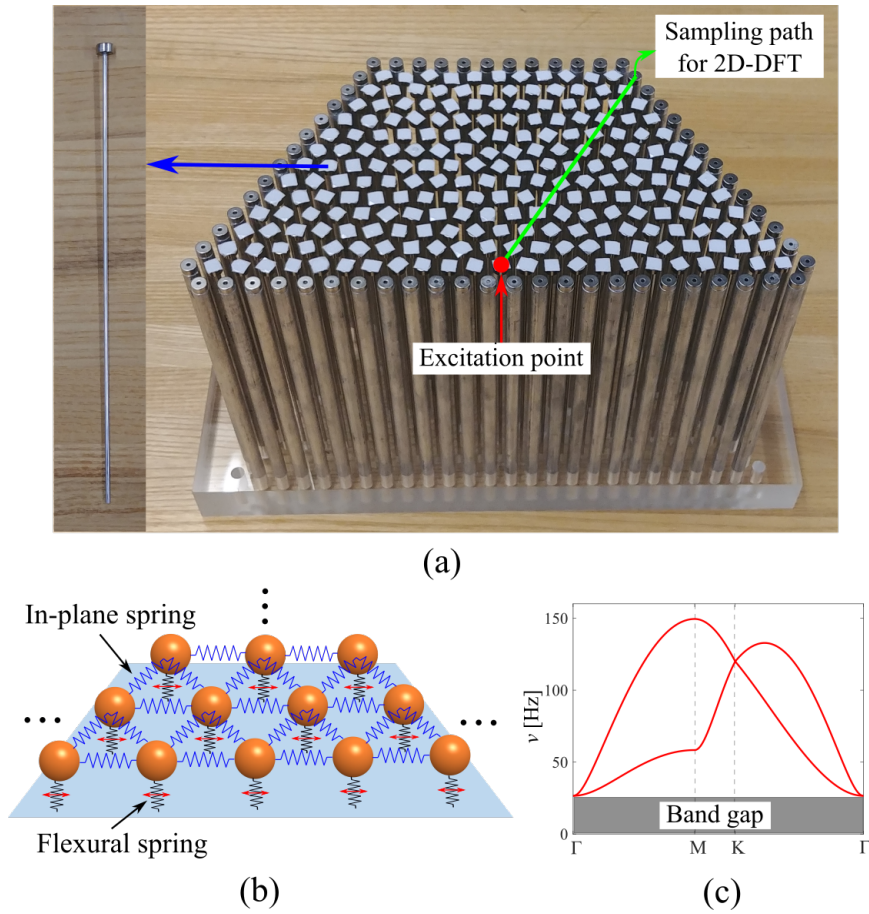


Figure 4.7: (a) Lattice specimen consisting of magnets supported by thin beams in the interior (shown in the inset) and thick beams along the boundary. The interior magnets are covered by reflective tapes to enhance laser measurements. (b) Equivalent spring-mass model of the lattice, showing the function of the pillars acting as an elastic foundation. (c) Linear dispersion relation obtained from the analytical model, accounting for the effect of the static inter-particle repulsive forces.

As shown in Fig. 4.7(b), the system is modeled as a triangular spring-mass lattice in which each node is connected to ground through a flexural spring that captures the elastic foundation effect of the supporting beam. The in-plane repulsive interaction between neighboring magnets is modeled as a nonlinear spring featuring an inverse power law $f(r) = \beta r^{-\alpha}$, with $\alpha = 4.5824$ and $\beta = 1.6209 \times 10^{-10}$. Here, the parameters have been obtained by fitting the force-displacement relation between two magnets acquired experimentally through a micrometer equipped with a highly sensitive load cell (details available in Appendix C). The spring constant of the flexural springs in the foundation is taken as the equivalent flexural stiffness of a cantilever beam with the cross sectional and material properties of the pillar, and found to be $k_f = 19.6757$ N/m. As for the other parameters, $m = 7.07 \times 10^{-4}$ kg is the mass of each magnet and $L_0 = 0.01$ m is the initial spacing between two nodes in the lattice. Following the framework presented in the previous section, the band diagram of a repulsive lattice with an elastic foundation can be obtained by solving the following eigenvalue problem

$$\left[-\omega^2 \mathbf{M} + \mathbf{D}'(\mathbf{k}) \right] \phi = \mathbf{0} \quad (4.17)$$

where $\omega = 2\pi\nu$ is the angular frequency, \mathbf{k} is the wavevector, $\mathbf{M} = \begin{bmatrix} m & 0 \\ 0 & m \end{bmatrix}$ is the mass matrix and

$$\mathbf{D}'(\mathbf{k}) = \mathbf{D}(\mathbf{k}) + \mathbf{K}_f \quad (4.18)$$

is a wavevector-dependent stiffness matrix that already incorporates Bloch conditions. In Eq. 4.18, $\mathbf{D}(\mathbf{k})$ is the stiffness matrix of a triangular lattice, whose expression is given in Eq. 4.15, and $\mathbf{K}_f = \begin{bmatrix} k_f & 0 \\ 0 & k_f \end{bmatrix}$ represents the stiffness of the elastic foundation. The solution of Eq. 4.17 yields the band diagram plotted in Fig. 4.7(c). As expected, the band diagram is fully gapped at low frequencies as a result of the elastic foundation, and we observe the two canonical acoustic branches, the first is dominated by shear mechanisms and the second by longitudinal mechanisms.

To experimentally capture the linear response of the lattice, we employ the 3D laser vibrometer by which we measure the in-plane displacements of the individual magnets. Specifically, we measure the in-plane components of the velocity vector of each magnet in the interior of the lattice. The specimen is excited in the vertical

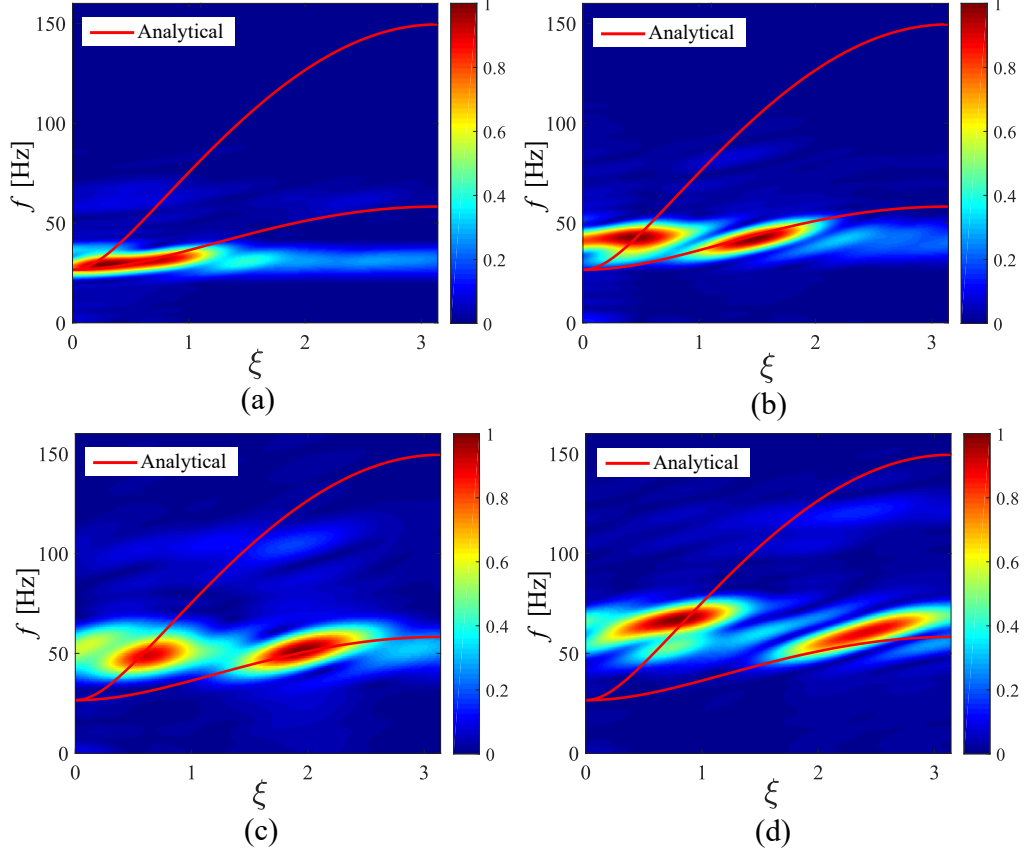


Figure 4.8: Experimental response spectra for tone-burst excitations at (a) 30 Hz, (b) 40 Hz, (c) 50 Hz, and (d) 60 Hz. The amplitude spectra conform to the band diagram predicted using the complete model, while they are not properly captured by the conventional one (especially for the shear mode).

direction by a force applied to the center magnet of the bottom layer (as indicated by the red dot in Fig. 4.9(a)). In Fig. 4.8, we plot the spectral response obtained via 2D-DFT of the experimental spatio-temporal data sampled along the green line (as shown in Fig. 4.7(a)) for tone-burst excitations with carrier frequencies centered at 30 Hz, 40 Hz, 50 Hz, and 60 Hz, respectively. For comparison, we superimpose the dispersion relations predicted using our modified analytical model (encompassing both \mathbf{D}_0 and \mathbf{D}^* contributions as per Eq. 4.18). In contrast with the previous cases, the band diagram is here fully gapped at low frequencies, which is a typical feature of systems with elastic

foundations. Notwithstanding small deviations at higher frequencies (which can be easily attributed to non-idealities and unavoidable minor differences between particle model and physical specimen, e.g., the neglecting of possible mild long-range interactions in the theoretical model), the experimental results show remarkable agreement with the dispersion branches obtained from the complete model.

4.3.2 Experimental characterization of nonlinear behavior

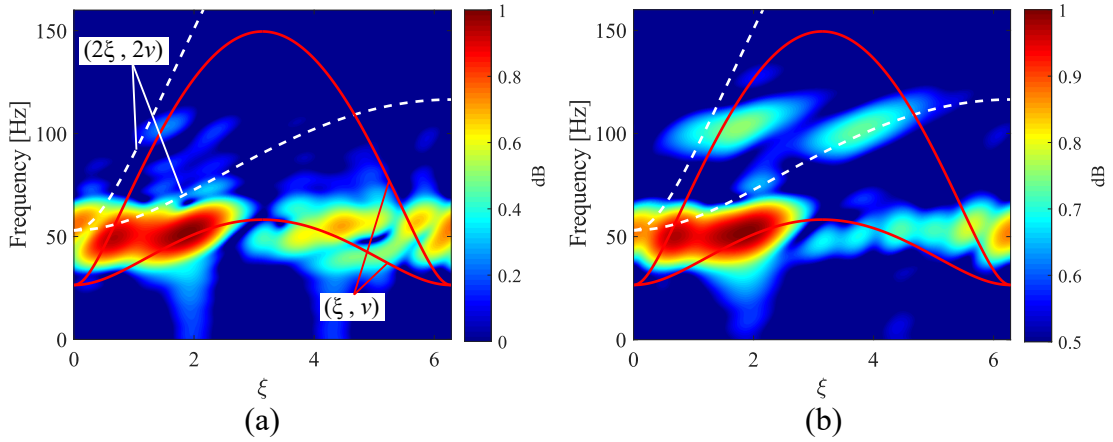


Figure 4.9: Spectra of the experimental responses for tone-burst excitations at 50 Hz. (a) Response to low-amplitude excitation, showing the fundamental harmonic activating both shear and longitudinal modes (red solid curves). (b) Response to high-amplitude excitation, showing two distinct signatures at the second harmonic (i.e., 100 Hz), confirming the existence of both homogeneous and forced components of the nonlinearly generated harmonic. The white dashed curves represent all the possible spectral points that can be activated by the forced component.

We now proceed to investigate the nonlinear response. In Fig. 4.9(a), we plot the color map of the normalized spectral amplitude obtained via 2D-DFT for a low-amplitude excitation at $\Omega_0 = 50$ Hz. With this reference excitation, we measure the amplitude of the vertical velocity at the excitation point to be equal to 0.03524 mm/s. Then, we progressively raise the amplitude of excitation, up to a level where the measured amplitude of the vertical velocity at the excitation point reaches 0.4004 mm/s, which is one order of magnitude larger than the reference case. The corresponding spectral amplitude map is given in Fig. 4.9(b). In both figures, we superimpose the

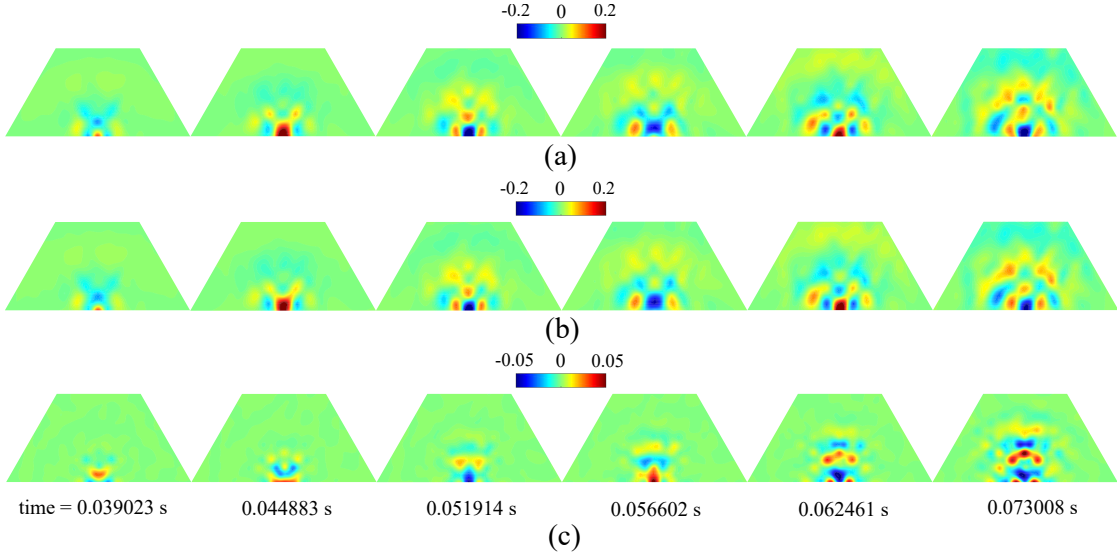


Figure 4.10: Snapshots of the wavefields experimentally acquired by laser scans at six successive time instants, showing distinct spatial patterns at the different harmonics. (a) Total wavefield. (b) Wavefield filtered at ν_0 , highlighting the fundamental harmonic. (c) Wavefield filtered at $2\nu_0$, highlighting the second harmonic. The two harmonics feature complementary modal and directional characteristics, thus exposing the functionality enrichment that is achieved by triggering a nonlinear response.

Γ -M portion of the linear dispersion branches (red curves) obtained via Bloch analysis informed using the equivalent lattice model and periodically extended into the second Brillouin zone for convenience. In addition, the white dashed curves denote the parametric locus of the $2\xi - 2\nu(\xi)$ pairs, i.e., the spectral points that feature simultaneously twice the frequency and twice the wavenumber of the acoustic phonons at the fundamental harmonic $(\xi, \nu(\xi))$. The $2\xi - 2\nu(\xi)$ points represent the pairs of frequency and wavenumber that can be displayed by the forced component of a nonlinearly generated second harmonic. Since these pairs do not live on any dispersion branch (and therefore do not conform to any mode of the linear system), their activation is conditional upon the generation of harmonics and is therefore the most robust detector of nonlinearity in the wave response. In other words, phonons that live on these curves must be generated through nonlinear mechanisms intrinsic to the lattice and cannot be merely induced by a component of the excitation with a 2ν frequency content, as such component would also necessarily result in the activation of the linear dispersion branch(es) available at

that frequency. This consideration provides a powerful tool to distinguish with absolute certainty the manifestation of nonlinearly generated harmonics from the signatures of high-frequency components that may be embedded by default in the excitation signal (for example due to nonlinearities in the signal generation and amplification). In essence, the ability to capture the forced response is the the most robust detector of nonlinearity in the lattice. As expected, in Fig. 4.9(a) we observe that the main spectral contribution is located at the prescribed frequency ($\nu_0 = 50$ Hz), where both the shear and longitudinal modes are activated, with no appreciable signature at the second harmonic ($2\nu_0 = 100$ Hz). In contrast, in the spectrum of the nonlinear response (i.e., Fig. 4.9(b)) we recognize two additional spectral signatures at the second harmonic. The one overlapping the longitudinal branch corresponds to the homogeneous component, while the one that lies precisely on the white curve is unequivocally identified as the forced component.

The spectral maps presented in Fig. 4.9 also provide insight in the different modal makeups of the fundamental and second harmonics. The fundamental harmonic blends both shear and longitudinal (S- and P-) modes, activated at comparable amplitude level (with an expected preference for the S-mode due to the higher compliance of the shear mechanisms), resulting in a hybrid polarization. At the second harmonic, the response also comprises two distinct contributions. The first, activated by the homogeneous component, involves the excitation of the P-mode in a higher-frequency and shorter-wavelength regime, and is therefore dominated by longitudinal characteristics. The second is the forced component, whose polarization is predominantly dictated by the shear characteristics of the fundamental harmonic that drives it, but does not conform to any linear modes per se. In essence, the response at the second harmonic also features a blend of distinct modal characteristics. The relative participation of these components in the response is, however, different and not exclusively controlled by the modal landscape at 2ν . We can characterize this result as an instance of modal enhancement, whereby the nonlinear activation of the second harmonic induces additional modal attributes to the response, perturbing the original modal makeup of the linear response.

The vibrometer scan also allows exploring the manifestation of SHG on the spatial pattern of the wave response. In Fig. 4.10, we plot six snapshots of the propagating wavefield using the vertical components of the measured velocities. In Fig. 4.10(a), we

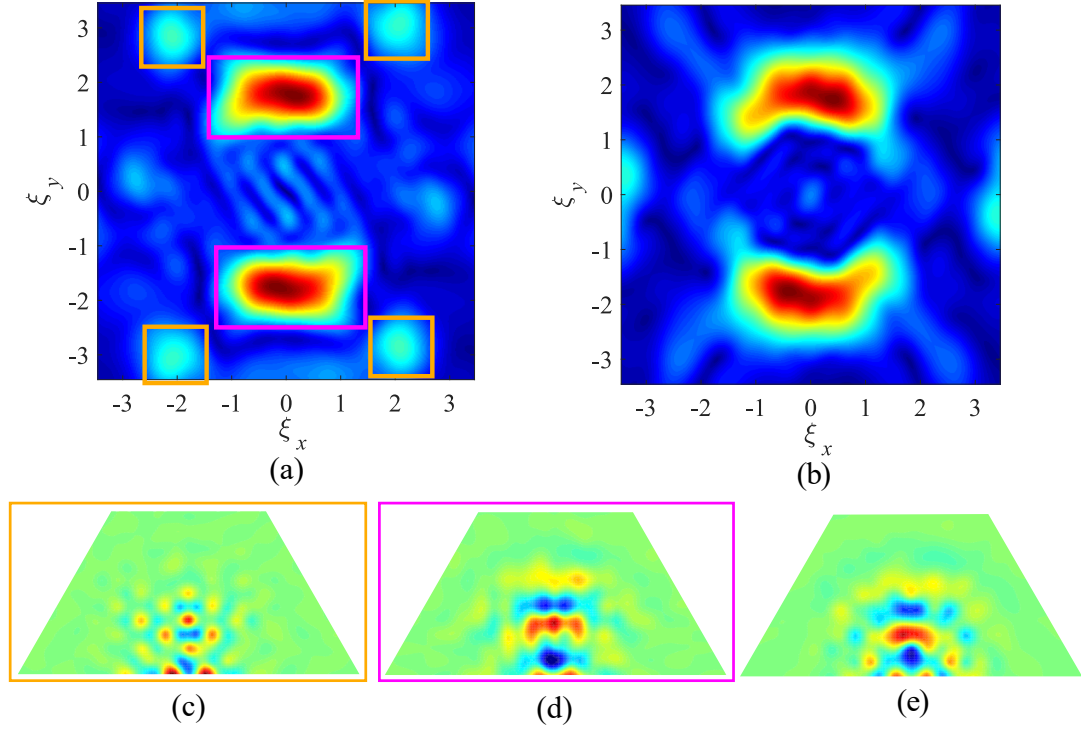


Figure 4.11: \mathbf{k} -plane amplitude spectra of (a) the filtered second harmonic of a nonlinear response and (b) a linear wavefield excited directly at $2\nu_0$. (c) and (d) Filtered wavefields of the spectral components inscribed in amber and magenta boxes, respectively.

show the total wavefield, encompassing fundamental and second harmonics, while in Fig. 4.10(b) and (c) we isolate the filtered components at ν_0 and $2\nu_0$, respectively. The wavefields reveal spatial complementarity between the predominantly vertical directivity of the second harmonic and the quasi-isotropic pattern of the fundamental harmonic. This result indicates that nonlinearity is responsible for a directivity enrichment. To highlight separately and filter the spatial contributions of the homogeneous and forced components that coexist at the second harmonic, we subject the last snapshot of the wavefield filtered at $2\nu_0$ (last snapshot in Fig. 4.10(c)) to 2D-DFT in space. The resulting \mathbf{k} -space spectrum is plotted in Fig. 4.11(a). For comparison, we repeat the exercise for a linear wavefield obtained with a low-amplitude excitation prescribed directly at $2\nu_0$ (Fig. 4.11(e)), whose spectrum is shown in Fig. 4.11(b). In Fig. 4.11(a), we identify two distinct spectral signatures at the second harmonic (appearing with their

mirror counterparts due to the symmetry of the wavefield and the symmetry folding operations involved in the 2D-DFT). The dominant component, inscribed by magenta boxes, is consistent with the spectrum of the linear wavefield excited directly at $2\nu_0$ (i.e., Fig. 4.11(b)), and is therefore interpreted as the homogeneous component. On the other hand, the secondary contribution, inscribed by amber boxes, which is germane to the nonlinear response, must be interpreted as the forced response. By zeroing out the two signatures, one at a time, and carrying out an inverse 2D-DFT of the remainder, we can filter out the separate wavefields of the two components, as shown in Fig. 4.11(c) and (d), respectively. Clearly, the pattern in the magenta box of Fig. 4.11(d), which exhibits longitudinal behavior, is reminiscent of the wavefield in Fig. 4.11(e), further supporting, from a spatial perspective, the notion that the homogeneous component conforms to the linear response that would be observed in the lattice if the excitation were prescribed directly at $2\nu_0$. The other, shown in Fig. 4.11(c) and corresponding to the forced component, displays a more dispersive spatial pattern. It is worth emphasizing again that, while it is possible that the homogeneous component may be in part triggered by nonlinearities extrinsic to the mechanical system and due, for instance, to harmonics buried in the excitation signal, the forced component is germane to the SHG established within the structure. Therefore, the existence of the forced second harmonic is the most powerful detector of mechanics-driven nonlinearities in the lattice.

4.4 Conclusions

In summary, we have predicted theoretically and demonstrated experimentally the complete dynamics of 2D interacting particle systems. First, we have demonstrated that the initial static repulsive forces play an important role in the linear dynamical behavior of these systems. Through an illustrative example of a resonating particle system, we have shown that the effect associated with the static forces is intrinsically tied to the 2D nature of the particle arrangements and disappears when the system reduces to a 1D configuration. Then, we have discussed the implications of this effect on the wave propagation characteristics of repulsive lattices, and we have highlighted the opportunities for mode-selective dispersion correction. Last, we have experimentally demonstrated these findings with a prototype lattice of magnets interacting repulsively and supported

by pillars.

Using the above findings as guidelines, we have characterized the nonlinear wave response of the prototype lattice. First, we have demonstrated the existence of SHG in the specimen, separately pinpointing its two second harmonic contributions. Then, we have shown that the nonlinear response features modal characteristics that are complementary to the those of the fundamental wave. Finally, we have reconstructed the spatial characteristics of the two nonlinear components, revealing additional complementarity between them in terms of spatial characteristics and directivity.

Chapter 5

Wavenumber-space band clipping in nonlinear periodic structures

The main nonlinear effect of cubic nonlinearity on wave propagation is an amplitude-dependent correction of the dispersion relation. This phenomenon manifests as a frequency shift of the dispersion relation when the excitation is prescribed as an initial condition, i.e., as an initial spatial profile imposed in the domain. Several models have been proposed to capture such frequency shifts. However, these models are not compatible with harmonic boundary excitations, which represent the conditions encountered in most practical applications, where the excitation is prescribed by imposing harmonic forces of displacements at selected points (often at a single point) in the interior of the domain or at its edges. To overcome this limitation, in this Chapter we present a multiple scales framework capable of analytically capturing the wavenumber shift experienced by dispersion relation of nonlinear periodic structures under harmonic boundary excitations. We also demonstrate that the wavenumber shifts result in an unusual dispersion correction effect that can be described as wavenumber-space band clipping.

5.1 Dispersion relation of nonlinear monatomic chains

In this section, we develop a multiple scales framework to properly capture the dispersion relation of a nonlinear monatomic spring-mass chain under both initial and

boundary excitations, and we investigate how different excitation conditions can significantly change the manifestation of cubic nonlinearity on the dispersive properties.

5.1.1 Multiple scales analysis

Consider an infinite monatomic chain in which adjacent masses are connected by springs featuring cubic nonlinearity. Under the assumption of weak nonlinearity, the restoring force in each spring can be expressed as

$$f = k\delta + \epsilon\Gamma\delta^3 \quad (5.1)$$

where δ denotes the relative displacement, ϵ is a small parameters, and k and Γ are the linear and cubic spring constants, respectively. The equation of motion for the n^{th} mass m can be derived as

$$m\ddot{u}_n + k(2u_n - u_{n-1} - u_{n+1}) + \epsilon\Gamma \left[(u_n - u_{n-1})^3 - (u_{n+1} - u_n)^3 \right] = 0 \quad (5.2)$$

where u_n represents the displacement of the n^{th} mass and the superscripted dot denotes time differentiation.

In the spirit of multiple scales analysis, we introduce a fast spatio-temporal variable $\theta_n = \xi n - \omega t$ (where ξ and ω are the normalized wavenumber and frequency, respectively) to capture the fundamental wave response, and two slow variables $s = \epsilon n$ (spatial), and $\tau = \epsilon t$ (temporal) to capture the weakly nonlinear effects (i.e., dispersion corrections). Accordingly, the solution is assumed to have an expansion of the form

$$u_n = u_n^0(\theta_n, s, \tau) + \epsilon u_n^1(\theta_n, s, \tau) + O(\epsilon^2) \quad (5.3)$$

Substituting Eq. 6.3 into Eq. 6.2, we obtain the equations at each order of expansion:

$$O(1): \quad \omega^2 m \frac{\partial^2 u_n^0}{\partial \theta_n^2} + k(2u_n^0 - u_{n-1}^0 - u_{n+1}^0) = 0 \quad (5.4)$$

$$O(\epsilon): \quad \omega^2 m \frac{\partial^2 u_n^1}{\partial \theta_n^2} + k(2u_n^1 - u_{n-1}^1 - u_{n+1}^1) = f \quad (5.5)$$

where the forcing function f at $O(\epsilon)$ is given as

$$f = 2\omega m \frac{\partial^2 u_n^0}{\partial \theta_n \partial \tau} + k \left(\frac{\partial u_{n+1}^0}{\partial s} - \frac{\partial u_{n-1}^0}{\partial s} \right) - \Gamma \left[(u_n^0 - u_{n-1}^0)^3 - (u_{n+1}^0 - u_n^0)^3 \right] \quad (5.6)$$

The general solution at $O(1)$ can be expressed as

$$u_n^0 = \frac{A(s, \tau)}{2} e^{i\theta_n} + \frac{A^*(s, \tau)}{2} e^{-i\theta_n} \quad (5.7)$$

where A is an arbitrary function of the slow variables (s, τ) , and $(\cdot)^*$ denotes the complex conjugate. Imposing Bloch conditions on the fast scale variable θ_n between neighboring atoms, we obtain

$$u_{n\pm 1}^0 = \frac{A(s, \tau)}{2} e^{i\theta_n} e^{\pm i\xi} + \frac{A^*(s, \tau)}{2} e^{-i\theta_n} e^{\mp i\xi} \quad (5.8)$$

Substituting Eq. 6.9 and Eq. 6.10 into Eq. 6.4, the linear dispersion relation is obtained

$$\omega = \sqrt{2k(1 - \cos(\xi))/m} \quad (5.9)$$

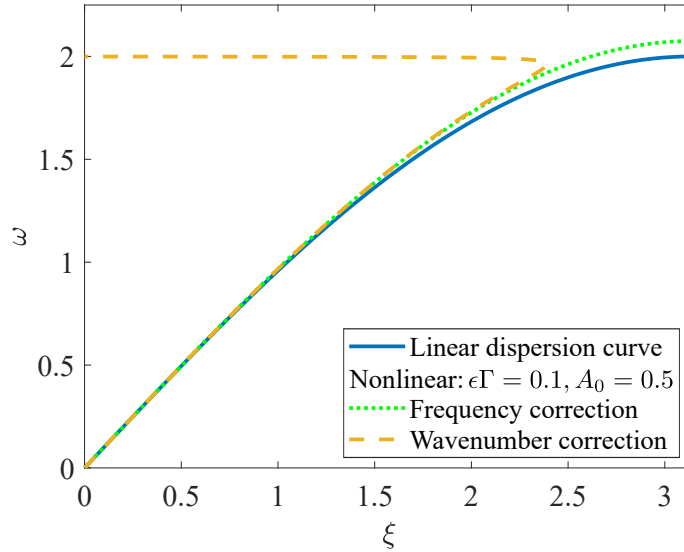


Figure 5.1: Corrected dispersion relation of a nonlinear monatomic chain based on standard multiple scales analysis (divergence occurs in the case of wavenumber correction).

We now shift our attention to the equation at $O(\epsilon_1)$, in which the forcing function f can be obtained by substituting Eq. 6.9 and Eq. 6.10 in Eq. 5.6. To prevent unbounded solution, the secular terms (i.e., the terms of the form $e^{\pm i\theta_n}$) appearing in f must be eliminated, leading to the following condition

$$\frac{\partial A}{\partial \tau} + \lambda \frac{\partial A}{\partial s} + i\mu |A|^2 A = 0 \quad (5.10)$$

where $\lambda = k \sin \xi / \omega m$ and $\mu = 6\Gamma \sin^4(\xi/2) / \omega m$. The solution of A can be written in a polar form as

$$A(s, \tau) = \alpha(s, \tau) e^{-i\beta(s, \tau)} \quad (5.11)$$

Substituting it into Eq. 5.10, yields a complex-variable algebraic equation, the solution of which requires that real and imaginary components vanish individually such that

$$\begin{aligned} \frac{\partial \alpha}{\partial \tau} + \lambda \frac{\partial \alpha}{\partial s} &= 0 \\ \frac{\partial \beta}{\partial \tau} + \lambda \frac{\partial \beta}{\partial s} &= \mu \alpha^2 \end{aligned} \quad (5.12)$$

The general solutions of these equations are

$$\begin{aligned} \alpha &= \alpha_0 (s - \lambda \tau) \\ \beta &= \beta_0 (s - \lambda \tau) + \beta^* \end{aligned} \quad (5.13)$$

The full expression for β encompasses a homogeneous solution β_0 and a particular solution β^* , the latter of which can be expressed either in terms of variable τ as $\beta^* = \mu \alpha^2 \tau$, or in terms of variable s as $\beta^* = \mu \alpha^2 s / \lambda$, depending on whether initial conditions or boundary conditions are considered. For example, given the initial harmonic amplitude profile $u_n = A_0 \cos \xi n$ at $t = 0$, it follows that $\alpha = A_0$, $\beta_0 = 0$ and $\beta^* = \mu \alpha^2 \tau$. Thus, the fundamental solution at $O(1)$ is

$$u_n^0 = \frac{A_0}{2} e^{i[\xi n - (\omega + \epsilon \mu A_0^2)t]} + c.c. \quad (5.14)$$

where *c.c.* denotes the complex conjugate of the preceding term. Eq. 5.14 shows that the nonlinear equation of motion (i.e., Eq. 6.2) produces a fundamental plane-wave solution, in which the frequency is modified by an amplitude-dependent correction term $\epsilon \mu A_0^2$. This cubic nonlinear effect is well documented in mathematics textbooks [80], as well as in literature of nonlinear periodic structures [79]. In contrast, if a boundary condition $u_n = A_0 \cos \omega t$ is imposed at one end of the chain (e.g., at $n = 0$), it follows that $\alpha = A_0$, $\beta_0 = 0$ and $\beta^* = \mu \alpha^2 s / \lambda$. With this, the fundamental solution becomes

$$u_n^0 = \frac{A_0}{2} e^{i[(\xi - \epsilon \mu A_0^2 / \lambda)n - \omega t]} + c.c. \quad (5.15)$$

in which the correction term $\epsilon \mu A_0^2 / \lambda$ takes place in the wavenumber domain.

Clearly, either frequency shifts or wavenumber shifts can modify the dispersive properties of the nonlinear monatomic chain. To demonstrate their tuning effects on the dispersion relation, we plot the modified dispersion relations predicted by Eq. 5.14 and Eq. 5.15, in comparison with the linear one, using the following parameters: $m = 1$, $k = \Gamma = 1$, $\epsilon = 0.1$, $A_0 = 0.5$ (standard SI units are adopted throughout the Chapter and omitted for simplicity). From a visual inspection, we observe that the two nonlinear dispersion branches start to deviate from the linear curve as ξ increases. While the two nonlinear curves overlap for a large range of frequencies, the one predicted by Eq. 5.15 diverges when ω is close enough to the cutoff frequency (2 rad/s). This divergence issue implies that the weakly nonlinear assumptions do not hold any more, and therefore the predictions of Eq. 5.15 are spurious.

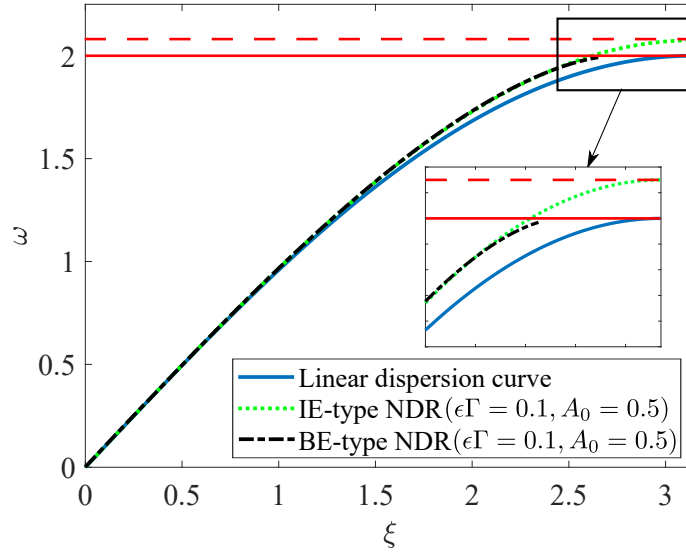


Figure 5.2: Corrected dispersion relation of a monatomic chain featuring hardening cubic nonlinearity obtained under different excitation conditions (a detailed comparison near the cutoff frequency is given in the inset).

To resolve this issue, we follow the approach proposed by [102], the basic notion of which is that the Bloch condition (Eq. 6.10), which imposes a constrain on the wavenumber between neighboring masses, needs to be updated once a wavenumber correction is determined from the perturbation analysis. Specifically, the original wavenumber ξ

should be replaced by the modified one $\xi - \epsilon\beta/s$ (this can be obtained by substituting Eq. 6.15 in Eq. 6.9 and collecting all the wavenumber contributions). This treatment results in a new condition (replacing Eq. 5.10) for the elimination of the secular terms at $O(\epsilon)$:

$$\frac{\partial A}{\partial \tau} + \lambda_0 \sin\left(\xi - \epsilon\frac{\beta}{s}\right) \frac{\partial A}{\partial s} + i\mu|A|^2 A = 0 \quad (5.16)$$

where $\lambda_0 = \frac{k}{\omega m}$. Substituting Eq. 6.15 in Eq. 6.14 yields the following equations for α and β

$$\begin{aligned} \frac{\partial \alpha}{\partial \tau} + \lambda_0 \sin\left(\xi - \epsilon\frac{\beta}{s}\right) \frac{\partial \alpha}{\partial s} &= 0 \\ \frac{\partial \beta}{\partial \tau} + \lambda_0 \sin\left(\xi - \epsilon\frac{\beta}{s}\right) \frac{\partial \beta}{\partial s} &= \mu\alpha^2 \end{aligned} \quad (5.17)$$

It can be shown that the above system of equations reduces to Eq. 5.12 to the first-order approximation for cases where the wavenumber correction $\epsilon\beta/s$ is at a higher order when compared to ξ . However, it is possible that, for some special cases, Eq. 6.16 gives profoundly different results from those solved by Eq. 5.12 as demonstrated below. Considering the same boundary excitation condition, it is reasonable to assume a priori, if a plane wave solution is allowed, that $\alpha = A_0$, $\beta_0 = 0$ and $\beta^* = Cs = \epsilon Cn$, where C is a real constant. Here, ϵC is the “true” wavenumber shift that we intend to determine. Substituting these into Eq. 6.16, yields the following transcendental equation for C

$$\lambda_0 C \sin \tilde{\xi} = \mu A_0^2 \quad (5.18)$$

where $\tilde{\xi} = \xi - \epsilon C$. While Eq. 6.17 is not amenable for analytical treatments, it is not difficult to find possible solutions numerically. Once C is determined, the fundamental solution can be expressed as

$$u_n^0 = \frac{A_0}{2} e^{i[(\xi - \epsilon C)n - \omega t]} + c.c \quad (5.19)$$

For the same parameters used above, in Fig. 5.2 we plot the corrected dispersion relation according to Eq. 5.19, and we also superimpose the linear dispersion curve and the nonlinear one predicted by Eq. 5.14, for comparison. We notice that the divergence observed in Fig. 5.1 for frequencies close to 2 rad/s is successfully resolved. The two nonlinear dispersion curves shown in Fig. 5.2 predict distinct dispersive characteristics

near the cutoff frequency. Specifically, the cubic nonlinear effect manifests as frequency shifts when initial excitations are imposed, leading to an extension of the dispersion relation in the frequency domain (green dotted curve). In contrast, wavenumber shifts are induced when boundary excitations are imposed. As a consequence, the dispersion relation is clipped in wavenumber space near the π limit (black dash-dotted curve). This wavenumber-space clipping effect is qualitatively consistent with observations recently reported by [107] invoking different modeling arguments. However, as shown in the inset of Fig. 5.2, the frequency range of the passing band is unaffected. For convenience, we will refer to the former nonlinear dispersion relation as IE-type NDR (IE standing for “initial excitation”) and to the latter one as BE-type NDR (BE standing for “boundary excitation”) throughout this Chapter.

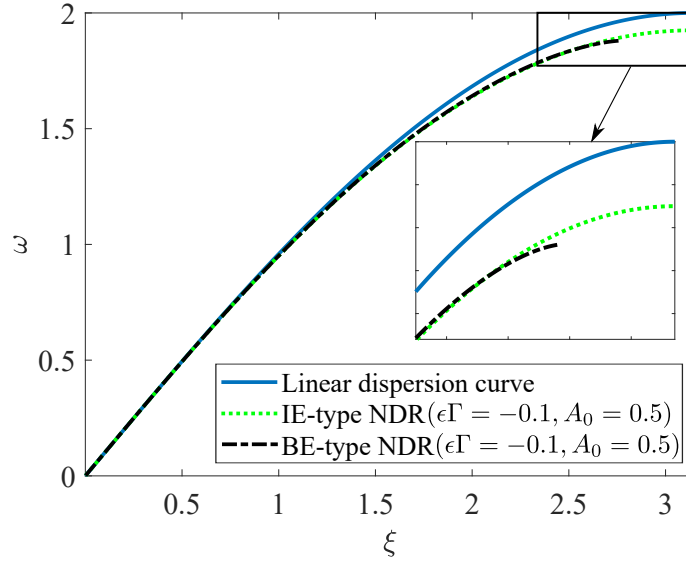


Figure 5.3: Corrected dispersion relation of a monatomic chain featuring softening cubic nonlinearity obtained under different excitation conditions (a detailed comparison near the cutoff frequency is given in the inset).

In the previous example, we investigated the dispersion characteristics of a monatomic chain featuring hardening cubic nonlinearity with $\Gamma = 1$. We now proceed to examine the case with softening cubic nonlinearity ($\Gamma = -1$). Following the same analysis, we can obtain the BE-type NDR of the chain with $\Gamma = -1$, which is plotted as a black

dashed curve in Fig. 5.3 and compared against the IE-type NDE counterpart (green dotted curve). Again, we observe the band clipping effect near the π limit. However, in contrast with the previous case, the cutoff frequency of the chain is modified using both nonlinear corrections. Compared to the IE-type NDR, the BE-type NDR further lowers the cutoff frequency for the same excitation amplitude, thus enabling a larger degree of nonlinear tuning.

5.1.2 Full-scale simulation

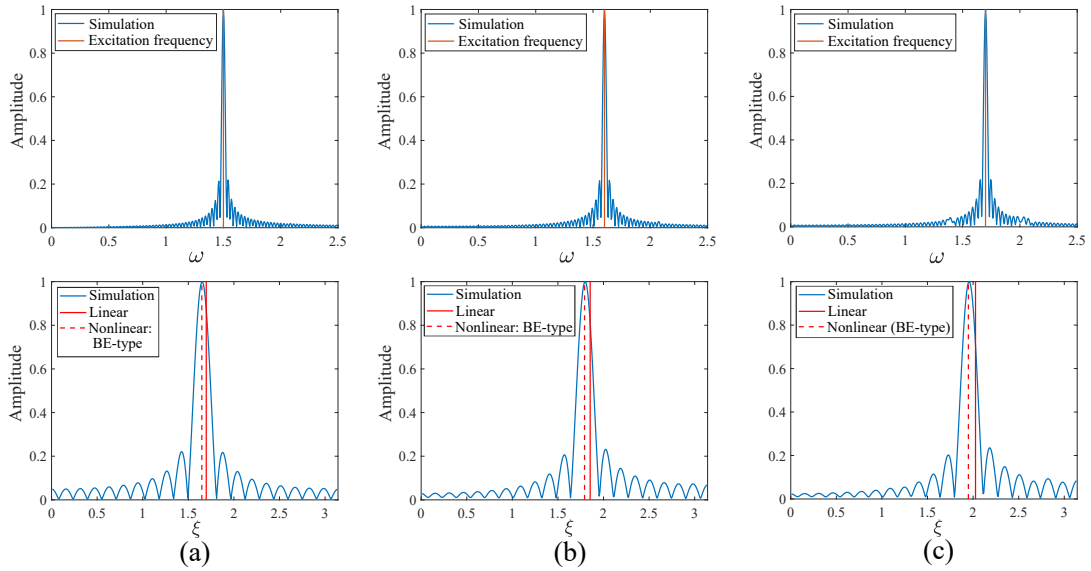


Figure 5.4: Spectra of the nonlinear response of a monatomic chain featuring hardening cubic nonlinearity ($\Gamma = 1$) under harmonic boundary excitations with three different frequencies: (a) 1.5 rad/s; (b) 1.6 rad/s; (c) 1.7 rad/s. First row: FFT of the output signal. Second row: FFT of the spatial profile after appropriately long simulation time.

To validate the above theoretical findings, we perform numerical simulations by integrating the equations of motion (Eq. 6.2) by means of the Verlet Algorithm [106]. We study the wave response of a monatomic chain with hardening cubic nonlinearity (with $\Gamma = 1$), consisting of 40 masses, and subjected to a harmonic boundary excitation imposed at the first mass. To minimize reflections and establish plane waves, an absorbing layer of 30 masses is attached at the end of the monatomic chain. The coefficient profile

for the n^{th} mass in the absorbing layer is given by

$$C_n = C_0 \left(\frac{n}{N_{\text{PML}}} \right)^\gamma \quad (5.20)$$

where $C_0 = 3$ is the maximum damping coefficient, $N_{\text{PML}} = 30$ denotes the number of unit cells in the layer, γ is set to 3 in the simulation. In Fig. 5.4, we plot the FFT of the time history of the last mass (i.e., the output of the chain) and the FFT of the spatial profile (after nearly plane wave response is reached) for three prescribed frequencies (denoted by the red bars): 1.5 rad/s, 1.6 rad/s, and 1.7 rad/s. We observe that the excitation frequencies are preserved in the output time histories while wavenumber shifts are observed in the nonlinear spatial profiles, matching the prediction from Eq. 5.19 (red dashed bars) and confirming the statement that, for harmonic boundary excitations, cubic nonlinear effect manifests as wavenumber shifts, as opposed to frequency shifts. For completeness, we repeat the simulation for a chain with softening cubic nonlinearity ($\Gamma = -1$) at one excitation frequency (1.8 rad/s), and the corresponding result is given in Fig. 5.5. It can be seen that the simulation result reveals a right-shifted wavenumber, which is in excellent agreement with the theoretical predication (red dashed bar). As an interesting side observation, we notice that the numerical simulation could diverge from the analytical model and multi-frequency quasi-periodic response would emerge if the harmonic excitation is set sufficiently close to the cutoff frequency and beyond certain amplitude thresholds (similar phenomena are reported by [64]).

The next task is to verify that the BE-type NDR preserves the cutoff frequency of the linear case. A characteristic that makes it distinct from the IE-type NDR for cases with hardening cubic nonlinearity. To this end, we set the excitation frequency to 2.05 rad/s, which is above the linear cutoff frequency (2 rad/s) but below that of the IE-type NDR (2.075 rad/s). The corresponding nonlinear response is shown in Fig. 5.6, in which we plot the input and output as functions of time in Fig. 5.6(a), as well as the spatial profile in Fig. 5.6(b). From a visual inspection, we observe a low output-input ratio and a clear spatial attenuation, which indicate the establishment of bandgap conditions further confirming the validity of the BE-type NDR obtained from the analytical model.

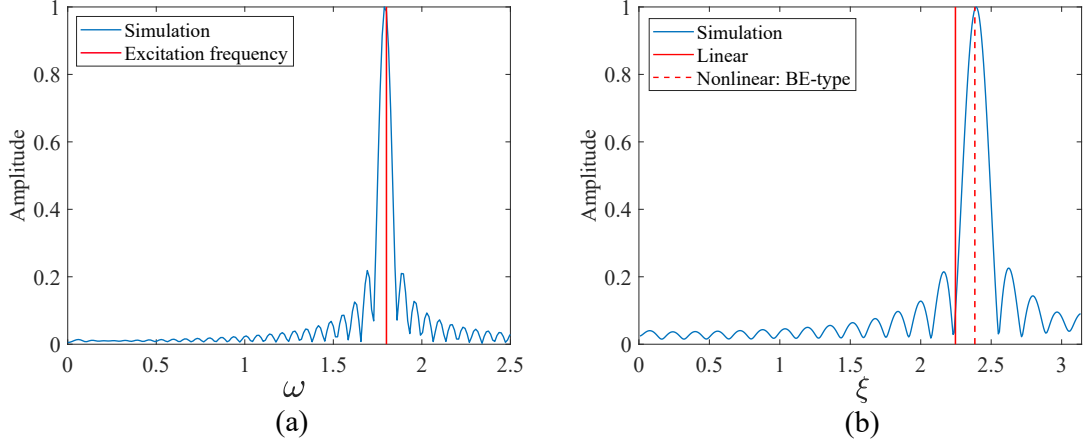


Figure 5.5: Spectra of the nonlinear response of a monatomic chain featuring softening cubic nonlinearity ($\Gamma = -1$) under harmonic boundary excitations at 1.8 rad/s. (a) FFT of the output signal. (b) FFT of the spatial profile after appropriately long simulation time.

5.2 Bandgap tunability in nonlinear locally-resonant periodic structures

Metamaterials featuring internal resonators are of great interest for their ability to open locally-resonant bandgap at low frequencies [2], as well as their implications for wave manipulation, including negative refraction [13], subwavelength wave steering [9], and seismic shielding [10]. In this section, we extend the multiple scales framework to nonlinear locally-resonant periodic structures to explore the availability of bandgap tunability under the practical constrain of boundary excitations.

5.2.1 Multiple scales analysis

Consider a periodic structure featuring internal resonators, which can be conceptually modeled as a mass-in-mass chain (as depicted in Fig. 5.7). Cubic nonlinearity can be incorporated either in the springs connecting the neighboring masses of the main chain (configuration referred to as system A), or in the internal springs attached to the internal resonators (system B). To obtain the BE-type NDR of the two systems, we extend the multiple scales analysis of the monatomic chain to the two-degree-of-freedom problem

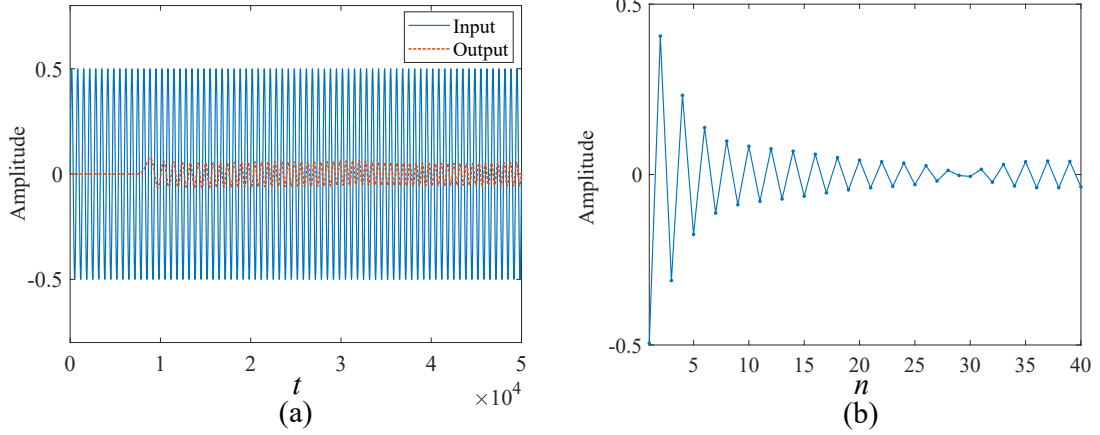


Figure 5.6: Nonlinear response of a monatomic chain under harmonic boundary excitation at frequency 2.05 rad/s, lying above the cutoff of the linear system but below that of the branch endowed with frequency correction. (a) Input signal vs. output signal. (b) Spatial profile after appropriately long simulation time. Both data sets suggest attenuation compatible with bandgap conditions, confirming that a frequency shift of the dispersion branch is not observed for boundary excitations.

of the mass-in-mass chain.

The equations of motion for the two nonlinear mass-in-mass systems can be written in the matrix form as

$$\begin{aligned}
 \begin{bmatrix} m_1 & 0 \\ 0 & m_2 \end{bmatrix} \begin{Bmatrix} \ddot{u}_n \\ \ddot{v}_n \end{Bmatrix} + \begin{bmatrix} 2k_1 + k_2 & -k_2 \\ -k_2 & k_2 \end{bmatrix} \begin{Bmatrix} u_n \\ v_n \end{Bmatrix} + \begin{bmatrix} -k_1 & 0 \\ 0 & 0 \end{bmatrix} \begin{Bmatrix} u_{n-1} \\ v_{n-1} \end{Bmatrix} + \\
 \begin{bmatrix} -k_1 & 0 \\ 0 & 0 \end{bmatrix} \begin{Bmatrix} u_{n+1} \\ v_{n+1} \end{Bmatrix} + \mathbf{f}_{NL}^{A(B)} = \begin{Bmatrix} 0 \\ 0 \end{Bmatrix} \quad (5.21)
 \end{aligned}$$

in which u_n and v_n denote the displacements of m_1 and m_2 in the n th unit cell, respectively; $\mathbf{f}_{NL}^A = \epsilon\Gamma \begin{Bmatrix} (u_n - u_{n-1})^3 - (u_{n+1} - u_n)^3 \\ 0 \end{Bmatrix}$ for system A;

and $\mathbf{f}_{NL}^B = \epsilon\Gamma \begin{Bmatrix} (u_n - v_n)^3 \\ -(u_n - v_n)^3 \end{Bmatrix}$ for system B.

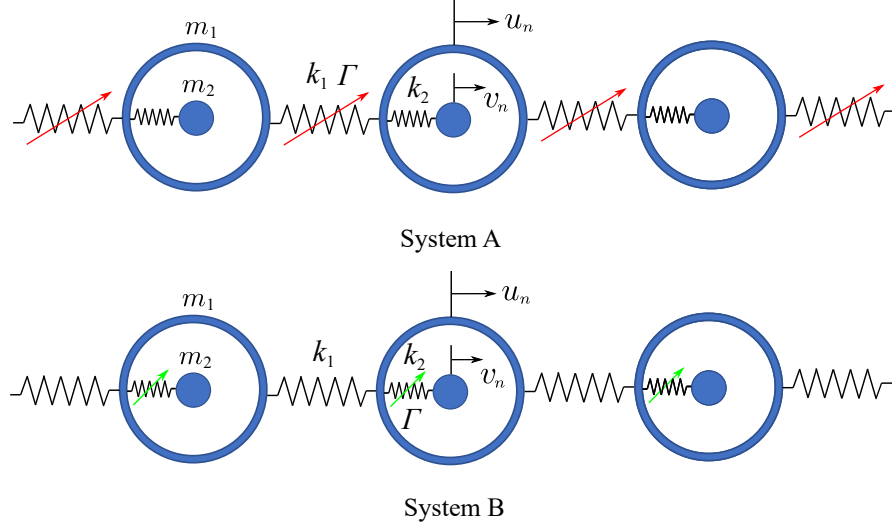


Figure 5.7: Schematic of nonlinear mass-in-mass chains. System A: a mass-in-mass chain with nonlinear springs connecting the masses m_1 . System B: a mass-in-mass chain with nonlinear springs attached to the local resonators m_2 .

The nodal displacements can be expressed up to the first-order approximation as

$$\mathbf{u}_n = \begin{Bmatrix} u_n(t) \\ v_n(t) \end{Bmatrix} = \begin{Bmatrix} u_n^0(\theta_n, s, \tau) + \epsilon u_n^1(\theta_n, s, \tau) \\ v_n^0(\theta_n, s, \tau) + \epsilon v_n^1(\theta_n, s, \tau) \end{Bmatrix} \quad (5.22)$$

By substituting Eq. 5.22 into Eq. 5.21, we obtain the following system of cascading equations

$$O(1): \quad \omega^2 \mathbf{M} \frac{\partial^2 \mathbf{u}_n^0}{\partial \theta_n^2} + \mathbf{K}_1 \mathbf{u}_n + \mathbf{K}_2 \mathbf{u}_{n-1}^0 + \mathbf{K}_2 \mathbf{u}_{n+1}^0 = \mathbf{0} \quad (5.23)$$

$$O(\epsilon): \quad \omega^2 \mathbf{M} \frac{\partial^2 \mathbf{u}_n^1}{\partial \theta_n^2} + \mathbf{K}_1 \mathbf{u}_n^1 + \mathbf{K}_2 \mathbf{u}_{n-1}^1 + \mathbf{K}_2 \mathbf{u}_{n+1}^1 = \mathbf{F}^{A(B)} \quad (5.24)$$

where $\mathbf{M} = \begin{bmatrix} m_1 & 0 \\ 0 & m_2 \end{bmatrix}$ is the mass matrix; $\mathbf{K}_1 = \begin{bmatrix} 2k_1 + k_2 & -k_2 \\ -k_2 & k_2 \end{bmatrix}$; $\mathbf{K}_2 = \begin{bmatrix} -k_1 & 0 \\ 0 & 0 \end{bmatrix}$

and the forcing term at $O(\epsilon)$ is

$$\mathbf{F}^{A(B)} = 2\omega \mathbf{M} \frac{\partial^2 \mathbf{u}_n^0}{\partial \theta_n \partial \tau} - \mathbf{q}^{A(B)} + \begin{Bmatrix} k_1 \left(\frac{\partial u_{n+1}^0}{\partial s} - \frac{\partial u_{n-1}^0}{\partial s} \right) \\ 0 \end{Bmatrix} \quad (5.25)$$

in which $\mathbf{q}^A = \Gamma \begin{Bmatrix} (u_n^0 - u_{n-1}^0)^3 - (u_{n+1}^0 - u_n^0)^3 \\ 0 \end{Bmatrix}$ for system A;

and $\mathbf{q}^B = \Gamma \begin{Bmatrix} (u_n^0 - v_n^0)^3 \\ -(u_n^0 - v_n^0)^3 \end{Bmatrix}$ for system B.

A plane wave solution at $O(1)$ can be assumed to have the form

$$\mathbf{u}_n^0 = \frac{A(s, \tau)}{2} \boldsymbol{\phi} e^{i\theta_n} + \frac{A^*(s, \tau)}{2} \boldsymbol{\phi}^* e^{-i\theta_n} \quad (5.26)$$

where $\boldsymbol{\phi} = \begin{Bmatrix} \phi_u \\ \phi_v \end{Bmatrix}$ is a modal eigenvector. Accordingly, the Bloch condition (Eq. 6.10) becomes

$$\mathbf{u}_{n\pm 1} = \frac{A(s, \tau)}{2} \boldsymbol{\phi} e^{i\theta_n} e^{\pm i\xi} + \frac{A^*(s, \tau)}{2} \boldsymbol{\phi}^* e^{-i\theta_n} e^{\mp i\xi} \quad (5.27)$$

Substituting Eq. 5.26 and Eq. 5.27 into Eq. 5.23 yields the following eigenvalue problem

$$\left(-\omega^2 \mathbf{M} + \mathbf{K}(\xi) \right) \boldsymbol{\phi} = \mathbf{0} \quad (5.28)$$

where $\mathbf{K}(\xi) = \begin{bmatrix} 2k_1(1 - \cos \xi) + k_2 & -k_2 \\ -k_2 & k_2 \end{bmatrix}$. The linear dispersion relation of a mass-in-mass chain can be obtained by solving the above eigenvalue problem, which can be analytically expressed as

$$\omega_{1,2} = \sqrt{\frac{b \mp \Delta(\xi)}{2a}} \quad (5.29)$$

where $\Delta(\xi) = \sqrt{b^2 - 4ac}$, with $a = m_1 m_2$, $b = (m_1 + m_2) k_2 + 2m_2 k_1 (1 - \cos \xi)$, and $c = 2k_1 k_2 (1 - \cos \xi)$, and ω_1 and ω_2 denote the acoustic and optical branch, respectively. The corresponding normalized eigenvector is given by

$$\boldsymbol{\phi}_{1,2} = \begin{Bmatrix} -\omega_{1,2}^2 m_2 + k_2 \\ k_2 \end{Bmatrix} / \sqrt{\omega_{1,2}^4 m_2^2 - 2k_2 m_2 \omega_{1,2}^2 + 2k_2^2} \quad (5.30)$$

We now follow the same logic described in the section 1.1 to derive an equation for the elimination of the secular terms at $O(\epsilon)$. For multi-degree-of-freedom systems, we can write the solution \mathbf{u}_n^1 as a superposition of the normal modes: $\mathbf{u}_n^1 = \boldsymbol{\Phi} \mathbf{z}_n$, where $\boldsymbol{\Phi}$ is the modal matrix featuring the modal vectors $\boldsymbol{\phi}$ as columns [108, 83]. Premultiply

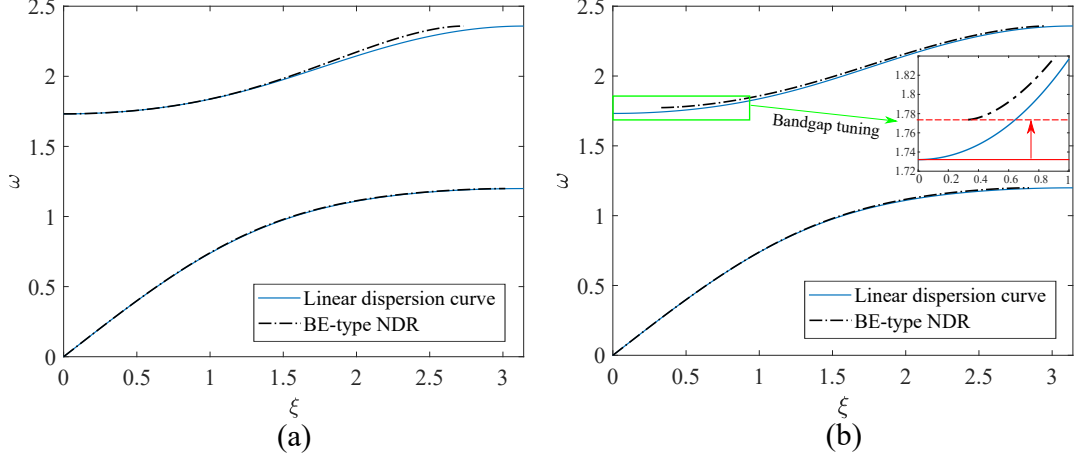


Figure 5.8: Corrected dispersion relations of (a) system A with nonlinearity in the main chain and (b) system B with nonlinearity in the local resonators. The band clipping effect gives rise to a bandgap tuning functionality in system B, which is not available in system A.

Eq. 5.24 by ϕ^H , where $(\cdot)^H$ denotes conjugate transpose, and note that its linear kernel is the same as the linear kernel of Eq. 5.24, leading to

$$\omega^2 \bar{m} \frac{\partial^2 z_n}{\partial \theta_n^2} + \bar{k} z_n = \phi^H \mathbf{F}^{A(B)} \quad (5.31)$$

where $\bar{m} = \phi^H \mathbf{M} \phi$ and $\bar{k} = \phi^H \mathbf{K} \phi$ are the modal mass and stiffness. The elimination of the secular terms in the RHS of Eq. 5.31 leads to the required condition using the updated wavenumber $\xi - \epsilon \frac{\beta}{s}$

$$\frac{\partial A}{\partial \tau} + \lambda_0 \sin \left(\xi - \epsilon \frac{\beta}{s} \right) \frac{\partial A}{\partial s} + i \mu^{A(B)} |A|^2 A = 0 \quad (5.32)$$

where $\lambda_0 = \frac{k_1 |\phi_u|^2}{\omega \bar{m}}$, $\mu^A = 6\Gamma \phi_u^4 \sin^4(\xi/2) / \omega \bar{m}$ for system A, and $\mu^B = 3\Gamma(\phi_u - \phi_v)(\phi_u^3 - \phi_v^3 + \phi_u \phi_v^2 - \phi_u^2 \phi_v) / 8\omega \bar{m}$ for system B. Repeating the procedure that leads to Eq. 6.17, we derive a similar transcendental equation, from which the wavenumber shift can be determined numerically. Then, we can easily construct the BE-type NDR of the two nonlinear systems. For a set of parameters selected as $m_1 = 1$, $m_2 = 0.5$, $k_1 = k_2 = \Gamma = 1$, $\epsilon = 0.1$, and $A_0 = 0.5$, we plot in Fig. 5.8 the BE-type NDR of system A in comparison with that of system B, and we superimpose their linear dispersion relations

for reference. As expected, in the BE-type NDR of system A, we observe band clipping similar to that observed in the monatomic chain with a wavenumber shift that increases as ξ approaches π and no influence on the bandgap bounds. Interestingly, for system B, in addition to the π limit, clipping also appears at the origin of the optical branch. As a result, the branch effectively starts at a finite wavenumber and the shift is accompanied by an upward shift of the cut-on frequency, resulting in a bandgap extension. This dispersive characteristic uniquely germane to system B endows it with a bandgap tuning functionality that is unachievable in system A where the nonlinearity is implemented in the main chain.

5.2.2 Full-scale simulation

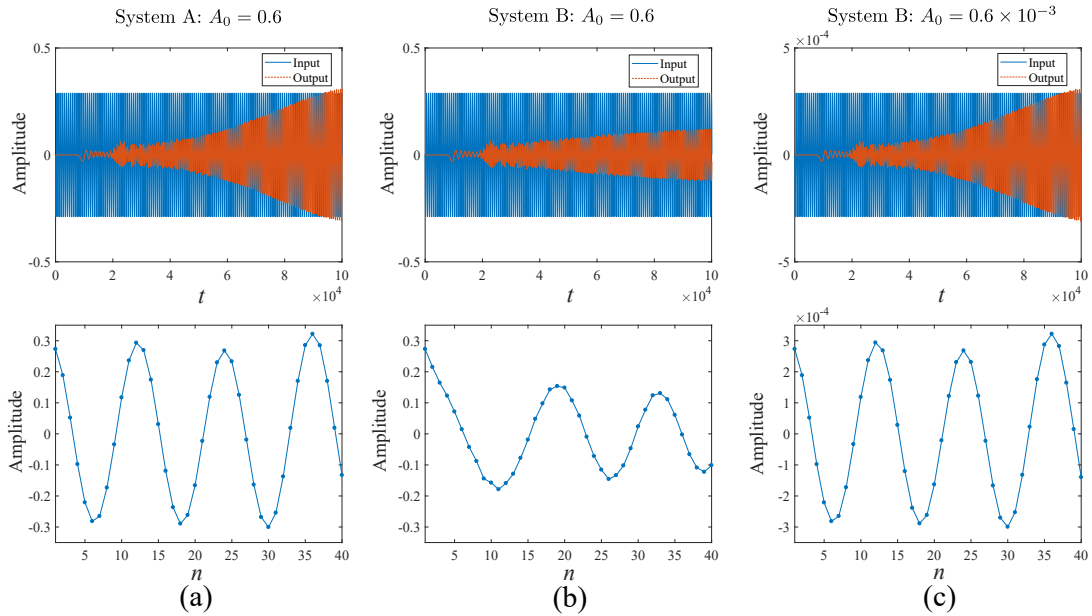


Figure 5.9: Temporal and spatial response of (a) system A and (b) system B for high amplitude of excitation $A_0 = 0.6$, and (c) system B for low amplitude $A_0 = 0.6 \times 10^{-3}$, under harmonic boundary excitation at frequency 1.76 rad/s. First row: Input signal vs output signal. Second row: Spatial profile after appropriately long simulation time, indicating that attenuation is activated only for system B under high amplitude of excitation.

We perform a suite of numerical simulations to demonstrate the bandgap tuning

capability of system B and the lack thereof of system A. The excitation frequency is set at 1.76 rad/s, which is located in the range of the bandgap extension shown in the inset of Fig. 5.8(b). First, in Fig. 5.9(a) and (b), we plot the temporal and spatial response of system A and B, respectively, for the same high-amplitude excitation ($A_0 = 0.6$). It is clear that the wave response of system B is highly attenuated compared to that of system A, confirming the existence of bandgap conditions at the prescribed frequency in system B, in accordance with the bandgap extension. Next, in Fig. 5.9(c) we plot the response of system B for a low-amplitude excitation ($A_0 = 0.6 \times 10^{-3}$). We observe that the attenuation effect is switched off, which further demonstrates that the bandgap of system B can be activated by controlling of the excitation amplitude.

5.3 Conclusions

In this Chapter, we have presented a general framework based on multiple scales analysis to properly capture the dispersive properties of weakly nonlinear periodic structures. Through this framework, we have revisited the benchmark problem of a cubic nonlinear monatomic chain, demonstrating that the cubic nonlinearity manifests as wavenumber shifts under harmonic boundary excitations in contrast to the typical frequency shifts observed when harmonic initial excitations are prescribed. Moreover, we have shown that wavenumber shifts have a strong influence on the dispersion relation, resulting in wavenumber-space band clipping. Then, we have extended the framework to nonlinear locally-resonant periodic structures to explore the bandgap tuning potential resulting from the band clipping effect. We have determined that bandgap tunability is available in systems where the cubic nonlinearity is introduced in the internal springs supporting the resonators, while no such effect arises in the presence of cubic nonlinearity in the main chain.

Chapter 6

Doubly-nonlinear waveguides with self-switching functionality selection capabilities

In the above Chapters, we have demonstrated the main effects of quadratic and cubic nonlinearity on wave propagation separately. Here, we intend to explore the possible interplay of quadratic and cubic nonlinearity and its implications for the design of adaptive acoustic switches, if the two types of nonlinearity coexist in a periodic structure.

6.1 Multiple scales analysis

6.1.1 Governing equations and linear dispersion relation

Our reference system is the spring-mass chain with a locally-resonant nonlinear foundation shown in Fig. 6.1. In each cell, the primary mass m_1 is connected to an auxiliary mass m_2 through linear spring 1, and m_2 is connected to a fixed point via spring 2, which is assumed to feature cubic nonlinearity, thus implementing a locally-resonant nonlinear foundation. Spring 3, connecting m_1 to its neighbors along the chain, is assumed to feature quadratic nonlinearity. Under weak nonlinearity assumptions, the force-stretch

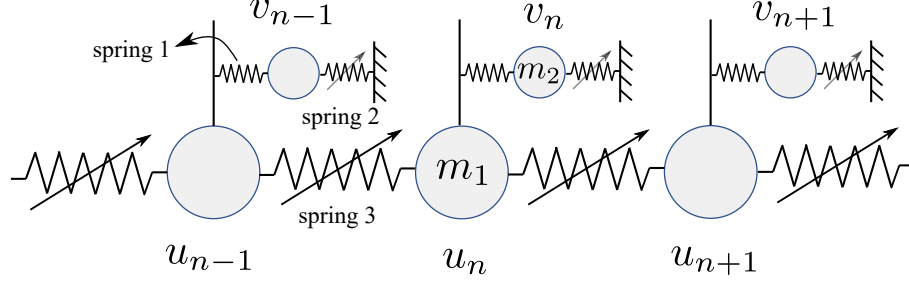


Figure 6.1: Nonlinear spring-mass chain with locally-resonant nonlinear elastic foundation.

relations in the three springs can be expressed as:

$$\begin{aligned}
 f_1 &= J_2 \delta \\
 f_2 &= G_2 \delta + \epsilon_1 G_4 \delta^3 \\
 f_3 &= K_2 \delta + \epsilon_2 K_3 \delta^2
 \end{aligned} \tag{6.1}$$

where ϵ_1 and ϵ_2 are small parameters for the cubic and quadratic nonlinearities, respectively. In this analysis, we take all the material parameters (i.e., J_2 , G_2 , K_2 , K_3 , and G_4) to be at the same order, e.g., $O(1)$, while ϵ_1 and ϵ_2 are small quantities of order greater than $O(1)$ which control the relative smallness of the different terms. Here, specifically, we assume that $\epsilon_1 > \epsilon_2$, in order to establish the hierarchy between nonlinear terms that is necessary to achieve the desired tuning effects.

The equations of motion for the two masses (m_1 and m_2) in n^{th} unit cell can be written in matrix form as:

$$\begin{aligned}
 &\begin{bmatrix} m_1 & 0 \\ 0 & m_2 \end{bmatrix} \begin{Bmatrix} \ddot{u}_n \\ \ddot{v}_n \end{Bmatrix} + \begin{bmatrix} 2K_2 + J_2 & -J_2 \\ -J_2 & J_2 + G_2 \end{bmatrix} \begin{Bmatrix} u_n \\ v_n \end{Bmatrix} + \begin{bmatrix} -K_2 & 0 \\ 0 & 0 \end{bmatrix} \begin{Bmatrix} u_{n-1} \\ v_{n-1} \end{Bmatrix} + \\
 &\begin{bmatrix} -K_2 & 0 \\ 0 & 0 \end{bmatrix} \begin{Bmatrix} u_{n+1} \\ v_{n+1} \end{Bmatrix} + \epsilon_1 \begin{Bmatrix} 0 \\ G_4 v_n^3 \end{Bmatrix} + \epsilon_2 \begin{Bmatrix} K_3 [(u_n - u_{n-1})^2 - (u_{n+1} - u_n)^2] \\ 0 \end{Bmatrix} = \begin{Bmatrix} 0 \\ 0 \end{Bmatrix}
 \end{aligned} \tag{6.2}$$

In the spirit of multiple scales analysis, we introduce a fast spatio-temporal variable $\theta_n = \xi n - \omega t$, where ξ and ω are the normalized wavenumber and frequency, respectively, and n is an integer mass index, as well as the two slow variables $s = \epsilon_1 n$ (spatial), and

$\tau = \epsilon_1 t$ (temporal). Accordingly, the cell nodal response is expressed as an expansion, up to $O(\epsilon_2)$, in successive approximations as:

$$\mathbf{u}_n = \begin{Bmatrix} u_n(t) \\ v_n(t) \end{Bmatrix} = \begin{Bmatrix} u_n^0(\theta_n, s, \tau) + \epsilon_1 u_n^1(\theta_n, s, \tau) + \epsilon_2 u_n^2(\theta_n, s, \tau) \\ v_n^0(\theta_n, s, \tau) + \epsilon_1 v_n^1(\theta_n, s, \tau) + \epsilon_2 v_n^2(\theta_n, s, \tau) \end{Bmatrix} \quad (6.3)$$

Substituting this into Eq. 6.2 and using the chain rule to resolve the time derivatives, one obtains the following system of cascading linear equations at each order of expansion:

$$O(1): \quad \omega^2 \mathbf{M} \frac{\partial^2 \mathbf{u}_n^0}{\partial \theta_n^2} + \mathbf{K}_1 \mathbf{u}_n + \mathbf{K}_2 \mathbf{u}_{n-1}^0 + \mathbf{K}_2 \mathbf{u}_{n+1}^0 = \mathbf{0} \quad (6.4)$$

$$O(\epsilon_1): \quad \omega^2 \mathbf{M} \frac{\partial^2 \mathbf{u}_n^1}{\partial \theta_n^2} + \mathbf{K}_1 \mathbf{u}_n^1 + \mathbf{K}_2 \mathbf{u}_{n-1}^1 + \mathbf{K}_2 \mathbf{u}_{n+1}^1 = \mathbf{f}^1 \quad (6.5)$$

$$O(\epsilon_2): \quad \omega^2 \mathbf{M} \frac{\partial^2 \mathbf{u}_n^2}{\partial \theta_n^2} + \mathbf{K}_1 \mathbf{u}_n^2 + \mathbf{K}_2 \mathbf{u}_{n-1}^2 + \mathbf{K}_2 \mathbf{u}_{n+1}^2 = \mathbf{f}^2 \quad (6.6)$$

where $\mathbf{M} = \begin{bmatrix} m_1 & 0 \\ 0 & m_2 \end{bmatrix}$; $\mathbf{K}_1 = \begin{bmatrix} 2K_2 + J_2 & -J_2 \\ -J_2 & J_2 + G_2 \end{bmatrix}$; $\mathbf{K}_2 = \begin{bmatrix} -K_2 & 0 \\ 0 & 0 \end{bmatrix}$ and the forcing terms at $O(\epsilon_1)$ and $O(\epsilon_2)$ are:

$$\mathbf{f}^1 = 2\omega \mathbf{M} \frac{\partial^2 \mathbf{u}_n^0}{\partial \theta_n \partial \tau} - \begin{Bmatrix} 0 \\ G_4 (v_n^0)^3 \end{Bmatrix} + \begin{Bmatrix} K_2 \left(\frac{\partial u_{n+1}^0}{\partial s} - \frac{\partial u_{n-1}^0}{\partial s} \right) \\ 0 \end{Bmatrix} \quad (6.7)$$

$$\mathbf{f}^2 = - \begin{Bmatrix} K_3 \left[(u_n^0 - u_{n-1}^0)^2 - (u_{n+1}^0 - u_n^0)^2 \right] \\ 0 \end{Bmatrix} \quad (6.8)$$

The general solution at $O(1)$ can be expressed as

$$\mathbf{u}_n^0 = A(s, \tau) \boldsymbol{\phi} e^{i\theta_n} + A^*(s, \tau) \boldsymbol{\phi}^* e^{-i\theta_n} \quad (6.9)$$

where A is an amplitude term that only depends on the slow scale variables (s, τ) , $\boldsymbol{\phi} = \begin{Bmatrix} \phi_u \\ \phi_v \end{Bmatrix}$ is a modal vector, and $(\cdot)^*$ denotes the complex conjugate of a variable. Imposing Bloch conditions on the fast scale variable θ_n between neighboring cells, we obtain

$$\mathbf{u}_{n\pm 1} = A(s, \tau) \boldsymbol{\phi} e^{i\theta_n} e^{\pm i\xi} + A^*(s, \tau) \boldsymbol{\phi}^* e^{-i\theta_n} e^{\mp i\xi} \quad (6.10)$$

Substituting Eq. 6.9 and Eq. 6.10 into Eq. 6.4, the linear dispersion relation is obtained by solving the eigenvalue problem

$$\left(-\omega^2 \mathbf{M} + \mathbf{K}(\xi)\right) \phi = \mathbf{0} \quad (6.11)$$

where $\mathbf{K}(\xi) = \begin{bmatrix} 2K_2(1 - \cos \xi) + J_2 & -J_2 \\ -J_2 & J_2 + G_2 \end{bmatrix}$. Two branches, denoted as “L” for the lower branch and “U” for the upper branch, are obtained analytically as:

$$\omega_{L/U} = \sqrt{\frac{b \mp \Delta(\xi)}{2a}} \quad (6.12)$$

where $\Delta(\xi) = \sqrt{b^2 - 4ac}$, with $a = m_1 m_2$, $b = (m_1 + m_2) J_2 + 2m_2 K_2 (1 - \cos \xi) + m_1 G_2$, and $c = 2K_2 (J_2 + G_2) (1 - \cos \xi) + J_2 G_2$. The amplitude ratio for each mode is given by

$$\phi_{L/U} = \left\{ \begin{array}{c} \frac{-\omega_{L/U}^2 m_2 + J_2 + G_2}{J_2} \\ 1 \end{array} \right\} \quad (6.13)$$

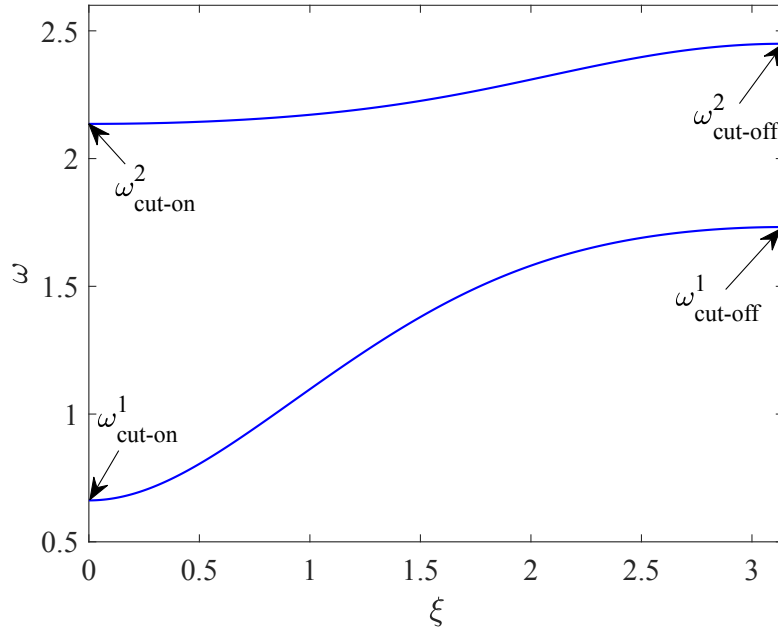


Figure 6.2: Linear dispersion relation for the chain with elastic foundation.

Fig. 6.2 depicts the dispersion relation of the linearized model obtained for an arbitrary choice of parameters: $m_1 = 1$, $m_2 = 0.5$, $K_2 = J_2 = G_2 = 1$. Visual inspection of the plot reveals a few peculiar dispersive characteristics of the chain. (1) The system is fully gapped at low frequencies, between 0 and the cut-on frequency for the first branch $\omega_{\text{cut-on}}^1$, as expected for a chain on an elastic foundation. (2) A locally-resonant bandgap is opened in the interval between $\omega_{\text{cut-off}}^1$ and $\omega_{\text{cut-on}}^2$. The positive group velocity exhibited by the upper branch at $\xi = 0$ is another clear signature of a locally-resonant mechanism.

6.1.2 Nonlinear correction of the dispersion relation

We now follow the framework presented in Chapter 5 to determine the nonlinear correction of the dispersion relation. In the case of harmonic boundary excitation, the wavenumber shifts can be resolved upon the elimination of the secular terms at $O(\epsilon_1)$, leading to the following equation

$$\frac{\partial A}{\partial \tau} + \lambda_0 \sin \left(\xi - \epsilon_1 \frac{\beta}{s} \right) \frac{\partial A}{\partial s} + i\mu |A|^2 A = 0 \quad (6.14)$$

where $\lambda_0 = \frac{K_2 |\phi_u|^2}{\omega \bar{m}}$ and $\mu = \frac{3G_4 |\phi_v|^4}{2\omega \bar{m}}$. Note that Eq. 6.14 has the same form as Eq. 5.32, albeit with different values for the coefficients. The amplitude A can be written in polar form as

$$A(s, \tau) = \alpha(s, \tau) e^{-i\beta(s, \tau)} \quad (6.15)$$

Substituting Eq. 6.15 in Fig. 6.14 leads to the following equations for α and β

$$\begin{aligned} \frac{\partial \alpha}{\partial \tau} + \lambda_0 \sin \left(\xi - \epsilon_1 \frac{\beta}{s} \right) \frac{\partial \alpha}{\partial s} &= 0 \\ \frac{\partial \beta}{\partial \tau} + \lambda_0 \sin \left(\xi - \epsilon_1 \frac{\beta}{s} \right) \frac{\partial \beta}{\partial s} &= \mu \alpha^2 \end{aligned} \quad (6.16)$$

The particular solution of β can be assumed as $\beta^* = C_1 s = C_1 \epsilon_1 n$ if plane wave solution is allowed, where C_1 is a constant. Substituting it into Eq. 6.16 and noticing that $\alpha = A_0$ under boundary excitation with constant amplitude A_0 , yields the transcendental equation for C_1

$$\lambda_0 C_1 \sin \tilde{\xi} = \mu A_0^2 \quad (6.17)$$

where $\tilde{\xi} = \xi - \epsilon_1 C_1$. Once the root of Eq. 6.17 has been numerically determined, the corrected dispersion relation can be computed using the updated wavenumber $\tilde{\xi}$, resulting in the curves of Fig. 6.3. Then, the fundamental solution with the updated wavenumber shift $\tilde{\xi}$ can be expressed compactly as

$$\mathbf{u}_n^0 = A_0 \phi e^{i(\tilde{\xi}n - \omega t)} + c.c. \quad (6.18)$$

This result leads to a few interesting observations. When a correction in ξ is enforced, the corrected dispersion branches (i.e., the dash-dotted red curves in Fig. 6.3 using the same parameters for the linear case with $\epsilon_1 = 0.1$ and $A = 1$) are not defined over the entire reduced Brillouin zone (i.e., the band clipping effect introduced in the Chapter 5). This is in contrast with the frequency shift [79], which is defined for every ξ . This implies that, at certain wavenumbers (especially, approaching the 0 and π limits), wave propagation is forbidden in the nonlinear system if a boundary condition is imposed. The reasonableness and physical implications of this result will be substantiated via numerical simulations in the following sections.

6.1.3 Second harmonic generation and its correction shift

It has been shown that, in the presence of quadratic nonlinearity, the complete solution at $O(\epsilon_2)$ encompasses a non-oscillatory term and an oscillatory contribution, the latter comprising the solution of the corresponding homogeneous problem and the particular (forced) solution due to the forcing term \mathbf{f}^2 [65]. The question we address here is whether the presence of cubic nonlinear springs in the foundation introduces additional tuning effects that are appreciated at the level of these second harmonic contributions. To this end, in the following we derive a general expression for the second harmonic solution that explicitly incorporates any spectral modulation due to such nonlinear interplay.

If we substitute the associated fundamental solution (i.e., Eq. 6.18) in Eq. 6.5, the expression for the forcing function (note that only the first component f_u^2 of \mathbf{f}^2 is non-zero) can be determined as (details about the derivation are given in Appendix D)

$$f_u^2 = -8iK_3 A_0^2 \phi_u^2 \sin \tilde{\xi} \sin^2 \frac{\tilde{\xi}}{2} e^{2i\tilde{\theta}_n} + c.c. \quad (6.19)$$

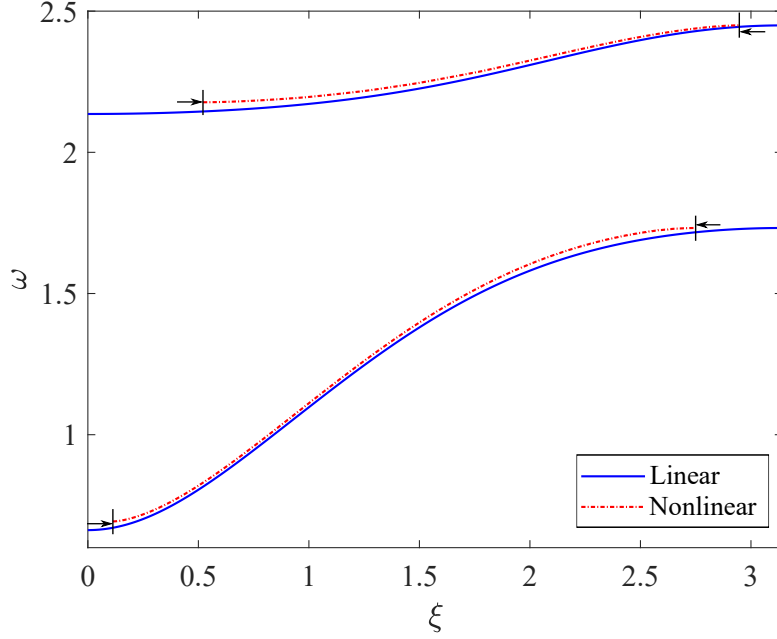


Figure 6.3: Dispersion correction under harmonic boundary excitation.

where $\tilde{\theta}_n = \tilde{\xi}n - \omega t$ and $\tilde{\xi}$ is the corrected wavenumber introduced above and, by working with $\tilde{\xi}$, we implicitly assume that the excitation is prescribed as a boundary condition. Since the coefficient in front of $e^{2i\tilde{\theta}_n}$ is purely imaginary, this expression suggests a phase shift in the second harmonic.

Forced solution and its correction

Following the standard procedure for heterogeneous PDEs, the forced solution can be found as

$$\mathbf{u}_n^{2f} = B_1 \boldsymbol{\varphi} e^{2i\tilde{\theta}_n} + c.c. \quad (6.20)$$

where the coefficient can be obtained by plugging Eq. 6.20 in Eq. 6.5, yielding

$$B_1 \boldsymbol{\varphi} = \left[-4\omega^2 \mathbf{M} + \mathbf{K}(\tilde{\xi}) \right]^{-1} \bar{\mathbf{f}}^2 \quad (6.21)$$

where $\bar{\mathbf{f}}^2 = \begin{Bmatrix} -8iK_3A_0^2\phi_u^2 \sin \tilde{\xi} \sin^2 \frac{\tilde{\xi}}{2} \\ 0 \end{Bmatrix}$ and φ is subjected to the same normalization followed for the fundamental modal vector ϕ . The phase $2i\tilde{\theta}_n$ indicates that \mathbf{u}_n^{2f} represents a harmonic wave traveling with $2\tilde{\xi}$ and 2ω , i.e., twice the frequency and twice the (corrected) wavenumber of the fundamental harmonic \mathbf{u}_n^0 . While the doubling of frequency and wavenumber is an expected feature of the forced response in systems with quadratic nonlinearity [65, 66], the dependence on $\tilde{\xi}$ introduces a new spectral control that is germane to the problem with additional cubic nonlinearity. In essence, cubic nonlinearity introduces an additional wavenumber shift in the signature of the quadratically-generated forced second harmonic. We conclude that the interplay between the two types of nonlinearity results in a new amplitude-dependent correction mechanism that endows traveling waves with an additional self-manipulation capability. We now proceed to check whether a similar effect is observed in the homogeneous part of the SHG.

Homogeneous solution and its correction

The homogeneous solution can be expressed as

$$\mathbf{u}_n^{2h} = iB_2\boldsymbol{\chi}e^{i\psi_n} + c.c. \quad (6.22)$$

In contrast with the forced response, here the phase $\psi = \xi(2\omega)n - 2\omega t$ involves the frequency-wavenumber pair predicted by the branch of the band diagram available at 2ω , thus conforming to the dispersion relation of the corresponding liner problem. Accordingly, $\boldsymbol{\chi} = \begin{Bmatrix} \chi_u \\ \chi_v \end{Bmatrix}$ is the modal vector at $(\xi(2\omega), 2\omega)$, and the imaginary constant i is assumed a priori in Eq. 6.22 to simplify the analysis.

In the spirit of multiple scale analysis, the amplitude term B_2 is, in general, taken to be dependent upon the slow variables s and τ , and can be expressed as

$$B_2(s, \tau) = a(s, \tau) e^{-ib(s, \tau)} \quad (6.23)$$

The full characterization of the homogeneous response relies on the non-trivial task of determining $B_2(s, \tau)$. To this end, we introduce a manipulation step aimed at virtually extending to the second harmonic the treatment, classically reserved for fundamental

harmonic, that we followed in section 1.1 for the determination of $A(s, \tau)$. Specifically, we formally combine the homogeneous second harmonic and the fundamental harmonic into a new baseline expression, which we will treat as the “new fundamental solution” at $O(1)$:

$$\hat{\mathbf{u}}_n^0 = A\phi e^{i\theta_n} + A^* \phi^* e^{-i\theta_n} + i\epsilon_2 B_2 \chi e^{i\psi_n} - i\epsilon_2 B_2^* \chi^* e^{-i\psi_n} \quad (6.24)$$

Accordingly, the equation at $O(\epsilon_1)$ is also updated, and the cubic nonlinear term in \mathbf{f}^1 becomes

$$\begin{aligned} f_{cubic}^1 &= -G_4 \left(v_n^0 \right)^3 = -G_4 \left(A\phi_v e^{i\theta_n} + A^* \phi_v^* e^{-i\theta_n} + i\epsilon_2 B_2 \chi_v e^{i\psi_n} - i\epsilon_2 B_2^* \chi_v^* e^{-i\psi_n} \right)^3 \\ &= -3G_4 \left(|A|^2 |\phi_v|^2 A\phi_v + 2\epsilon_2^2 |B_2|^2 |\chi_v|^2 A\phi_v \right) e^{i\theta_n} \\ &\quad - 3i\epsilon_2 G_4 \left(2|A|^2 |\phi_v|^2 B_2 \chi_v + \epsilon_2^2 |B_2|^2 |\chi_v|^2 B_2 \chi_v \right) e^{i\psi_n} + c.c. \end{aligned} \quad (6.25)$$

where higher order terms have been omitted. Following the same logic described in section 1.1, the removal of the secular terms for the wave modes associated with $e^{i\theta_n}$ and $e^{i\psi_n}$ requires that

$$\frac{\partial A}{\partial \tau} + \lambda_0 \sin \left(\xi - \epsilon_1 \frac{\beta}{s} \right) \frac{\partial A}{\partial s} + i \left(\mu |A|^2 + \epsilon_2^2 \eta |B_2|^2 \right) A = 0 \quad (6.26)$$

and

$$\frac{\partial B_2}{\partial \tau} + \lambda'_0 \sin \left(\xi(2\omega) - \epsilon_1 \frac{b}{s} \right) \frac{\partial B_2}{\partial s} + i \left(\mu' |A|^2 + \epsilon_2^2 \eta' |B_2|^2 \right) B_2 = 0 \quad (6.27)$$

where $\eta = \frac{3G_4 |\chi_v|^2 |\phi_v|^2}{\omega \bar{m}}$; $\lambda'_0 = \frac{K_2 |\chi_u|^2}{2\omega \bar{m}}$; $\mu' = \frac{3G_4 |\phi_v|^2 |\chi_v|^2}{2\omega \bar{m}}$; $\eta' = \frac{3G_4 |\chi_v|^4}{4\omega \bar{m}}$. Ignoring the high order term $O(\epsilon_2^2)$, Eq. 6.26 reduces back to Eq. 6.14, whose solution yields the dispersion shift in the fundamental harmonic, as discussed before. Similarly, neglecting high order term in Eq. 6.27, the equation becomes

$$\frac{\partial B_2}{\partial \tau} + \lambda'_0 \sin \left(\xi(2\omega) - \epsilon_1 \frac{b}{s} \right) \frac{\partial B_2}{\partial s} + i\mu' |A|^2 B_2 = 0 \quad (6.28)$$

which is a partial differential equation in s and τ controlling the slow spatio-temporal evolution of B_2 . Substituting Eq. 6.23 in Eq. 6.28 and assuming $b = C_2 s = \epsilon_1 C_2 n$ (a priori assumption which leads to a traveling wave solution if C_2 can be solved as a real

number), yields a transcendental equation formally similar to Eq. 6.17, which can be solved numerically for C_2 . With C_2 , the homogeneous solution can be rewritten as

$$\mathbf{u}_n^{2h} = ia\chi e^{i\hat{\psi}_n} + c.c. \quad (6.29)$$

where $\hat{\psi}_n = \hat{\xi}n - 2\omega t$ and $\hat{\xi} = \xi(2\omega) - \epsilon_1 C_2$. This result shows that the Q-C interplay leads to a new dispersion shift that is germane to the homogeneous second harmonic.

Phase matching conditions

A careful inspection on Eq. 6.21 suggests that the above procedures for finding the solutions at $O(\epsilon_2)$ works only when $-4\omega^2\mathbf{M} + \mathbf{K} \equiv \mathbf{Q}$ is invertible. It is possible, however, that \mathbf{Q} is singular ($\det(\mathbf{Q}) = 0$). If that is the case, the term containing the variable $2\tilde{\theta}$ in the forcing function \mathbf{f}^2 satisfies the linear eigenvalue problem of Eq. 6.11. In other words, the forcing function resonates with the homogeneous solution (i.e., $2\tilde{\theta}_n = \psi_n$) and the solution becomes secular. Such scenario is referred to as phase matching condition (PMC) and in general has been shown to be conducive to stronger nonlinear response signatures [99, 100]. The solution, which is assumed to grow in direct proportion to the propagation distance, is expressed as

$$\mathbf{u}_n^2 = D\chi n e^{2i\tilde{\theta}_n} + c.c. \quad (6.30)$$

Substituting it in Eq. 6.5, yields

$$D \left(-4\omega^2\mathbf{M} + \mathbf{K}(\tilde{\xi}) \right) \chi n + D\mathbf{p} = \bar{\mathbf{f}}^2 \quad (6.31)$$

where $\mathbf{p} = -K_2 \begin{Bmatrix} 2i\chi_u \sin 2\tilde{\xi} \\ 0 \end{Bmatrix}$. The first term in the LHS of Eq. 6.31 automatically vanishes since it satisfies the eigenvalue problem Eq. 6.11, as stated above. Then, the coefficient D can be determined as: $D = \frac{4K_3 A_0^2 \phi_u^2 \sin \tilde{\xi} \sin^2 \frac{\tilde{\xi}}{2}}{K_2 \chi_u \sin 2\tilde{\xi}}$.

As we mentioned earlier in the manuscript, this type of nonlinear system also supports a non-oscillatory solution - a general nonlinear effect in anharmonic lattices [66]. For completeness, let us briefly re-examine the forcing term at $O(\epsilon_2)$ (see Appendix D), in which we notice that a constant force can be induced in each quadratic spring.

$$F_s = 2\epsilon_2 K_3 A_0^2 |\phi_u|^2 \left(1 - e^{-i\tilde{\xi}} \right) \left(1 - e^{i\tilde{\xi}} \right) = 4\epsilon_2 K_3 A_0^2 |\phi_u|^2 (1 - \cos \tilde{\xi}) \quad (6.32)$$

This constant force results in a stationary displacement \mathbf{u}_n^{2s} in the system, and such static problem can be easily solved once the size (i.e., the total number of degrees of freedom) of the system is specified. As a side note, it is worth noticing that the magnitude of the force term in Eq. 6.32 contains the corrected wavenumber $\tilde{\xi}$. As a result, we can expect that the strength of the stationary displacement u_n^{2s} will also be moderately affected by the presence of cubic springs in the foundation. In conclusion, the complete solution at $O(\epsilon_2)$ can be expressed as

If $2\tilde{\theta}_n \neq \psi_n$ (Non-PMC):

$$\mathbf{u}_n^2 = \mathbf{u}_n^{2s} + B_1 \varphi e^{2i\tilde{\theta}_n} + ia\chi e^{i\hat{\psi}_n} + c.c. \quad (6.33)$$

If $2\tilde{\theta}_n = \psi_n$ (PMC):

$$\mathbf{u}_n^2 = \mathbf{u}_n^{2s} + D\chi n e^{2i\tilde{\theta}_n} + c.c. \quad (6.34)$$

Imposing the absence of second harmonic and of non-oscillatory terms at the boundary ($n = 0$), it yields $b_0 = 0$ and $a = iB_1\varphi_v/\chi_v$, and the unknowns in \mathbf{u}_n^{2s} can be fully determined.

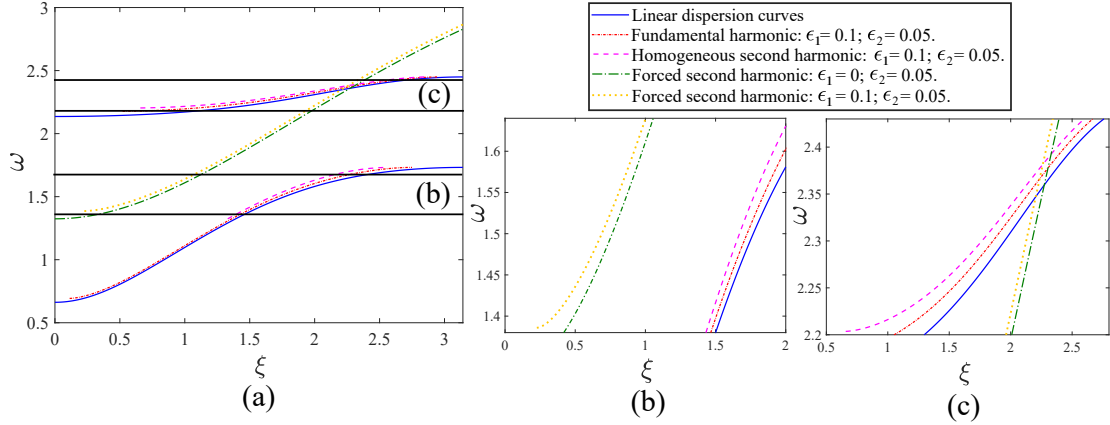


Figure 6.4: (a) Dispersion shifts in the fundamental and second harmonics. (b-c) Zoomed details of the (b) lower branch and (c) upper branch, with amplitude $A_0 = 1$.

Equations 6.33 and 6.34 shed light over some unique characteristics of the nonlinearly-generated second harmonics, which are summarized below:

1) The shift in wavenumber introduced by the cubic nonlinearity at $O(\epsilon_1)$, is also observed in the forced solution at the second harmonic. However, the shift at the second

harmonic is magnified by a factor of 2 (i.e., $2\Delta\xi = 2(\tilde{\xi} - \xi)$), which implies that the spectral signatures of the forced second harmonic can be modified to a larger extent than the fundamental harmonic by playing with the amplitude of excitation.

2) We have shown that the interaction between the quadratic and cubic nonlinearities produces a new dispersion shift in the second harmonics, which is conceptually distinct from the shift in the fundamental harmonic. In other words, at a given frequency, two shifts are defined: the one experienced by a fundamental harmonic excited directly at that frequency and the one experienced by the second harmonic generated by an excitation with half frequency content. We note that the dispersion shift in the homogeneous second harmonic (dashed magenta curves) is significantly larger (precisely twice larger) when compared to the shift in the fundamental solution (dash-dotted red curves) at that frequency. A visual comparison of these shifts is provided in Fig. 6.4 for different frequencies and strengths of nonlinearity. This unique feature enables an additional array of wave manipulation opportunities, as will be discussed in the application section below.

3) When PMC is achieved, the amplitude of the second harmonic grows with the propagation distance, and the full nonlinear response conforms to the linear dispersion relation. As discussed in [99, 100], this unique property has important practical implications. The energy tunneling induced by the SHG from the fundamental to second harmonic can be boosted by enabling PMC.

4) In the presented multiple scales analysis, the selection of the scale variables is deliberately chosen to capture the main effects of quadratic and cubic nonlinearities in the system. A more general choice, up to $O(\epsilon_2)$ would include: $\theta_n = \xi n - \omega t$; $s_1 = \epsilon_1 n$; $\tau_1 = \epsilon_1 t$; $s_2 = \epsilon_2 n$; $\tau_2 = \epsilon_2 t$. However, the two additional variables s_2 and τ_2 will not add any new information to the existing solutions in our context. This can be explained by recalling that the main purpose of introducing the slow variables s and τ is to capture the shift in the dispersion relation. To the first order approximation (i.e., at $O(\epsilon_1)$), this is brought about exclusively by the cubic nonlinearity, while the shift due to quadratic nonlinearity is negligible [109]. Another consequence of this argument is that the presented perturbation analysis also works when ϵ_2 is comparable to ϵ_1 , i.e., $\epsilon_1 \approx \epsilon_2$. Under these circumstances, Eq. 6.5 and Eq. 6.6 can be combined into one equation with the two forcing functions \mathbf{f}^1 and \mathbf{f}^2 , and the rest of the procedure remains the same.

6.2 Full-scale simulations

In this section, we perform full-scale numerical simulations to validate our analytical model and support the findings detailed in section 2. The wave response of a finite chain is obtained by integrating the system of nonlinear equations (Eq. 6.2) using Verlet Algorithm [106]. In order to obtain clean signatures of the desired harmonics, it is imperative to work with traveling waves that are as monochromatic as possible. This can be achieved by prescribing sustained harmonic excitations at the boundary. However, this route is impractical with finite-size systems as reflections from the boundaries would soon result in standing waves (i.e., vibration states).

To prescribe purely harmonic traveling waves while avoiding boundary reflections, we implement an absorbing layer of 30 unit cells endowed with viscous damping at the end of the main chain which consists of 40 undamped unit cells. The coefficient profile for the n^{th} unit cell in the absorbing layer is given by

$$\mathbf{C}_n = C_0 \left(\frac{n}{N_{\text{PML}}} \right)^\gamma \mathbf{I} \quad (6.35)$$

where $C_0 = 3$ is the maximum damping coefficient, $N_{\text{PML}} = 30$ denotes the number of unit cells in the layer, γ is set to 3 in the simulation, and \mathbf{I} is the 2×2 identity matrix. A continuous harmonic displacement excitation is applied to mass m_2 in the first unit cell of the chain. The spatio-temporal response computed at each cell site over the considered time interval is transformed to the Fourier domain via two-dimensional Discrete Fourier Transform (2D-DFT). The spectral components (ξ, ω) of the response, to be compared against the band diagrams from unit cell analysis, are extracted by tracking the maximum values of the 2D-DFT data in different frequency intervals.

The system parameters are $m_1 = 1$, $m_2 = 0.5$, $K_2 = J_2 = G_2 = 1$, $\epsilon_1 = 0.1$. The cubic nonlinearity can be positive ($G_4 = 1$) or negative ($G_4 = -1$), which corresponds to a hardening or softening nonlinear foundation, respectively. The amplitude of the excitation A_0 is set to 1 for the lower branch correction (Fig. 6.5(a)) and to 0.6 for the upper branch correction (Fig. 6.5(b)). First, we perform a series of simulations to characterize the wavenumber shifts in the fundamental harmonic. The 2D-DFT data of the numerical results is plotted in Fig. 6.5, which indicates an excellent agreement between the numerical simulations and the multiple scales analysis. It is worth noting

that the branches are shifted upward or downward depending on whether hardening or softening is considered.

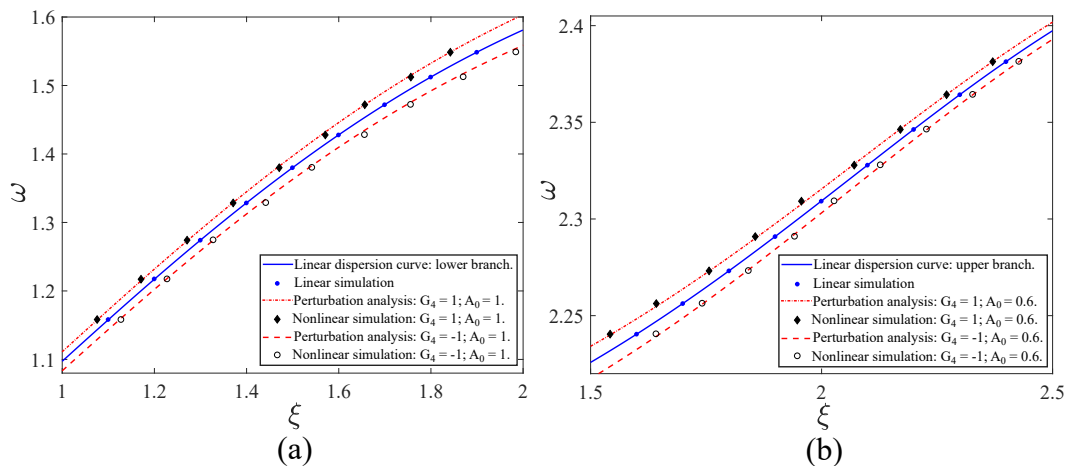


Figure 6.5: Numerical estimation of the dispersion shift in the lower (a) and upper (b) branches of the band diagram, compared with the analytical model based on perturbation analysis.

Now, we incorporate quadratic nonlinearity ($K_3 = 1$ and $\epsilon_2 = 0.05$) in the springs of the main chain to elicit second harmonic generation and estimate its spectral shift. The spectral content of the forced second harmonic is determined by the $(\tilde{\xi}, 2\omega)$ pair, and the homogeneous one is dictated by the $\hat{\xi} - 2\omega$ curve. Both wavenumbers $\tilde{\xi}$ and $\hat{\xi}$ are subjected to (different) correction shifts and depend on the excitation amplitude A_0 . Fig. 6.6 shows the numerical results of the dispersion shift in the second harmonics. Two scenarios can be identified. In a certain frequency range, the forced and homogeneous solutions co-exist, as shown in Fig. 6.6(a). In the frequency range where no modes are available, only the forced solutions is observed, as shown in Fig. 6.6(b). In both cases, the agreement between the analytical and numerical results is remarkable. Comparing Fig. 6.5(a) against Fig. 6.6(b), and Fig. 6.5(b) against Fig. 6.6(a), we can easily conclude that the wavenumber shifts in the homogeneous and forced second harmonics are significantly larger than those exhibited by the fundamental harmonics under the same amplitudes of the excitation, consistently with the prediction of the multiple scales analysis.

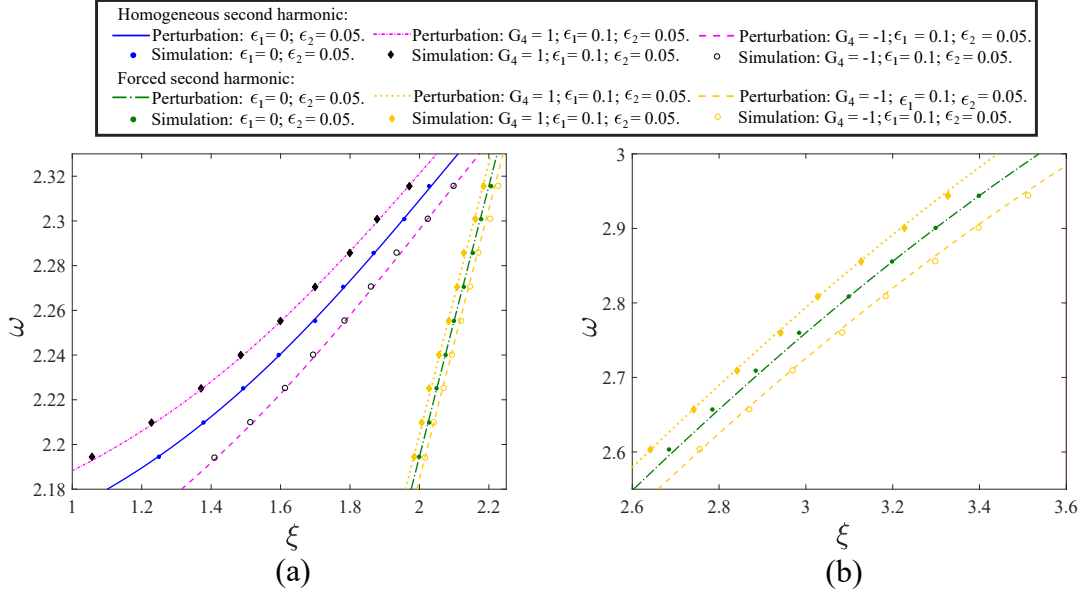


Figure 6.6: Numerical estimation of dispersion shift in the second harmonics (a) in frequency range where homogeneous and forced solutions co-exist ($A_0 = 0.6$), and (b) in frequency range where only the forced solution exists ($A_0 = 1$).

6.3 Application for self-switching capabilities

In this section we demonstrate that the extreme tunability of the second harmonic enabled by the cubic nonlinearity allows controlling the spectral characteristics of the nonlinear wave response due to the quadratic nonlinearity, and activate new modal functionalities at the second harmonic. One interesting application is to design a family of self-adaptive modal switches that can turn on and off some desired functionalities by simply adjusting the amplitude of excitation. Here we illustrate the richness of opportunities resulting from this idea through two illustrative examples.

6.3.1 Application 1: Optical mode switch

The first example exploits the possibility to control the manifestation of the homogeneous second harmonic (due to quadratic nonlinearity) through the cubic term. This allows activating/deactivating or tuning certain modal characteristics typical of the higher-frequency optical regime that are nonlinearly activated in the response via SHG.

This application is based on the notion that, when a wave mode (dispersion branch) is available at the second harmonic, the homogeneous solution will display the spectral modal characteristics of that mode [99]. If the second harmonic is subjected to a dispersion shift, e.g., through cubic nonlinear correction, the modal characteristics of the activated harmonic can be further manipulated with respect to the default case with only quadratic nonlinearity. This concept is illustrated in Fig. 6.7 and supported by numerical simulations performed with the same parameters used in section 2. The excitation frequency ω_0 (red dot in Fig. 6.7(a)) is carefully chosen such that the second harmonic $2\omega_0$ is above, but sufficiently close to, the cut-on frequency $\omega_{\text{cut-on}}^2$ of the upper branch. Thus, at low amplitude (or without cubic nonlinearity), the

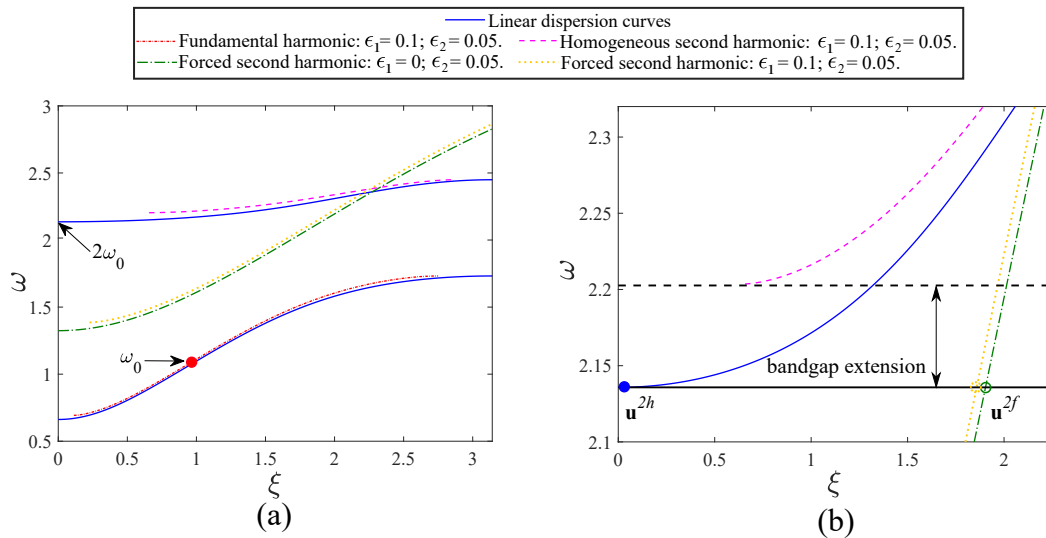


Figure 6.7: Schematic of a self-adaptive switch which can turn on/off homogeneous second harmonic. (a) Entire band diagram, and (b) zoomed details at the second harmonic frequency.

homogeneous second harmonic is located at the onset of the upper branch (around the blue dot in Fig. 6.7(b)), whose response involves large motion of mass m_2 (a typical feature of locally resonant bandgaps). The forced solution is marked by the green circle located on the dash-dotted green curve, which represents the locus of the $2\xi - 2\omega$ pairs. At high amplitude ($A_0 = 1$), the dispersion relation is corrected. As a result, the forced second harmonic is shifted from the location of the green circle to the location of the yellow dotted circle, while the homogeneous second harmonic is in the bandgap

extension produced by the upshifted upper branch (magenta dashed curve).

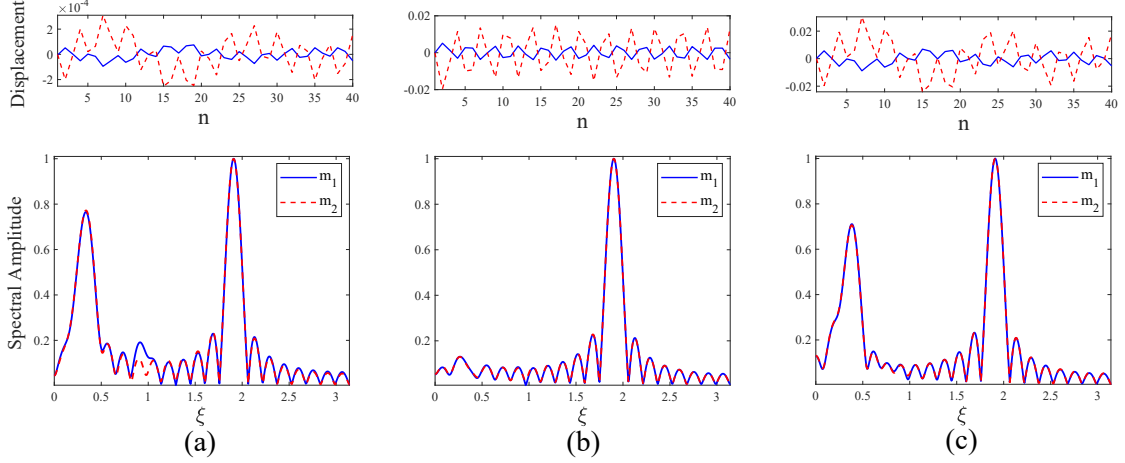


Figure 6.8: Spatial profile and DFT of the filtered second harmonics for mass m_1 (the solid blue curves) and m_2 (the dashed red curves). (a) Low amplitude $A_0 = 0.1$ with $\epsilon_1 = 0.1$ and $\epsilon_2 = 0.05$. (b) High amplitude $A_0 = 1$ with $\epsilon_1 = 0.1$ and $\epsilon_2 = 0.05$. (c) High amplitude $A_0 = 1$ with $\epsilon_2 = 0.05$ (no cubic nonlinearity).

In simulations, the prescribed excitation frequency is chosen to be $\omega_0 = 1.07$ rad/s such that the second harmonic is around $2\omega_0 = 2.14$ rad/s, which is close to the cut-on frequency $\omega_{\text{cut-on}}^2$, as desired. A band-pass filter is used to extract the second harmonics from the nonlinear response. Fig. 6.8 depicts the spatial profiles and the normalized DFT of the filtered second harmonics for mass m_1 and mass m_2 . With a low-amplitude excitation, as shown in Fig. 6.8(a), we observe that there are two peaks in the spectral domain: the one with lower wavenumber corresponds to the homogeneous solution, and the other to the forced solution. This is consistent with the spatial profile, where the wave presents an amplitude modulation - a typical feature of waves with two co-existing spectral components. At high amplitude, the first peak is eliminated, and the wavefield becomes monochromatic, as depicted in Fig. 6.8(b). In comparison, in Fig. 6.8(c) we consider a case where we retain a high amplitude of excitation but we remove the cubic nonlinearity in the system. We see that all the major wave signatures are qualitatively similar to case (a), albeit with higher displacement amplitude. This indicates that the SHG due to quadratic nonlinearity is triggered under large amplitude excitations, but the additional correction (filtering of the homogeneous component) due to the cubic

term in the foundation is lost. In essence, we have demonstrated that, by playing with the amplitude of the excitation and with cubic nonlinearity to exploit, we obtain a double tuning effect on the wave: 1) we trigger and control the strength of the second harmonic (this effect would be observed even without cubic term); 2) we selectively determine whether the homogeneous solution is observed in the second harmonic in addition to the forced one (this effect is germane to the case with double nonlinearity) and therefore we determine whether two distinct wavenumbers and modal characteristics will co-exist in the response. In summary, by controlling the amplitude, not only do we control the strength of the second harmonic; we also inherently dictate its spectral and modal content.

6.3.2 Application 2: Adaptive PMC switch

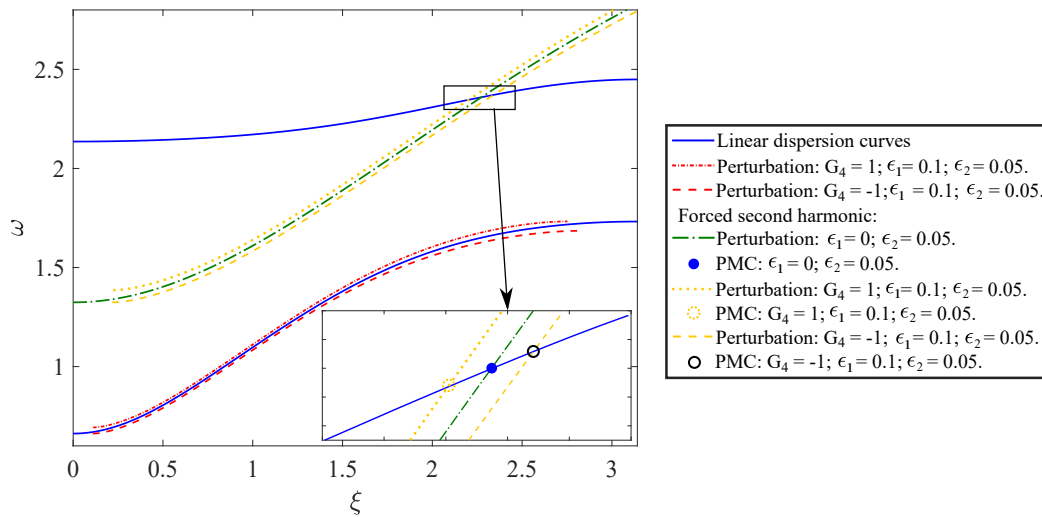


Figure 6.9: Schematic of tunable PMC with hardening or softening cubic nonlinearity at amplitude $A_0 = 1$.

The second example exploits the possibility to interfere with the establishment of PMC in the second harmonic through the cubic correction. Since the strength of the harmonic generation under PMC is largely magnified, the entire modal manifestation of the second harmonic can be dramatically changed depending on whether PMC is enabled or not.

As discussed in the theory section, if PMC is achieved, the amplitude of the solution

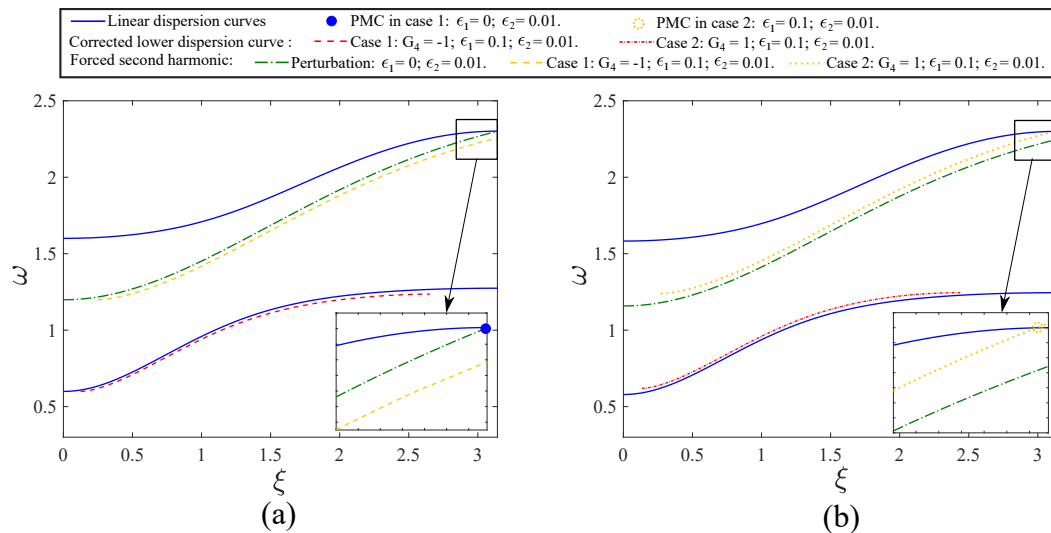


Figure 6.10: Schematic of self-adaptive PMC switches: (a) Case 1: switching *off* PMC at high amplitude via hardening cubic nonlinearity; (a) Case 2: switching *on* PMC at high amplitude via softening cubic nonlinearity.

at $O(\epsilon_2)$ is proportional to the propagation distance. This unique feature can be utilized to boost SHG, overall emphasizing the nonlinear response. However, for a given system with only quadratic nonlinearity, PMC is strictly linked to specific frequencies, or even not available at all, based on the fixed characteristics of the band diagram. In contrast, by incorporating cubic nonlinearity in the system and by exploiting its manifestation on the correction of the dispersion branches, we can instead switch on/off PMC in a certain frequency range, as shown in Fig. 6.9. Based on its mathematical definition, the geometrical interpretation of PMC is the existence of an intersection between the linear dispersion curves and the curve encompassing all the forced second harmonic pair (the $2\tilde{\xi} - 2\omega$ curve). In light of this, in the system with $\epsilon_1 = 0$ (i.e., no cubic nonlinearity) and $\epsilon_2 = 0.05$ depicted in Fig. 6.9 PMC is located at the blue dot (zoomed details shown in the inset). If some hardening cubic nonlinearity ($\epsilon_1 = 0.1$, $G_4 = 1$) is added, PMC is shifted to the yellow dotted circle. In contrast, if softening cubic nonlinearity is added ($G_4 = -1$), PMC are shifted to the solid black circle. In essence, by resorting to different types of cubic nonlinearity, PMC becomes highly tunable, providing another way to manipulate nonlinear wave propagation at the second harmonic.

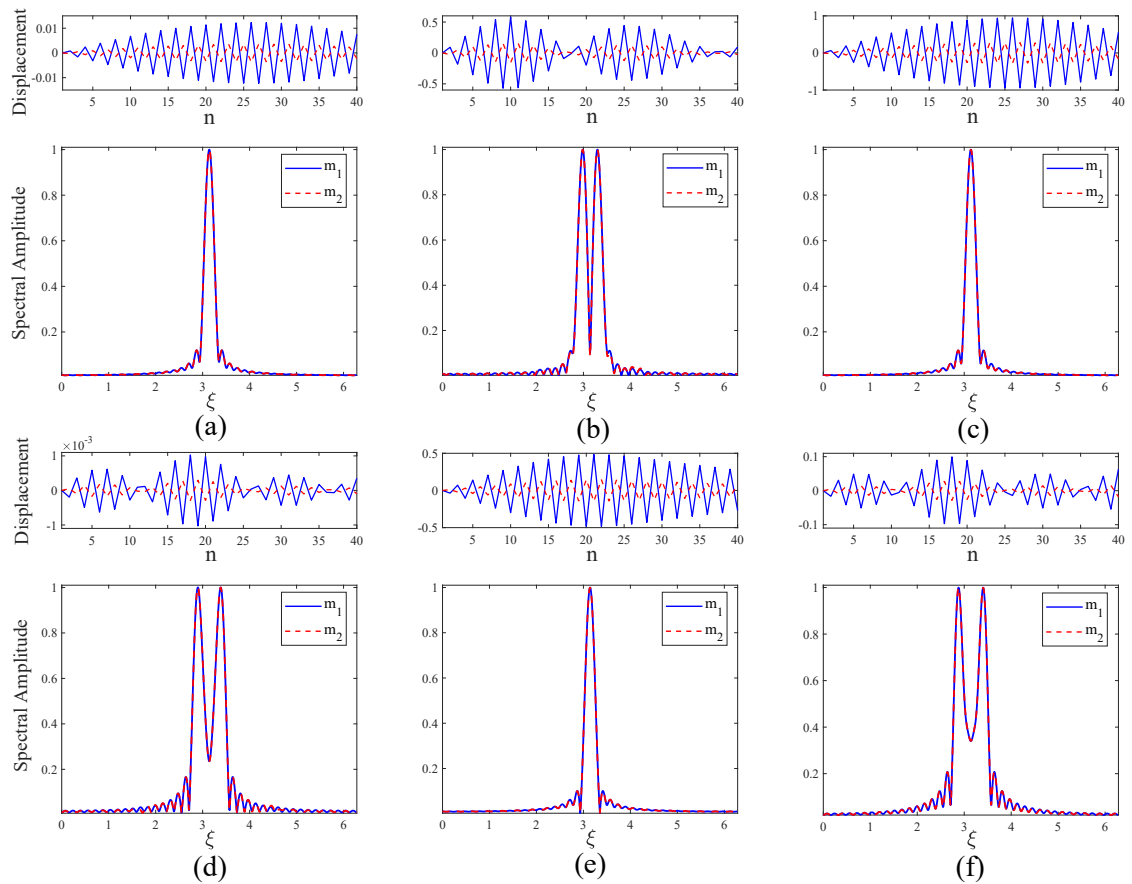


Figure 6.11: Spatial profile and DFT of the filtered second harmonics for the two cases of self-adaptive PMC switch. Case 1: (a) Low amplitude $A_0 = 0.1$ with $G_4 = 1$, $\epsilon_1 = 0.1$, $\epsilon_2 = 0.01$. (b) High amplitude $A_0 = 1$ with $G_4 = 1$, $\epsilon_1 = 0.1$, $\epsilon_2 = 0.01$. (c) High amplitude $A_0 = 1$ with $\epsilon_2 = 0.01$ (no cubic nonlinearity). Case 2: (d) Low amplitude $A_0 = 0.1$ with $G_4 = -1$, $\epsilon_1 = 0.1$, $\epsilon_2 = 0.01$. (e) High amplitude $A_0 = 1$ with $G_4 = -1$, $\epsilon_1 = 0.1$, $\epsilon_2 = 0.01$. (f) High amplitude $A_0 = 1$ with $\epsilon_2 = 0.01$ (no cubic nonlinearity).

To illustrate this capability, we consider two chains. The parameters of chain 1 (with softening foundation) are $m_1 = m_2 = 1$, $K_2 = J_2 = 1 = 1$, $G_2 = 0.92$, $G_4 = -1$, $\epsilon_1 = 0.1$, and $\epsilon_2 = 0.01$. Chain 2 (with hardening foundation) features $G_2 = 0.84$, $G_4 = 1$, while all the other coefficients are kept identical. For amplitude $A_0 = 1$, the corrected dispersion relations for both systems are plotted in Fig. 6.10 and superimposed to the linear ones. In the first case, the system features one PMC (blue dot in the inset of Fig. 6.10(a)) close to the upper cut-off frequency, when excited with low amplitude or without cubic nonlinearity. By increasing the amplitude, the PMC can be switched off due to the activated dispersion shift (the yellow dashed curve). In the second case, there is no PMC available at low amplitude, but a new one (i.e., the yellow dotted circle in Fig. 6.10(b)) can be created as we increase the amplitude to a certain degree and produce the correction marked by the yellow dotted curve.

Next, we perform numerical simulations for both chains. The filtered second harmonics in the spatial and spectral domains for mass m_1 and mass m_2 are plotted in Fig. 6.11. For chain 1, the excitation frequency is carefully chosen such that the second harmonic is close to the blue dot. At low excitation amplitude ($A_0 = 0.1$), PMC is achieved as designed, as confirmed by the fact that the spectrum only contains one dominant wavenumber component, as shown in Fig. 6.11(a). As a result, the response at the second harmonic grows in space, as predicted from the analytical solution. Note however that, in practice, the harmonic starts losing intensity beyond a certain stage in the simulation. This reduction in amplitude is not captured by our perturbation analysis, because it occurs when the second harmonic, under PMC, is accumulated to a different order other than $O(\epsilon_2)$, which violates the order assumption in Eq. 6.3. At high amplitude ($A_0 = 1$), the PMC is switched off, and the second harmonic splits into two parts, one corresponding to the homogeneous response and the other denoting the forced response, which globally result a modulation in amplitude, as shown in Fig. 6.11(b). In comparison, the result obtained with high amplitude of excitation but without additional cubic nonlinearity is given in Fig. 6.11(c). We see that PMC is again enabled and the response features wave characteristics similar to those observed for the case of Fig. 6.11(a).

In the second case, the excitation frequency is chosen such that the second harmonic is close to the yellow dotted circle, and therefore PMC is not available at low amplitude.

As a result, the response at the second harmonic has two components as shown in the DFT plot of Fig. 6.11(d). As we increase the amplitude to 1, the dispersion shift leads to a nonlinearly-generated PMC, and the corresponding quasi-monochromatic numerical result is plotted in Fig. 6.11(e). However, if we remove the cubic nonlinearity in the system, PMC is again unavailable, as confirmed by the resulting modulated filtered second harmonic shown in Fig. 6.11(f). Similar to the previous example, the chain behaves like a self-adaptive switch, which can turn on and off selected modal characteristics typical of the optical mode via the interplay between cubic nonlinearity and SHG. Unlike the other case, however, here the mechanism is not the selective excitation and suppression of one component (homogeneous) of the second harmonic, but rather the selective activation of PMC and of its amplitude-reinforcing effects.

6.4 Conclusion

In this Chapter, we have studied wave propagation in a quadratic nonlinear spring-mass chain attached to a locally-resonant cubic nonlinear foundation, using a multiple scales analysis and full-scale simulations. We have been able to link the interplay between quadratic and cubic nonlinearity to a number of new nonlinear phenomena, as well as to revisit some more classical tuning and manipulation effects from a different perspective.

First, we have revisited the amplitude-dependent dispersion shift of the fundamental harmonic, which has been known to be the most tangible effect of cubic nonlinearity. We have then considered the phenomenon of second harmonic generation, which is the prominent signature of quadratic nonlinearity. We have shown that, similarly to the fundamental harmonic, both homogeneous and forced second harmonics also feature amplitude-dependent dispersion shifts due to the Q-C nonlinearity interplay. We have presented two examples of tunable chains with self-adaptive switching capabilities. The first example involves activating or deactivating new modal characteristics in the nonlinear response through the dispersion shift induced in the homogeneous second harmonic. The second example shows the capability of switching on and off phase matching conditions to activate and deactivate strong nonlinear signatures at high frequencies. In conclusion, the self-interacting effect of cubic and quadratic nonlinearities provides a

new conceptual platform for the design of nonlinear phononic crystals and metamaterials with superior tunability characteristics.

Chapter 7

Conclusion and future outlook

7.1 Conclusion

In this dissertation, we have systematically investigated wave propagation in periodic structures with special focus on weakly nonlinear effects. Using perturbation techniques, we are able to provide analytical models to characterize the dispersive properties of weakly nonlinear systems, which have been further demonstrated via numerical simulations and experiments. In addition, we have explored the implications of these nonlinear effects for wave control and tunability, thereby offering alternative avenues for the design of tunable acoustic metamaterials.

First, we have focused on the nonlinear effects associated with quadratic nonlinearity. Through a theoretical framework based on fundamental arguments of continuum mechanics, we have shown the main nonlinear effects on wave propagation in 1D geometrically-nonlinear waveguides, including the existence of a non-oscillatory component and the generation of two (homogeneous and forced) second harmonic components (SHG). Moreover, we have shown the complementary modal characteristics exhibited between the fundamental harmonic and the nonlinearly-generated second harmonic and the availability of phase matching conditions (PMC) that can effectively enhance the strength of SHG. Using these analytical findings as guidelines, we have explored these effects in periodic waveguides featuring internal resonators, in which SHG, reinforced upon the establishment of PMC, is employed as a mechanism to transfer considerable

amount of energy to the resonators, therefore enabling energy trapping and harvesting capabilities. Last, we have devoted efforts towards an experimental investigation on SHG in 2D periodic structures with an emphasis on the spatial characteristics of the nonlinear waves. Through a prototype lattice of magnets supported by pillars, we have been able to experimentally confirm all the key nonlinear components activated by SHG and their individual spatial contributions. This result unveiled the complementary directivity patterns displayed by the different harmonic components in the nonlinear response, supporting the argument that nonlinearity can be exploited to activate complementary spatial features that cannot be observed in the corresponding linear structures under the same excitation conditions.

We have then shifted our attention to the tuning effects induced by cubic nonlinearity. To this end, we have proposed an analytical model based on multiple scales analysis to capture the nonlinear dispersion corrections of 1D spring-mass chains excited harmonically at their boundaries. We have demonstrated that the dispersion correction manifests as wavenumber shift, in contrast with the frequency shift typically observed in cases where harmonic initial profiles are prescribed over the spatial domain. We have revealed an unusual dispersion effect resulting from this wavenumber shift, which cuts off a small portion of the dispersion relation near the π limit or the origin of optical branches and therefore can be seen as a clipping of the branch. We have exploited this effect for bandgap tunability in mass-in-mass chains, showing that the tuning capability is only available if the cubic nonlinearity is deployed in the springs supporting the internal resonators.

Finally, we have combined quadratic and cubic nonlinearities in doubly-nonlinear periodic waveguides to investigate the tuning effects resulting from the interplay between the two types of nonlinearity. Specifically, we have shown that the dispersion correction caused by cubic nonlinearity can be used to modify the dispersive characteristics of the second harmonic that is generated by quadratic nonlinearity. Through two illustrative examples, we have demonstrated that this quadratic-cubic interplay can be exploited to achieve self-switching functionalities, including an optical mode switch, which is capable of controlling the activation of some optical modal characteristics in the nonlinear response, and a PMC switch, which can be turned on and off to effectively manage the strength of nonlinear signatures at high frequencies.

In conclusion, this investigation offers a full exploration of the diverse manifestations of quadratic and cubic nonlinearities on wave propagation in periodic structures and the intertwined effects that the two nonlinearities exert on each other. On the technological side, it offers an outlook into the implications of these effects for wave control and tunability, thus providing building blocks for the design of nonlinear acoustic metamaterials with tunable and adaptive functionalities.

7.2 Future outlook

Future expansion of this work could be directed towards the following aspects. First, fundamental understanding on the interactions among nonlinearity, periodicity (or discreteness), dispersion, and boundary conditions is a key component for better modeling of complex wave phenomena in periodic structures. While a large number of studies have focused on the interactions among nonlinearity, periodicity, and dispersion, the potential influence of boundary conditions on the manifestation of nonlinearity has rarely been discussed in the relevant literature. In Chapter 5, we show that boundary conditions, associated with harmonic excitations imposed at boundaries, can effectively dictate how the cubic nonlinear effect (i.e., amplitude-dependent dispersion correction) manifests in the wavenumber-space of the nonlinear response of 1D periodic chains. This finding provides new perspectives on the study of nonlinear waves and brings additional opportunities for tunability and functionality enrichment. Future efforts in this direction could be devoted towards exploring such interplay of nonlinearity and boundary conditions in higher-dimensional periodic structures and its implications for spatial directivity.

The magnetic lattice prototype introduced in Chapter 4 has been shown to be a robust platform for the experimental observation and demonstration of two-dimensional nonlinear wave phenomena. Through this platform, we could be able to experimentally demonstrate other high-dimensional nonlinear wave effects and concepts that leverage those effects for practical applications. One promising avenue out of this perspective is to realize nonlinear topological lattices that can nearly represent the ideal ones, which could be used to explore the interplay between nonlinearity and topological characteristics.

Bibliography

- [1] V.S. Deshpande, N.A. Fleck, and M.F. Ashby. Effective properties of the octet-truss lattice material. *Journal of the Mechanics and Physics of Solids*, 49(8):1747–1769, 2001.
- [2] Z. Liu, X. Zhang, Y. Mao, Y.Y. Zhu, Z. Yang, C.T. Chan, and P. Sheng. Locally resonant sonic materials. *Science*, 289(5485):1734–1736, 2000.
- [3] M.A. Porter, P. G. Kevrekidis, and C. Daraio. Granular crystals: Nonlinear dynamics meets materials engineering. *Physics Today*, 68(11), 11 2015.
- [4] L. Brillouin. *Wave propagation in periodic structures*. Dover, second edition, 1953.
- [5] M.I. Hussein, M.J. Leamy, and M. Ruzzene. Dynamics of phononic materials and structures: Historical origins, recent progress, and future outlook. *Applied Mechanics Reviews*, 66(4):040802, 2014.
- [6] A. Khelif, Y. Achaoui, S. Benchabane, V. Laude, and B. Aoubiza. Locally resonant surface acoustic wave band gaps in a two-dimensional phononic crystal of pillars on a surface. *Physical Review B*, 81:214303, Jun 2010.
- [7] M. B. Assouar, M. Senesi, M. Oudich, M. Ruzzene, and Z. Hou. Broadband plate-type acoustic metamaterial for low-frequency sound attenuation. *Applied Physics Letters*, 101(17):173505, 2012.
- [8] K.H. Matlack, A. Bauhofer, S. Krödel, A. Palermo, and C. Daraio. Composite 3D-printed metastructures for low-frequency and broadband vibration absorption. *Proceedings of the National Academy of Sciences of the United States of America*, 113(30):8386–8390, 2016.

- [9] P. Celli and S. Gonella. Manipulating waves with lego bricks: A versatile experimental platform for metamaterial architectures. *Applied Physics Letters*, 107(8):081901, 2015.
- [10] A. Colombi, D. Colquitt, P. Roux, S. Guenneau, and R.V. Craster. A seismic metamaterial: The resonant metawedge. *Scientific Reports*, 6:27717, 2016.
- [11] A. Colombi, P. Roux, S. Guenneau, P. Gueguen, and R. V. Craster. Forests as a natural seismic metamaterial: Rayleigh wave bandgaps induced by local resonances. *Scientific Reports.*, 6:19238, 2016.
- [12] H.H. Huang, C.T. Sun, and G.L. Huang. On the negative effective mass density in acoustic metamaterials. *International Journal of Engineering Science*, 47(4):610 – 617, 2009.
- [13] R. Zhu, X.N. Liu, G.K. Hu, C.T. Sun, and G.L. Huang. Negative refraction of elastic waves at the deep-subwavelength scale in a single-phase metamaterial. *Nature Communications*, 5:5510, 2014.
- [14] H. Nassar, Y. Y. Chen, and G. L. Huang. Polar metamaterials: A new outlook on resonance for cloaking applications. *Physical Review Letters*, 124:084301, Feb 2020.
- [15] R. Ganesh. Mechanisms of wave manipulation in nonlinear periodic structures (doctoral dissertation). *University of Minnesota, Minneapolis, USA*, 2015.
- [16] R. Massimo, S. Fabrizio, and S. Francesco. Wave beaming effects in two-dimensional cellular structures. *Smart Materials and Structures*, 12(3):363, 2003.
- [17] A.S. Phani, J. Woodhouse, and N.A. Fleck. Wave propagation in two-dimensional periodic lattices. *Journal of the Acoustical Society of America*, 119(4):1995–2005, 2006.
- [18] Alessandro Spadoni, Massimo Ruzzene, Stefano Gonella, and Fabrizio Scarpa. Phononic properties of hexagonal chiral lattices. *Wave Motion*, 46(7):435 – 450, 2009.

- [19] A. Leonard, C. Chong, P.G. Kevrekidis, and C. Daraio. Traveling waves in 2D hexagonal granular crystal lattices. *Granular matter*, 16:531–542, 2014.
- [20] P. Celli and S. Gonella. Laser-enabled experimental wavefield reconstruction in two-dimensional phononic crystals. *Journal of Sound and Vibration*, 333(1):114–123, 2014.
- [21] P. Celli and S. Gonella. Tunable directivity in metamaterials with reconfigurable cell symmetry. *Applied Physics Letters*, 106(9):091905, 2015.
- [22] O.R. Bilal, A. Foehr, and C. Daraio. Reprogrammable phononic metasurfaces. *Advanced Materials*, 29(39):1700628, 2017.
- [23] F. Casadei, T. Delpero, A. Bergamini, P. Ermanni, and M. Ruzzene. Piezoelectric resonator arrays for tunable acoustic waveguides and metamaterials. *Journal of Applied Physics*, 112(6):064902, 2012.
- [24] D. Cardella, P. Celli, and S. Gonella. Manipulating waves by distilling frequencies: a tunable shunt-enabled rainbow trap. *Smart Materials and Structures*, 25(8):085017, 2016.
- [25] Y.Y. Chen, X.P. Li, H. Nassar, G.K. Hu, and G.L. Huang. A programmable metasurface for real time control of broadband elastic rays. *Smart Materials and Structures*, 27(11):115011, 2018.
- [26] F. Allein, V. Tournat, V.E. Gusev, and G. Theocharis. Tunable magneto-granular phononic crystals. *Applied Physics Letters*, 108(16):161903, 2016.
- [27] M. Lapine, I. V. Shadrivov, D. A. Powell, and Y. S. Kivshar. Magnetoelastic metamaterials. *Nature Mater.*, 11:30 – 33, 2012.
- [28] O.R. Bilal, A. Foehr, and C. Daraio. Bistable metamaterial for switching and cascading elastic vibrations. *Proceedings of the National Academy of Sciences of the United States of America*, 114(18):4603–4606, 2017.
- [29] R.K. Pal and P.H. Geubelle. Wave tailoring by precompression in confined granular systems. *Physical Review E*, 90:042204, Oct 2014.

- [30] J. Jang, C.Y. Koh, K. Bertoldi, M.C. Boyce, and E.L. Thomas. Combining pattern instability and shape-memory hysteresis for phononic switching. *Nano Letters*, 9(5):2113–2119, 2009. PMID: 19391612.
- [31] S. Rudykh and M.C. Boyce. Transforming wave propagation in layered media via instability-induced interfacial wrinkling. *Physical Review Letters*, 112:034301, Jan 2014.
- [32] P. Wang, F. Casadei, S. Shan, J. C. Weaver, and K. Bertoldi. Harnessing buckling to design tunable locally resonant acoustic metamaterials. *Physical Review Letters*, 113(1):014301, 2014.
- [33] J. Meaud and K.K. Che. Tuning elastic wave propagation in multistable architected materials. *International Journal of Solids and Structures*, 122-123:69 – 80, 2017.
- [34] Y. Bar-Sinai, G. Librandi, K. Bertoldi, and M. Moshe. Geometric charges and nonlinear elasticity of two-dimensional elastic metamaterials. *Proceedings of the National Academy of Sciences of the United States of America*, 2020.
- [35] E. Fermi, J. Pasta, and S. Ulam. *Studies of nonlinear problems*. Los Alamos Scientific Laboratory, Los Alamos, 1955.
- [36] Dr. D. J. Korteweg and Dr. G. de Vries. Xli. On the change of form of long waves advancing in a rectangular canal, and on a new type of long stationary waves. *The London, Edinburgh, and Dublin Philosophical Magazine and Journal of Science*, 39(240):422–443, 1895.
- [37] N. J. Zabusky and M. D. Kruskal. Interaction of "solitons" in a collisionless plasma and the recurrence of initial states. *Physical Review Letters*, 15:240–243, Aug 1965.
- [38] C. Daraio, V. F. Nesterenko, E. B. Herbold, and S. Jin. Strongly nonlinear waves in a chain of teflon beads. *Physical Review E*, 72:016603, Jul 2005.

- [39] C. Daraio, V.F. Nesterenko, E.B. Herbold, and S. Jin. Tunability of solitary wave properties in one-dimensional strongly nonlinear phononic crystals. *Physical Review E*, 73:026610, Feb 2006.
- [40] A. Spadoni and C. Daraio. Generation and control of sound bullets with a nonlinear acoustic lens. *Proceedings of the National Academy of Sciences of the United States of America*, 107(16):7230–7234, 2010.
- [41] C. Daraio, V. F. Nesterenko, E. B. Herbold, and S. Jin. Energy trapping and shock disintegration in a composite granular medium. *Physical Review Letters*, 96:058002, Feb 2006.
- [42] B. G. Chen, N. Upadhyaya, and V. Vitelli. Nonlinear conduction via solitons in a topological mechanical insulator. *Proceedings of the National Academy of Sciences of the United States of America*, 111(36):13004–13009, 2014.
- [43] B. Deng, L. Chen, D. Wei, V. Tournat, and K. Bertoldi. Pulse-driven robot: Motion via solitary waves. *Science Advances*, 6(18), 2020.
- [44] J.R. Raney, N. Nadkarni, C. Daraio, D.M. Kochmann, J.A. Lewis, and K. Bertoldi. Stable propagation of mechanical signals in soft media using stored elastic energy. *Proceedings of the National Academy of Sciences of the United States of America*, 113(35):9722–9727, 2016.
- [45] B. Deng, J. R. Raney, V. Tournat, and K. Bertoldi. Elastic vector solitons in soft architected materials. *Physical Review Letters*, 118:204102, May 2017.
- [46] R. Ziv and G. Shmuel. Oscillating vector solitary waves in soft laminates. *Journal of the Mechanics and Physics of Solids*, 143:104058, 2020.
- [47] A.J. Sievers and S. Takeno. Intrinsic localized modes in anharmonic crystals. *Physical Review Letters*, 61:970–973, Aug 1988.
- [48] G. Iooss and G. James. Localized waves in nonlinear oscillator chains. *Chaos: An Interdisciplinary Journal of Nonlinear Science*, 15(1):0151113, 2005.
- [49] D.K. Campbell, S. Flach, and Y.S. Kivshar. Localizing energy through nonlinearity and discreteness. *Physics Today*, 57(1):43–49, 2004.

- [50] S. Flach and A.V. Gorbach. Discrete breathers — advances in theory and applications. *Physics Reports*, 467(1):1 – 116, 2008.
- [51] N. Boechler, G. Theocharis, S. Job, P. G. Kevrekidis, Mason A. Porter, and C. Daraio. Discrete breathers in one-dimensional diatomic granular crystals. *Physical Review Letters*, 104:244302, Jun 2010.
- [52] M. A. Hasan, S. Cho, K. Remick, A.F. Vakakis, D.M. McFarland, and W.M. Kriven. Experimental study of nonlinear acoustic bands and propagating breathers in ordered granular media embedded in matrix. *Granular Matter*, 17:49–72, 2015.
- [53] M.F. Blackstock, D.T. Hamilton, et al. *Nonlinear Acoustics*. Academic Press, San Diego, CA, 1998.
- [54] A. H. Nayfeh and D. T. Mook. *Nonlinear Oscillations*. Wiley-VCH, New Wiley-VCH, New York, 1995.
- [55] V. A. Krasilnikov and L. K. Zarembo. Nonlinear interaction of elastic waves in solids. *IEEE Transactions on Ultrasonics*, 14(1):12–17, Jan 1967.
- [56] L. K. Zarembo and V. A. Krasilnikov. Nonlinear phenomena in the propagation of elastic waves in solids. *Physics-Uspokhi*, 13(6):778, 1971.
- [57] W.J.N. De Lima and M.F. Hamilton. Finite-amplitude waves in isotropic elastic plates. *Journal of Sound and Vibration*, 265(4):819–839, 2003.
- [58] M. Deng, P. Wang, and X. Lv. Experimental observation of cumulative second-harmonic generation of lamb-wave propagation in an elastic plate. *Journal of Physics D: Applied Physics*, 38(2):344, 2005.
- [59] C. Bermes, J.Y. Kim, J.M Qu, and L.J. Jacobs. Experimental characterization of material nonlinearity using lamb waves. *Applied Physics Letters*, 90(2):021901, 2007.
- [60] K. H. Matlack, J. Y. Kim, L. J. Jacobs, and J. Qu. Experimental characterization of efficient second harmonic generation of lamb wave modes in a nonlinear elastic isotropic plate. *Journal of Applied Physics*, 109(1):014905, 2011.

- [61] M.X. Deng and J.F. Pei. Assessment of accumulated fatigue damage in solid plates using nonlinear lamb wave approach. *Applied Physics Letters*, 90(12):121902, 2007.
- [62] B. Liang, X.S. Guo, J. Tu, D. Zhang, and J. C. Cheng. An acoustic rectifier. *Nature Materials*, 9:989, 2010.
- [63] Di Zhou, Jihong Ma, Kai Sun, Stefano Gonella, and Xiaoming Mao. Switchable phonon diodes using nonlinear topological maxwell lattices. *Physical Review B*, 101:104106, Mar 2020.
- [64] N. Boechler, G. Theocharis, and C. Daraio. Bifurcation-based acoustic switching and rectification. *Nature Materials*, 10(9):665 – 668, 2011.
- [65] V.J. Sánchez-Morcillo, I. Pérez-Arjona, V. Romero-García, V. Tournat, and V.E. Gusev. Second-harmonic generation for dispersive elastic waves in a discrete granular chain. *Physical Review E*, 88:043203, 2013.
- [66] A. Mehrem, N. Jiménez, L.J. Salmerón-Contreras, X. García-Andrés, L.M. García-Raffi, R. Picó, and V.J. Sánchez-Morcillo. Nonlinear dispersive waves in repulsive lattices. *Physical Review E*, 96:012208, Jul 2017.
- [67] V.V. Konotop. Second-harmonic generation in diatomic lattices. *Physical Review E*, 54:4266–4270, Oct 1996.
- [68] J. Cabaret, V. Tournat, and P. Béquin. Amplitude-dependent phononic processes in a diatomic granular chain in the weakly nonlinear regime. *Physical Review E*, 86:041305, 2012.
- [69] V. Tournat, V. E. Gusev, V. Yu Zaitsev, and B. Castagnede. Acoustic second-harmonic generation with shear to longitudinal mode conversion in granular media. *Europhys. Lett.*, 66(6):798, 2004.
- [70] S.P. Wallen and N. Boechler. Shear to longitudinal mode conversion via second harmonic generation in a two-dimensional microscale granular crystal. *Wave Motion*, 68:22–30, 2017.

- [71] R. Ganesh and S. Gonella. Nonlinear waves in lattice materials: Adaptively augmented directivity and functionality enhancement by modal mixing. *Journal of the Mechanics and Physics of Solids*, 99:272 – 288, 2017.
- [72] R. Ganesh and S. Gonella. Experimental evidence of directivity-enhancing mechanisms in nonlinear lattices. *Applied Physics Letters*, 110(8):084101, 2017.
- [73] Matthew D. Fronk and Michael J. Leamy. Internally resonant wave energy exchange in weakly nonlinear lattices and metamaterials. *Physical Review E*, 100:032213, Sep 2019.
- [74] V. Tournat, V. E. Gusev, and B. Castagnède. Self-demodulation of elastic waves in a one-dimensional granular chain. *Physical Review E*, 70:056603, Nov 2004.
- [75] Feng Li, Priscilla B. Silva, and Varvara G. Geers, Marc G. D. and Kouznetsova. Granular acoustic switches and logic elements. *Nature Communications*, 5:5311, 2014.
- [76] Valentina Zega, Priscilla B. Silva, and Varvara G. Geers, Marc G. D. and Kouznetsova. Experimental proof of emergent subharmonic attenuation zones in a nonlinear locally resonant metamaterial. *Scientific Reports*, 10:12041, 2020.
- [77] J. M. T. Thompson and H. B. Stewart. *Nonlinear Dynamics and Chaos*. John Wiley and Sons, LTD, 2002.
- [78] G. Chakraborty and A.K. Mallik. Dynamics of a weakly non-linear periodic chain. *International Journal of Non-Linear Mechanics*, 36(2):375–389, 2001.
- [79] R.K. Narisetti, M.J. Leamy, and M. Ruzzene. A perturbation approach for predicting wave propagation in one-dimensional nonlinear periodic structures. *Journal of Vibration and Acoustics*, 132(3):031001, 2010.
- [80] M.H. Holmes. *Introduction to perturbation methods*. Springer, second edition, 2012.
- [81] B.S. Lazarov and J.S. Jensen. Low-frequency band gaps in chains with attached non-linear oscillators. *International Journal of Non-Linear Mechanics*, 42(10):1186 – 1193, 2007.

- [82] R.K. Narisetti, M. Ruzzene, and M.J. Leamy. A perturbation approach for analyzing dispersion and group velocities in two-dimensional nonlinear periodic lattices. *Journal of Vibration and Acoustics*, 133(6):061020, 2011.
- [83] K. Manktelow, R.K. Narisetti, M.J. Leamy, and M. Ruzzene. Finite-element based perturbation analysis of wave propagation in nonlinear periodic structures. *Mechanical Systems and Signal Processing*, 39(1):32 – 46, 2013.
- [84] R.K. Pal, J. Vila, M. Leamy, and M. Ruzzene. Amplitude-dependent topological edge states in nonlinear phononic lattices. *Physical Review E*, 97:032209, Mar 2018.
- [85] M. Bukhari and O. Barry. Spectro-spatial analyses of a nonlinear metamaterial with multiple nonlinear local resonators. *Nonlinear Dynamics*, 99:1539 – 1560, 2020.
- [86] L. Bonanomi, G. Theocharis, and C. Daraio. Wave propagation in granular chains with local resonances. *Physical Review E*, 91:033208, Mar 2015.
- [87] X. Fang, J.H. Wen, B. Bonello, J.F. Yin, and D.L. Yu. Ultra-low and ultra-broad-band nonlinear acoustic metamaterials. *Nature Communications*, 8(1):1288, 2017.
- [88] X. Fang, J.H. Wen, D.L. Yu, G.L. Huang, and J.F. Yin. Wave propagation in a nonlinear acoustic metamaterial beam considering third harmonic generation. *New Journal of Physics*, 20(12):123028, 2018.
- [89] J. Bunyan, K.J. Moore, A. Mojahed, M.D. Fronk, M. Leamy, S. Tawfick, and A.F. Vakakis. Acoustic nonreciprocity in a lattice incorporating nonlinearity, asymmetry, and internal scale hierarchy: Experimental study. *Physical Review E*, 97:052211, May 2018.
- [90] M. Molerón, A. Leonard, and C. Daraio. Solitary waves in a chain of repelling magnets. *Journal of Applied Physics*, 115(18):184901, 2014.
- [91] N. Taberlet, J. Ferrand, and N. Plihon. Stability analysis of an array of magnets: When will it jump? *Physical Review Letters*, 120:264301, Jun 2018.

- [92] M. Molerón, C. Chong, A.J. Martínez, M.A Porter, P.G. Kevrekidis, and C. Daraio. Nonlinear excitations in magnetic lattices with long-range interactions. *New Journal of Physics*, 21(6):063032, jun 2019.
- [93] A. Askar and M.J. Lighthill. Dispersion relation and wave solution for anharmonic lattices and korteweg de vries continua. *Proc. R. Soc. London, Ser. A*, 334(1596):83–94, July 1973.
- [94] G.X. Huang, Z.P. Shi, and Z.X. Xu. Asymmetric intrinsic localized modes in a homogeneous lattice with cubic and quartic anharmonicity. *Physical Review B*, 47:14561–14564, Jun 1993.
- [95] G.X. Huang and B. Hu. Asymmetric gap soliton modes in diatomic lattices with cubic and quartic nonlinearity. *Physical Review B*, 57:5746–5757, Mar 1998.
- [96] S.P. Wallen, J. Lee, D. Mei, C. Chong, P. G. Kevrekidis, and N. Boechler. Discrete breathers in a mass-in-mass chain with hertzian local resonators. *Physical Review E*, 95:022904, Feb 2017.
- [97] B. Deng, P. Wang, Q. He, V. Tournat, and K. Bertoldi. Metamaterials with amplitude gaps for elastic solitons. *Nature Communications*, 9(1):3410, 2018.
- [98] B. Deng, V. Tournat, and K. Bertoldi. Effect of predeformation on the propagation of vector solitons in flexible mechanical metamaterials. *Physical Review E*, 98:053001, Nov 2018.
- [99] W. Jiao and S. Gonella. Mechanics of inter-modal tunneling in nonlinear waveguides. *Journal of the Mechanics and Physics of Solids*, 111:1–17, 2018.
- [100] W. Jiao and S. Gonella. Intermodal and subwavelength energy trapping in nonlinear metamaterial waveguides. *Physical Review Applied*, 10:024006, Aug 2018.
- [101] W. Jiao and S. Gonella. Dynamics of interacting particle systems: Modeling implications of the repulsive interactions and experiments on magnetic prototypes. *Physical Review B*, 102:054304, Aug 2020.
- [102] W. Jiao and S. Gonella. Doubly nonlinear waveguides with self-switching functionality selection capabilities. *Physical Review E*, 99:042206, Apr 2019.

- [103] S. Krenk. *Non-linear modeling and analysis of solids and structures*. Cambridge University Press, 2009.
- [104] R. Ganesh and S. Gonella. Invariants of nonlinearity in the phononic characteristics of granular chains. *Physical Review E*, 90(2):023205, 2014.
- [105] D. Griffiths. *Introduction to Electrodynamics*. Prentice Hall, Upper Saddle River, NJ, 3rd ed. edition, 2007.
- [106] W.C. Swope, H.C. Andersen, P.H. Berens, and K.R. Wilson. A computer simulation method for the calculation of equilibrium constants for the formation of physical clusters of molecules: Application to small water clusters. *The Journal of Chemical Physics*, 76(1):637–649, 1982.
- [107] M.H. Bae and J.H. Oh. Amplitude-induced bandgap: New type of bandgap for nonlinear elastic metamaterials. *Journal of the Mechanics and Physics of Solids*, 139:103930, 2020.
- [108] L. Meirovitch. *Fundamentals of vibrations*. Waveland Press, Long Grove, IL, 2010.
- [109] R. Ganesh and S. Gonella. Spectro-spatial wave features as detectors and classifiers of nonlinearity in periodic chains. *Wave Motion*, 50(4):821 – 835, 2013.

Appendix A

Derivation of the complete stiffness matrix

The complete stiffness matrix \mathbf{D} for the 2D magnetic resonator is derived as follows

$$\begin{aligned}
 \mathbf{D} &= - \nabla_{\mathbf{u}} \sum_{i=1}^3 \mathbf{F}_i \Big|_{\mathbf{u}=\mathbf{0}} = - \nabla_{\mathbf{u}} \sum_{i=1}^3 f(r_i) \mathbf{n}_i \Big|_{\mathbf{u}=\mathbf{0}} \\
 &= - \sum_{i=1}^3 [\mathbf{n}_i \otimes \nabla_{\mathbf{u}} f(r_i) + f(r_i) \nabla_{\mathbf{u}} \mathbf{n}_i]_{\mathbf{u}=\mathbf{0}} \\
 &= - \sum_{i=1}^3 [f'(r_i) \mathbf{n}_i \otimes \mathbf{n}_i]_{\mathbf{u}=\mathbf{0}} - \sum_{i=1}^3 f(r_i) \left[\frac{\mathbf{I}}{r_i} - \frac{(L_0 \mathbf{e}_i + \mathbf{u}) \otimes (L_0 \mathbf{e}_i + \mathbf{u})}{r_i^3} \right]_{\mathbf{u}=\mathbf{0}} \quad (\text{A.1}) \\
 &= - \sum_{i=1}^3 f'(L_0) \mathbf{e}_i \otimes \mathbf{e}_i - \sum_{i=1}^3 \frac{f(L_0)}{L_0} (\mathbf{I} - \mathbf{e}_i \otimes \mathbf{e}_i) \\
 &\equiv \mathbf{D}_0 + \mathbf{D}^*
 \end{aligned}$$

in which $\nabla_{\mathbf{u}} f(r_i)$ is derived as $\nabla_{\mathbf{u}} f(r_i) = f_r(r_i) \nabla_{\mathbf{u}} r_i = f'(r_i) \mathbf{n}_i$, $\nabla_{\mathbf{u}} \mathbf{n}_i = \begin{bmatrix} \partial n_i^x / \partial u & \partial n_i^x / \partial v \\ \partial n_i^y / \partial u & \partial n_i^y / \partial v \end{bmatrix}$, and \mathbf{I} is the identity matrix.

The components of $\nabla_{\mathbf{u}}\mathbf{n}_i$ are derived as

$$\begin{aligned}
\partial n_i^x / \partial u &= \partial \left(\frac{L_0 e_i^x + u}{r_i} \right) / \partial u = \frac{1}{r_i} - \frac{(L_0 e_i^x + u)^2}{r_i^3} \\
\partial n_i^x / \partial v &= \partial \left(\frac{L_0 e_i^x + u}{r_i} \right) / \partial v = - \frac{(L_0 e_i^x + u)(L_0 e_i^y + v)}{r_i^3} \\
\partial n_i^y / \partial u &= \partial \left(\frac{L_0 e_i^y + v}{r_i} \right) / \partial u = - \frac{(L_0 e_i^y + v)(L_0 e_i^x + u)}{r_i^3} \\
\partial n_i^y / \partial v &= \partial \left(\frac{L_0 e_i^y + v}{r_i} \right) / \partial v = \frac{1}{r_i} - \frac{(L_0 e_i^y + v)^2}{r_i^3}
\end{aligned} \tag{A.2}$$

The above equations can be written in a compact form using tensor notation as $\nabla_{\mathbf{u}}\mathbf{n}_i = \frac{\mathbf{I}}{r_i} - \frac{(L_0 \mathbf{e}_i + \mathbf{u}) \otimes (L_0 \mathbf{e}_i + \mathbf{u})}{r_i^3}$, which is adopted in Eq. A.1.

Appendix B

Preliminary stability analysis of the magnetic particle oscillator

In the analysis of the magnetic particle oscillator, we mentioned that instabilities may occur for certain configurations. For instance, in the case of $\theta = \pi/2$, the system approaches a 1D configuration, and we will show that its dynamical behavior becomes unstable in the horizontal direction. For the same parameters ($M = 1, L_0 = 1, \gamma = 10^4$), the complete stiffness matrix \mathbf{D} is calculated as

$$\begin{aligned}\mathbf{D} &= \mathbf{D}_0 + \mathbf{D}^* \\ &= \begin{bmatrix} 0 & 0 \\ 0 & 120000 \end{bmatrix} + \begin{bmatrix} -30000 & 0 \\ 0 & 0 \end{bmatrix} \\ &= \begin{bmatrix} -30000 & 0 \\ 0 & 120000 \end{bmatrix}\end{aligned}\tag{B.1}$$

where we notice that the first diagonal component is negative. From basic structural dynamics, a negative stiffness component is often related to dynamical instabilities. In this case, instabilities occur when the resonator is perturbed in the horizontal direction, which is due to the fact that there is no horizontal resistance provided in the system. To prevent the occurrence of instabilities in this configuration, the horizontal motion of the resonator is constrained in the simulation.

Appendix C

Experimental characterization of the force-displacement relation between two repulsive magnets

To provide reliable parameters for the analytical model, we conduct a static test on two magnets. The experimental setup is shown in Fig. C.1 (a). The two magnets are mounted on appropriately machined holder such that their sides can progressively moved against each other. A micrometer is used to control by small amounts the distance between the two magnets, and a highly sensitive load cell (shown in Fig. C.1 (b)) is attached to the top magnet grip to measure the repulsive force. The measured force values are plotted as circles in Fig. C.2, and fitted by an inverse power law $f(r) = br^{-a}$ using “lsqcurvefit” in Matlab (based on the method of nonlinear least squares), which yields $a = 4.5824$ and $b = 1.6209 \times 10^{-10}$.

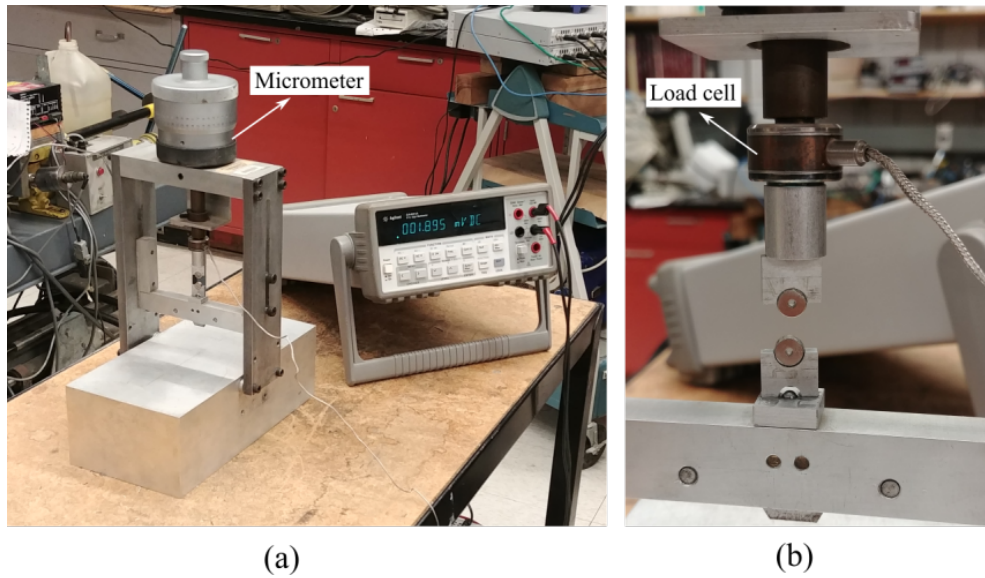


Figure C.1: Experimental characterization of the repulsive force between magnets. (a) Testing apparatus. (b) Detail of the magnets position.

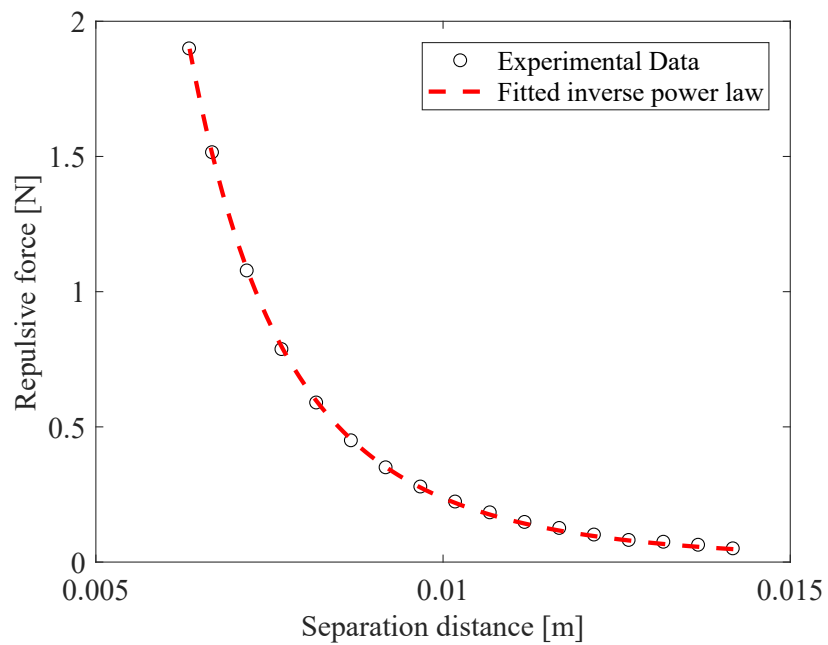


Figure C.2: Experimental data and fitted force-displacement curve for two magnets with repulsive interaction.

Appendix D

Derivation of the non-zero forcing term f_u^2 at $O(\epsilon_2)$

The complete expression for the non-zero forcing term f_u^2 at $O(\epsilon_2)$, due to the quadratic nonlinearity embedded in the spring-mass chain, is

$$\begin{aligned}
f_u^2 &= -K_3 \left[\left(u_n^0 - u_{n-1}^0 \right)^2 - \left(u_{n+1}^0 - u_n^0 \right)^2 \right] \\
&= -K_3 \left[A_0^2 \phi_u^2 \left(1 - e^{-i\tilde{\xi}} \right)^2 e^{2i\tilde{\theta}_n} + c.c. + \underline{2A_0^2 |\phi_u|^2 \left(1 - e^{-i\tilde{\xi}} \right) \left(1 - e^{i\tilde{\xi}} \right)} \right] \\
&+ K_3 \left[A_0^2 \phi_u \left(e^{i\tilde{\xi}} - 1 \right)^2 e^{2i\tilde{\theta}_n} + c.c. + \underline{2A_0^2 |\phi_u|^2 \left(e^{-i\tilde{\xi}} - 1 \right) \left(e^{i\tilde{\xi}} - 1 \right)} \right] \quad (D.1) \\
&= -K_3 A_0^2 \phi_u^2 \left[\left(1 - e^{-i\tilde{\xi}} \right)^2 - \left(e^{i\tilde{\xi}} - 1 \right)^2 \right] e^{2i\tilde{\theta}_n} + c.c. \\
&= -8i K_3 A_0^2 \phi_u^2 \sin \tilde{\xi} \sin^2 \frac{\tilde{\xi}}{2} e^{2i\tilde{\theta}_n} + c.c.
\end{aligned}$$